Development of Apertureless Microscopy and Force Microscopy of GaN and CeO_2

Thesis by

Paul M. Bridger

In Partial Fulfillment of the Requirements

for the Degree of

Doctor of Philosophy

California Institute of Technology

Pasadena, California

1999

(Submitted May 11, 1999)

To my family

List of Publications and Presentations

Work related to this thesis has been or will be presented in the following:

Nanoscale optical imaging of chromosomes with apertureless microscopy P. M. Bridger and T. C. McGill. To appear in Scanning.

Observation of nanometer scale optical property discrimination using a near-field scanning apertureless microscope P. M. Bridger and T. C. McGill. Presented at Scanning 99. To appear in Optics Letters.

Modification of induced surface charges in GaN by light and strain as observed by electric force microscopy P.M. Bridger, Z.Z. Bandic, E.C. Piquette, and T.C. McGill. Presented at PCSI '99 and to appear in J. Vac. Sci. Tech.

Measurement of induced surface charge, contact potentials and surface states in GaN by electric force microscopy P.M. Bridger, Z.Z. Bandic, E.C. Piquette, and T.C. McGill. Presented at Scanning 99 and To be published Appl. Phys. Lett.

Correlation between the surface defect distribution and minority carrier transport properties in GaN, P.M. Bridger, Z.Z. Bandic, E.C. Piquette, and T.C. McGill, Appl. Phys. Lett. 73 (23) 3438 (1998).

Resolution and Optical Contrast in Scanning Interferometric Apertureless Microscopy, P. M. Bridger, C. J. Hill, T. C. McGill. Presented at Materials Research Society meeting, San Francisco, April, 1998.

Nanoscale Chacterization of Linear Dislocations and Surface Defects in GaN, P.M. Bridger, Z.Z. Bandic, E.C. Piquette, and T.C. McGill, presented at Materials Research Society meeting, San Francisco, April, 1998.

Optical Sensitivity of Indium-Tin Oxide Tunnel Switch Diodes. Presented at the American Physical Society meeting, Los Angeles, March, 1998. Submitted to IEEE Trans. on Elec. Devices.

Minority carrier diffusion length and lifetime in GaN, Z. Z. Bandic, P. M. Bridger, E. C. Piquette, and T. C. McGill, Appl. Phys. Lett. 72 (24) 3166 (1998).

Electron diffusion length and lifetime in p-type GaN, Z. Z. Bandic, P. M. Bridger, E. C. Piquette, and T. C. McGill. Appl. Phys. Lett. 73 (22) 3276 (1998).

Design of GaN/AlGaN high power devices, invited talk, by Z.Z. Bandic, E.C. Piquette, P.M. Bridger, and T.C. McGill, Electrochemical Society meeting in Boston, Nov. 1-6, 1998; Electrochemical Society Proceedings **98** 39 (1998).

The Values of Minority Carrier Lifetime and their Implications for Bipolar Devices, invited talk, Z. Z. Bandic, E. C. Piquette, P. M. Bridger, and T. C. McGill, Workshop on wide bandgap bipolar devices, January 1999.

Nitride based high power devices: design and fabrication issues, invited paper, by Z.Z. Bandic, E.C. Piquette, P.M. Bridger, R.A. Beach, and T.C. McGill, Solid State Electron. 42, 2289 (1998).

Design and Fabrication of Nitride Based High Power Devices, Z. Z. Bandic, E. C. Piquette, P. M. Bridger, T. F. Kuech, and T. C. McGill, Mat. Res. Soc. Symp. Proc. 483, 399 (1998).

Nitride Based High Power Devices: Transport Properties, Linear Defects and Goals, Z. Z. Bandic, P. M. Bridger, E. C. Piquette, T. F. Kuech, and T. C. McGill, Mat. Res. Soc. Symp. Proc. 512, 27 (1998).

High Voltage (450 V) GaN Schottky Rectifiers, Z. Z. Bandic, P. M. Bridger, T. C. McGill, R. P. Vaudo, V. M. Phanse, and J. M. Redwing, Appl. Phys. Lett. **74**, 1266 (1999).

Growth of III-Nitrides by RF-Assisted Molecular Beam Epitaxy, E. C. Piquette, P. M. Bridger, Z. Z. Bandic, and T. C. McGill, Mat. Res. Soc. Symp. Proc. 512, 387 (1998).

Morphology and Polarity of MBE Grown GaN on Sapphire (0001), E. C. Piquette, P. M. Bridger, R. A. Beach, Z. Z. Bandic, and T. C. McGill, presented at NA-MBE 17, Penn State, Oct. 1998, to be published in J. Vac. Sci. Technol. B.

Morphology and Polarity of MBE Grown GaN on Sapphire (0001) , E. C. Piquette, P. M. Bridger, R. A. Beach, Z. Z. Bandic, and T. C. McGill, submitted to MRS Fall 1998 Boston.

Proximity Lithography Device. Patent Pending under U.S. Provisional Patent Application 60/039,361 March, 1997.

Acknowledgements

First and foremost I would like to thank my advisor, Dr. Tom McGill who provided the intellectual freedom to pursue a new research direction and the resources to make it happen. Tom has put together a superb lab and a great group which exceeded all my expectations for Caltech.

Tom's group is certainly unique and I have not met a more talented group of students. Alicia Alonzo, Zvonimir Bandić, Matt Barton, Bob Beach, Xavier Cartoixa, Xiao-Chang Cheng, Cory Hill, Joel Jones, Eric Piquette, and Robert Strittmatter have all been a pleasure to work with. In particular I'd like to give a second helping of praise to the fellow students I've worked with throughout graduate school. Cory and I spent many hours together working on the apertureless microscope and many nights reworking our computer system. I wish we had more time for climbing and picking stocks. Joel is one totally committed dude whose research was too sexy for APL despite the pressures of press releases. Eric's critiques kept me honest. My collaboration with Zvonimir inspired a large portion of this thesis. He is one of the smartest people I've ever met and great friend.

A huge thank you goes to Gerry Picus for his patience while proofreading my papers and thesis. I am grateful for his persistence in forcing me to clarify my sometimes vague ideas.

Thanks to Per-Olov Pettersson and Erik Daniel who overlapped with me as senior graduate students and showed me the ropes.

Ogden Marsh, Ed Yu, Darryl Smith, Dave Ting, Yoshi Hagiwara, and Amikam Zur have all contributed with their wealth of experience and insight.

Tim Harris, Gloria Pendlay, and Marcia Hudson have all held the group together in its day to day operation. I am grateful to all of them for cutting the red tape for me.

Outside the group I'd like to acknowledge Kerry Vahala, Roberto Paiella, and

Guido Hunziker with whom I've shared many lunchtime discussions. I'd like to give special thanks to Guido Hunziker for our many adventures together.

Luke Ghislain of Digital Instruments has been a valuable source of information and discussion throughout my graduate career. His input helped tremendously when I was getting started with the apertureless microscope project.

Finally I'd like to thank my wife, Anna, for putting up with my long hours while finishing my degree.

Abstract

This thesis concentrates on the development of both novel scanning probes as well as novel applications of existing ones in three major areas. The first area is our development of apertureless microscopy and progress toward our goal of 1nm optical imaging and spectroscopy. Fundamental experiments and simulations of the apertureless imaging mechanism were conducted using nanosphere size standards. Fifteen nanometer resolution as well as optical property discrimination was demonstrated. The apertureless microscope was then used to investigate the near field optical structure of chromosomes and anti-reflective polymer thin films. The second area is the investigation of the electronic properties of the wide bandgap semiconductor GaN by atomic force microscopy. Defects in GaN were correlated to diffusion lengths as measured by electron beam induced current. Electric force microscopy (EFM), a varient of atomic force microscopy, was subsequently used to investigate sub 1μm electric field gradient and surface potential variation associated with these defects. A novel application of EFM to measure the surface state density was also demonstrated. The third area is another novel application of EFM for localized charge storage in double barrier CeO2/Si/Ce02/Si structures which may have relevance for data storage and charge directed lithography.

Contents

List of Figures

List of Tables

Chapter 1 Introduction

1.1 Thesis overview

This thesis concentrates on the development of both novel scanning probes as well as novel applications of existing ones in three major areas. The first area is our development of apertureless microscopy and progress toward our goal of 1nm optical imaging and spectroscopy. Fundamental experiments and simulations of the apertureless imaging mechanism were conducted using nanosphere size standards. Fifteen nanometer resolution as well as optical property discrimination was demonstrated. The apertureless microscope was then used to investigate the near field optical structure of chromosomes and anti-reflective polymer thin films. The second area is the investigation of the electronic properties of the wide bandgap semiconductor GaN by atomic force microscopy. Defects in GaN were correlated to diffusion lengths as measured by electron beam induced current. Electric force microscopy (EFM), a varient of atomic force microscopy, was subsequently used to investigate sub 1μm electric field gradient and surface potential variation associated with these defects. A novel application of EFM to measure the surface state density was also demonstrated. The third area is another novel application of EFM for localized charge storage in double barrier CeO2/Si/Ce02/Si structures which may have relevance for data storage and charge directed lithography.

1.2 Motivation

Apertureless Microscopy

Microscopy has always been at the forefront of scientific investigation since many basic physical phenomena lie beyond human sensory perception. To perceive length scales

smaller than a fraction of a millimeter, a "microscope" of some description is needed. Therefore, It is hard to underestimate the scientific impact of the development of new microscopes and techniques.

Optical microscopes are of particular interest since spectroscopy can give non-invasive chemical information. Other forms of microscopy such as scanning electron microscopy, scanning tunneling microscopy, or atomic force microscopy either cannot distinguish chemical information or impose severe restrictions on the sample properties. Yet, conventional optics suffers from the wave nature of light where the diffraction limit sets a limit to the size of objects that can be differentiated. Interestingly enough, diffraction limited microscopes appeared around the 1850's. It was not until over 100 years later in 1986 that the first sub-diffraction limit images were obtained using tapered fiber probes [1]. Today, in 1999, tapered probes have reached practical detection and fabrication limits at around 50 nm resolution. The apertureless microscope [2] may be one solution to extend optical resolution to 1 nm, or even smaller. Such resolutions would provide a huge number of applications such as determining the internal structure of chromosomes, single protein molecules, and DNA which would have significant technological and scientific impact.

It is the purpose of the first part of this thesis to examine two important questions about the apertureless microscope.

1 Does it give sub-wavelength resolution?

2 What is the ultimate limit of the resolution?

Force Microscopy

Besides optical microscopy, there are a range of other techniques that are based on the success of the atomic force microscope. Their principle of operation is typically to shrink a detector so that the measurement of interest is confined to the detector dimension. In this way, spatially localized measurements can be made to examine the micro-structure that is averaged in a bulk measurement.

The second part of this thesis deals primarily with the nanostructure of the wide

bandgap semiconductor GaN and how it influences the bulk material properties [3, 4]. Nitride based devices have been of great interest in the last few years, notably due to their success in optoelectronics, where lasers and light emitting diodes have been demonstrated and successfully commercialized. Applications of nitrides are also expected in high power and high temperature electronics, as well as solar blind ultraviolet detectors. In our lab, interest in the nitrides was motivated by high power rectification and switching because the nitrides can stand off the high fields required for high voltage applications [5].

In addition to localized measurements, scanning probe techniques can also be used for modifying the structures they measure [6, 7]. Today, as the dimensions shrink in electronics and data storage, alternatives are being sought to replace current technology making scanning probes an attractive alternative. Probe techniques have even been driven to the point of thermomechanical (scratching with a hot tip) writing in polymers with AFM tips. The third and final topic describes controlled charge storage in double barrier CeO2/Si/Ce02/Si structures with spatial dimensions comparable to state of the art magnetic bit sizes.

Nanometer scale charge storage in cerium oxide may also have implications for silicon electronics for biosensors. We have also been researching ways of producing nanostructures in silicon. Presently, silicon has limited applicability for nanostructures because of the lack of a crystalline wide bandgap companion for the production of heterojunctions. My colleagues in our lab have recently shown that the Si/CeO2/Si couple could be the basis for a fully functional heterostructure technology [8]. These technologies include various quantum devices such as resonant tunneling devices, tunnel switched diodes, standard MOSFET's as well as three-dimensional electronics. Long lived charged islands could be functionalized with polar molecules as part of the fabrication of biosensors or biochips on silicon electronics since this technique would allow us to precisely attach molecules directly on fully functional transistors.

1.3 Summary of Results

1.3.1 Apertureless Microscopy

Over the course of this work, we have developed a very versatile instrument that can be configured for both phase and intensity imaging modes. Due to the controversy surrounding apertureless microscopy [9], we have also conducted experiments to explore the fundamental limits of the resolution and performance of this technique. At present, the instrument has an optical resolution approaching 15 nm and can distinguish objects of different indices of refraction.

Since the mechanism of converting evanescent fields into propagating ones was not understood for the apertureless microscope, we have also simulated the near-field perturbation mechanism. Simulations of simple situations show that a dipole coupling model agrees with many of the experimental observations.

1.3.2 Minority Carrier Diffusion Lengths

Using atomic force microscopy and electron beam induced current, we have studied linear dislocations and surface defects in p and n-type GaN grown by chemical vapor deposition(MOCVD), hydride vapor phase epitaxy (HVPE) and molecular beam epitaxy (MBE). The surface pits due to threading dislocations were found not to be distributed randomly but on the boundaries of growth columns. These dislocations are thought to be electrically active since the average distance between them (average column size) is comparable to minority carrier diffusion lengths as measured by electron beam induced current experiments. Diffusion lengths found for holes and electrons are on the order of $L_p = 0.28\mu$m and $L_e = 0.16\mu$m which corresponded to the sizes of regions free from surface dislocations in both cases.

This work not only represented some of the first measurements of minority carrier diffusion lengths, but it also indicated that they are affected by material quality.

1.3.3 Electric Force Microscopy

We have initiated several novel applications of electric force microscopy in two areas. We have studied molecular beam epitaxy grown GaN films to detect sub 1 micron regions of charge density variations associated with GaN extended defects. The large piezoelectric coefficients of GaN together with strain introduced by crystalline imperfections produce variations in piezoelectrically induced electric fields around these defects. The consequent spatial rearrangement of charges can be detected by electrostatic force microscopy and was found to be on the order of the characteristic Debye length for GaN at our dopant concentration.

The electric force microscope signal was also found to be a linear function of the contact potential between the metal coating on the tip and GaN. Electrostatic analysis of the data allowed us to measure both the surface state density and energy.

Finally, an electric force microscope was used to induce and image localized dots of charge in a double barrier CeO_2/Si/CeO_2/Si(111) structure. By applying large charging voltages and reducing the tip to sample separation to 3-5 nm, dots 20-50 nm in radius of both positive and negative charge have been written. These charge dots are shown to be stable over periods of time greater than a day, with a very slow spreading and decrease in total stored charge. It is shown that the dots may be rewritten and replaced by charge of the opposite sign by application of the opposite charging voltage.

1.4 Chapter Outline

The thesis is divided into two parts. Part I deals with near-field apertureless microscopy. Part II deals with semiconductor applications of force microscopy.

In Part I, Chapter 2 outlines the current techniques and issues related to near-field. Chapter 3 describes simulations of a dipole coupling model. Chapter 4 presents apertureless experiments on simple situations to support the calculations in Chapter 3 as well as real world applications.

In Part II, Chapter 6 presents the results of experiments correlating the defect distribution in GaN to electron beam induced current measurements of minority carrier diffusion lengths. Chapter 7 presents the results of electric force microscopy experiments to study piezoelectric effects in GaN. Chapter 8 describes localized, controlled charge storage in the CeO_2/Si system.

Bibliography

[1] E. Betzig, M. Isaacson, and A. Lewis, *Appl. Phys. Lett.* **51**, 2088 (1987).

[2] F. Zenhausern, M. P. O'Boyle, and H. K. Wickramasinghe, *Appl. Phys. Lett.* **65**, 1623 (1994).

[3] P.M.Bridger, Z.Z. Bandić, E.C. Piquette, and T.C. McGill, Appl. Phys. Lett., **73**, 3438 (1998).

[4] Z. Z. Bandić, P. M. Bridger, E. C. Piquette, and T. C. McGill *Appl. Phys. Lett.* **72**, 3166 (1998).

[5] Z.Z. Bandić, E. C. Piquette, P. M. Bridger, R. A. Beach, T. F. Kuech, and T. C. McGill. Solid State Electronics **42**, 2289 (1998).

[6] J. E. Stern, B. D. Terris, H. J. Mamin, and D. Rugar, Appl. Phys. Lett. **53**, 2717 (1988).

[7] D. Schaadt, E. Yu, S. Sankar, A. Berkowitz, Appl. Phys. Lett. **74**, 472 (1999).

[8] J. Jones, E. Croke, C. Garland, O. Marsh, T. McGill, J. Vac. Sci. Technol. B **16**, 2686 (1998).

[9] B. Hecht, H. Bielefeldt, Y. Inouye, L. Novotny, and D. W. Pohl, *J. Appl. Phys.* **81**, 2492 (1997).

Part I

Near-Field Scanning Apertureless Microscopy

Chapter 2 Near Field Optics

2.1 Overview of Near-field Optics

2.1.1 Historical Perspective

The implementation of E. A. Synge's idea of a near-field optical microscope [1] took almost 60 years until the demonstration of the fiber NSOM in 1986 [2]. As illustrated in the following passage from his paper of 1928, he not only the realized that near-field optics should be possible, but his ideas for its implementation are essentially unchanged. Conceptually, it contains the basis for the majority of near-field instruments thus far and a motivation that remains contemporary into the next century.

> It is generally accepted as an axiom of microscopy that the only way to extend resolving-power lies in the employment of light of smaller wave-lengths. Practical difficulties, however, rapidly accumulate as light of increasingly small wave-length is brought into service, and probably little hope is entertained of arriving at a resolution much beyond 0.1μ, with, perhaps 0.05μ as an extreme limit.
>
> Yet a method offers itself which lies a little outside the beaten track of microscopic work and raises various technical problems of a new kind, but which makes the attainment of resolution of 0.01μ and even beyond, dependent upon technical accomplishment which does not seem inpracticable at present. The idea of the method is exceedingly simple, and it has been suggested to me by a distinguished physicist that it would be of advantage to give it publicity, even though I was unable to develop it in more than an abstract way.

> We shall suppose, also, that a minute aperture, whose diameter is approximately 10^{-6} cm, has been constructed in an opaque plate or film and that this is illuminated intensely from below, and is placed immediately beneath the exposed side of the biological section, so that the distance of the minute hole from the section is a fraction of 10^{-6} cm. The light from the hole after passing through the section is focussed through a microscope upon a photo-electric cell, whose current measures light transmitted.
>
> The final limitations of the method seem, indeed, to depend solely upon the limitations to the opacity of the films for light of various wavelengths. For a film having the opacity of silver with respect to ordinary light, the practicable limit of resolution would seem to be about 0.005μ or 0.004μ.
>
> Since this degree of resolution should bring all living organisms within our scope an attempt to overcome the technical difficulties would seem to be justified.
>
> - *E. A. Synge, 1928.*

The idea of a limiting aperture still remains the standard way to implement near-field optical studies. However, one of the major disadvantages of small apertures is that they have very high losses which results in intrinsically weak signals. Around 1994 a new idea replacing the lossy aperture with a small "scattering" element appeared and initiated a new class of near-field optical instruments termed "apertureless" microscopes [3]. The potential for this technique is twofold. First, small scattering elements can be made **very** small since, unlike apertures, they are not skin depth limited. Second, the problem of detection becomes one of detecting a small perturbation which lends itself to sensitive techniques such as interferometry.

The following sections review some of the current techniques that are used to achieve sub-wavelength resolution using the optical near-field. This will set the background for the scanning apertureless microscope and review the major considerations for instrument design and performance.

Apertureless microscopy remains controversial and it is the point of a large fraction of this thesis to shed some light on the physics and applications of the technique.

Radiating and Non-radiating Fields

The first step to the understanding of near-field imaging is a formal theorem due to E. Wolf and M. Nieto-Vesperinas [4]. In particular, they show that when the scattering potential is continuous over the region occupied by the scattering object, the scattered field must always contain both homogeneous and evanescent waves. The second step is that the evanescent waves can be converted to detectable, propagating waves in the far field. The following techniques represent different embodiments of this conversion process.

2.2 Techniques

2.2.1 Near-field Scanning Optical Microscopy

Near-field scanning optical microscopy (NSOM) was concurrently developed by Denk and Pohl at IBM Zurich [5] and by Betzig and Lewis at Cornell around 1984. The first sub-wavelength images were collected by Betzig in 1986 [2, 6]. Its principle of operation is to use a tapered optical fiber to define a sub-wavelength aperture 50 - 100 nm in diameter. By bringing the aperture into the near-field of the sample, it can then be used to either illuminate or collect light. The distance to the sample is typically controlled by vibrating the fiber and using variations in the shear force when it is close to the sample. A schematic of the NSOM is shown in Figure 2.1. Many variants of the NSOM have been invented since the original instrument. They range from collecting the evanescent field from totally internally reflected light to bent fiber probes which are simultaneously used as atomic force microscope tips.

The major disadvantages of the NSOM are the difficulty in implementing the shear force distance regulation and the large losses in the tapered fiber which can no longer support propagating modes. Loss can be as high as a factor of 10^{-6} per pass through

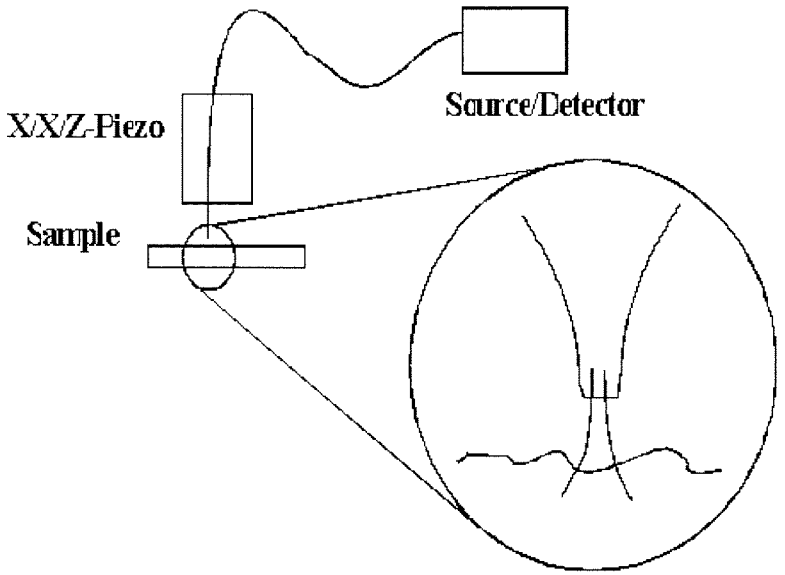

Figure 2.1: Schematic of the NSOM. In most cases, the NSOM is used in illumination mode where light from a laser propagates through the fiber to illuminate the sample in the near-field. High numerical aperture far-field optics then collect the resulting light.

the fiber which confines the NSOM to either illumination or collection. It is easy to see that experiments which use the fiber for both illumination and collection quickly become impractical after suffering losses of 10^{-12}.

2.2.2 Solid Immersion Lens

The solid immersion lens (SIL) technique was invented by Mansfield and Kino in 1990 [7] and improved by Ghislain and Ellings in 1998 [8, 9] for a scanning mode of operation. The principle behind the SIL is essentially the same as the conventional method of immersing the objective lens of a microscope in oil to increase the resolution. In a high index material the wavelength, and hence the resolution, is reduced by a factor of $1/n$. Instead of oil, this microscope uses a high index solid which is brought within the near-field distance ($< \lambda$) from the sample. Since the index of refraction of solids for visible light can be as high as 2.5, a resolution of around 100 nm can be obtained by using blue light.

In the first SIL microscope, the entire field of view needed to be in contact with the

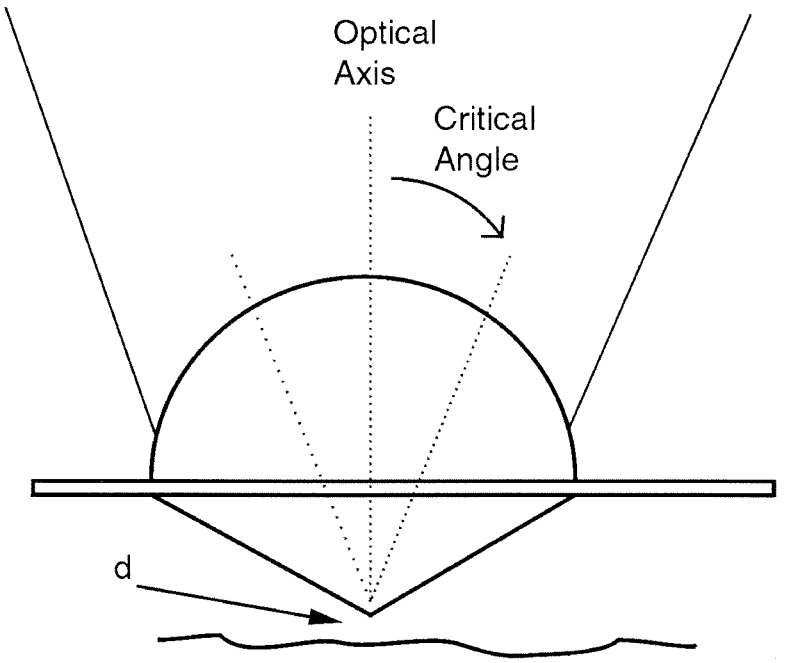

Figure 2.2: Schematic of the SIL. Light from a conventional microscope objective is focussed into the SIL to a diffraction limited spot at the apex of the lens. Consequently the diffraction limit is set by the index of the lens material. The SIL is then brought a distance, d, from the sample and scanned to build up an image. Since d is in the near-field, the diffraction limited spot is largely unaffected by the change in index which allows an improved resolution.

sample. As a result, maintaining the near-field distance condition over a large area was a significant problem. The solution as shown in Figure 2.2 was to make the apex of the lens very small and scan it over the sample. The lens-sample distance could then be maintained by attaching the lens to a lever arm and monitoring its deflection as the lens approached the sample. Using this technique, Ghislain has demonstrated both imaging and lithography. The imaging resolution was 150 nm and the lithography resolution was 190 nm when operating with a lens material with an index of 2.2 at a wavelength of 442 nm. The major advantage of the SIL is that the optical throughput is very high so it can be used both for collection and for illumination. High throughput also allows much greater scan rates than a conventional fiber NSOM. The disadvantages include sample wear due to the sharp tip as well as the resolution being diffraction limited. High index materials do not exceed about $n = 2.5$ for visible light so material properties will set the ultimate limit for the resolution.

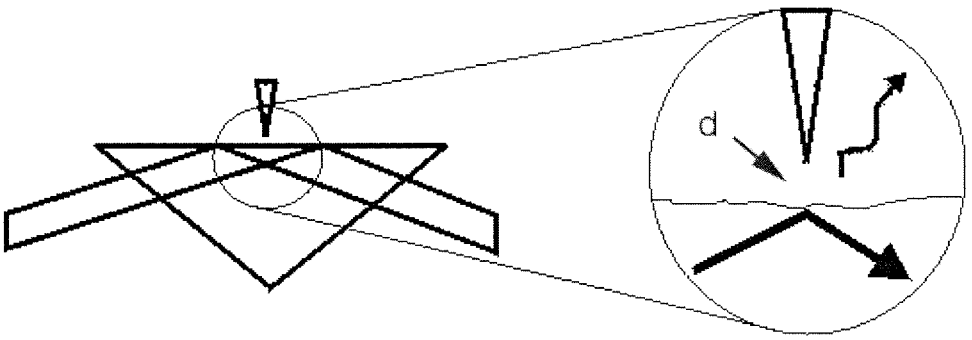

Figure 2.3: Schematic of the PSTM. Light is reflected from the surface of a prism at an angle greater than the critical angle. A sharp tip close to the surface then perturbs the evanescent fields to couple out a propagating wave. As the tip scans the sample, the light coupled out of the near field is then collected to form the image.

2.2.3 PSTM and others

The best known of some of the other techniques is the photon scanning tunneling microscope [10]. The principle behind photon scanning tunneling microscopy is to perturb the evanescent wave of totally internally reflected light. This is similar to frustrated total internal reflection microscopes. The difference between them is that instead of a large contact area between two prisms, the frustrating element is localized to the tip of a scanning probe microscope. A major disadvantage in the practical implementation of this class of near field microscopes is a large amount of stray light that is scattered from the surface of rough samples. For clarity, the PSTM technique is illustrated in Figure 2.3. There is an array of other techniques [11] that have been used for alternate near-field microscopes. Some of them are as follows. One possibility is very small integrated photodiodes at the tip of an AFM to "image" the near-field [12–14]. Another is to use surface enhancement effects of small silver particles to image single molecules [15]. A recent idea based on calculations of a field enhancement effect at a sharp metallic tip is to use the large field to enhance scattering [16, 17].

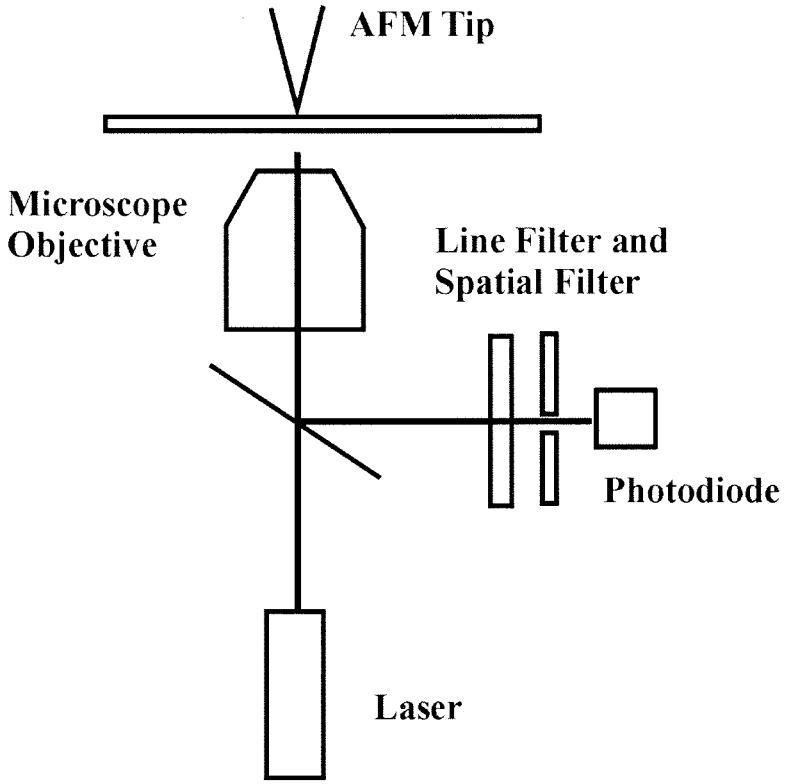

Figure 2.4: Schematic of the SAM. Laser light illuminates an AFM tip which is placed in the near field of a sample. The reflected light is subsequently modified by the tip and detected as the tip scans the sample. A laser line filter blocks light from the AFM laser and a spatial filter passes light from the tip while rejecting stray reflections

2.2.4 Scanning Apertureless Microscope

Scanning apertureless microscopy (SAM) is very similar to PSTM, and relies on the conversion of evanescent fields to propagating fields by scattering from a sharp tip very close to the sample. [18] The existence of such fields has been proved by Wolf as indicated in Section 2.1.1. The physics of the conversion process, however, remains a subject of research. The apertureless microscope operates by bringing a sharp tip within the near-field of a laser illuminated sample. The tip, by its presence, modifies the near-field distribution which in turn affects the illuminating light. Detecting the modified light as the tip is scanned across the sample forms the image. Figure 2.4 illustrates the apertureless technique. The major disadvantage of the apertureless microscope is that small perturbations on a large signal must be detected. Lock-in techniques and interferometric detection proposed by Wickramasinghe [3, 18–21]

make the task feasible but nevertheless problematic. The apertureless technique's attraction that overwhelms the detection problem is the resolution. Since the resolution should be limited to the size of the tip that modifies the near-field, it can, in principle, approach 1 nm or less. Tips are much easier to fabricate than apertures which gives a second advantage to the SAM. Not only can the tips be made very small, they are potentially very versatile since the tip properties can be modified by coating or attaching particles, molecules, etc.

2.3 Resolution

2.3.1 Diffraction Limited Resolution

Resolving power is the most important feature of any microscope system; unfortunately (and fortunately for some), it does not have an unambiguous definition. All of us are familiar with the standard definition of the Rayleigh limit for the optical resolution limit, so it is surprising how its principle is disregarded in scanning probe microscopy. The expression for the far field intensity distribution in the image plane for two uniform point sources is:

$$I(x,y) = \left[\frac{2J_1(Y_1)}{Y_1}\right]^2 + \left[\frac{2J_1(Y_2)}{Y_2}\right]^2 + 2\gamma_{12}\frac{2J_1(Y_1)}{Y_1}\frac{2J_1(Y_2)}{Y_2} \tag{2.1}$$

Where J_1 is the first order Bessel function and γ_{12} is the degree of coherence. $Y_{1,2} = \frac{2\pi}{\lambda}NA\sqrt{(x-x_{1,2})^2+(y-y_{1,2})^2}$ where NA is the numerical aperture of the lens, x and y refer to the position in the image plane and $x_{1,2}$, $y_{1,2}$ are the coordinates of the point sources 1 and 2.

This expression for the intensity distribution gives rise to the common two point resolution criteria, the spirit of which can be summarized by stating that *two luminous points on a dark background can be observed separately if their diffraction patterns are not too close to one another.* The differing degrees of "closeness" are:

The Rayleigh criterion for incoherent light: When the maximum of one Airy

pattern lies on the minimum of the other.

$$R = \frac{0.61\lambda}{NA} \tag{2.2}$$

The Sparrow criterion for both coherent and incoherent light: When the second derivative of the intensity is zero between the two Airy patterns.

$$R = \frac{0.47\lambda}{NA}, \text{ Incoherent Light} \tag{2.3}$$

$$R = \frac{0.73\lambda}{NA}, \text{ Coherent Light} \tag{2.4}$$

In keeping with the spirit of this definition, our resolution criterion will be a two point resolution where the scanning probe is said to have a resolution, R, when it can distinguish between adjacent objects both of size R. An illustration of this is the claim that AFM's have atomic resolution because one can observe the periodicity of the lattice yet cannot distinguish a substitutional defect as in Figure 2.5. Since the apertureless microscope should be able to attain resolutions on the order of the tip size (which can be atomic), future applications such as distinguishing protein structure or imaging nanometric optical properties will necessarily require performance defined by this type of resolution criterion.

2.3.2 Tip Limited Resolution

There are claims of near-field resolutions that are smaller than the probe size [22]. This makes little sense since it is the tip localization that provides the improved spatial accuracy in the first place. An analysis of the consequence of the probe size for the resolution is given in Reference [23] and is as follows. A probe of size "a" and response S is scanned at velocity v across an object of spatial frequency α represented

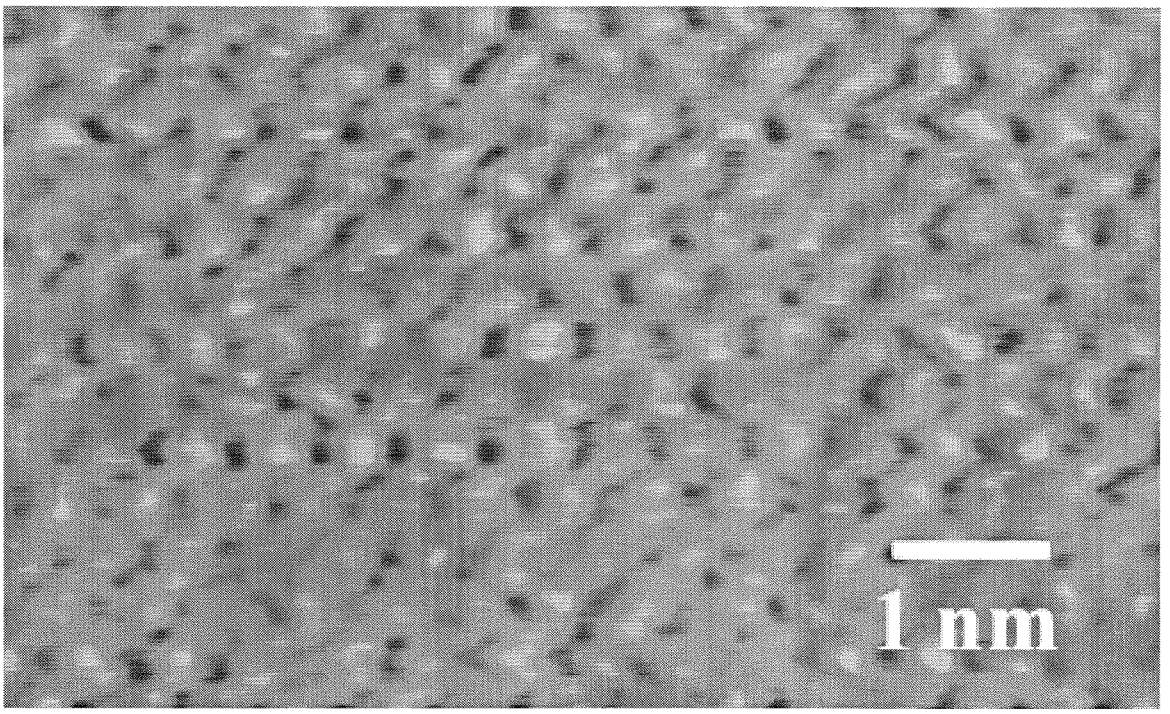

Figure 2.5: Contact AFM image of "atoms" of mica taken with our Multimode AFM and a Nanoscope IIIa controller.

by $f(x) = 1 + \cos(2\pi\alpha x)$. The detected signal is

$$g(t) = S\int_{-\infty}^{\infty} f(x)\text{rect}\left(\frac{x}{a}\right)dx \tag{2.5}$$

where

$$\text{rect}\left(\frac{x}{a}\right) = \begin{cases} 1 & , \ -a/2 \leq x \leq a/2 \\ 0 & , \ \text{otherwise} \end{cases} \tag{2.6}$$

Scanning over the sample converts spatial frequencies to the time domain by integrating out x in favor of t.

$$g(t) = S\int_{-\infty}^{\infty} [1 + \cos 2\pi(\alpha x + f_0 t)]\text{rect}\left(\frac{x}{a}\right)dx \tag{2.7}$$

$$g(t) = S\int_{-a/2}^{a/2} [1 + \text{Re } exp[2\pi(\alpha x + f_0 t)]]\,\text{rect}\left(\frac{x}{a}\right)dx \tag{2.8}$$

Now

$$g(t) = aS + aS\frac{\sin(\pi\alpha a)}{\pi\alpha a}cos(2\pi f_0 t) \tag{2.9}$$

Maximizing the second term gives $a = 1/2\alpha$ as the optimal probe size. Namely, the probe has to sample at twice the spatial frequency for a maximum signal.

2.4 Summary

Despite the wide variety of competing near-field optical techniques, it is the promise of resolution an order of magnitude better than any other method that convinced us to focus on apertureless microscopy. To reiterate Section 2.2.4 the resolution should be limited to the size of the tip, which can, in principle, approach 1 nm or less. In addition, the limits of apertureless microscopy are largely unexplored. Modified tips that would allow one to explore the physics of the imaging process by coating or attaching particles, molecules, etc, have not been pursued. Although Wickramasinghe has attempted resonant imaging, spectroscopy on the nanometer scale has not yet been attempted. The obvious applicability of apertureless microscopy for biological imaging has also been ignored.

The rest of Part I of this thesis will focus exclusively on apertureless microscopy, the physics of the imaging process, and its applications.

Bibliography

[1] E. H. Synge, Phil. Mag. **6** 356 (1928).

[2] E. Betzig, et al., Biophys. J., **49** 269 (1986).

[3] F. Zenhausern, M. P. O'Boyle, and H. K. Wickramasinghe, *Appl. Phys. Lett.* **65**, 1623 (1994).

[4] E. Wolf and M. Nieto-Vesperinas, J. Opt. Soc. Am. A **2** No. 6, 886 (1985).

[5] D. W. Pohl, W. Denk, and M. Lanz, *Appl. Phys. Rev. Lett.* **44**, 651 (1984).

[6] E. Betzig, M. Isaacson, and A. Lewis, *Appl. Phys. Lett.* **51**, 2088 (1987).

[7] S. M. Mansfield and G. S. Kino, *Appl. Phys. Lett.* **57**, 2615 (1990).

[8] L. P. Ghislain and V. B. Elings, *Appl. Phys. Lett.* **72**, 2279 (1998).

[9] L. P. Ghislain, V. B. Elings, K. B. Crozier, S. R. Manalis, S. C. Minne, K. Wilder, G. S. Kino, and C. F. Quate, *Appl. Phys. Lett.* **74** (1998).

[10] A. Ashino and M. Ohtsu, *Appl. Phys. Lett.* **72**, 1299 (1998).

[11] D. Courjon and C. Bainier, Rep. Prog. Phys. **57**, 989 (1994).

[12] K. Fukuzawa, Y. Tanaka, S. Akamine, H. Kuwano, and H. Yamada, *J. Appl. Phys.* **78**, 7376 (1995).

[13] S. Akamine, H. Kuwano, and H. Yamada, *Appl. Phys. Lett.* **68**, 579 (1996).

[14] R. C. Davis and C. C. Williams, *Appl. Phys. Lett.* **69**, 1179 (1996).

[15] S. Nie and S. R. Emory, *Science* **275** 1102 (1997).

[16] L. Novotny, E. Sanchez and X. S. Xie, *Ultramicroscopy*, 21 (1998).

[17] L. Novotny, R. X. Bian, and X. S. Xie, Phys. Rev. Lett. **79** 645 (1997).

[18] H. K. Wickramasinghe and C. C. Williams, Apertureless Near Field Optical Microscope, U.S. Patent 4,947,034 (April 28, 1989).

[19] F. Zenhausern, Y. Martin, and H. K. Wickramasinghe, *Science* **269**, 1083 (1995).

[20] Y. Martin, F. Zenhausern, and H. K. Wickramasinghe, *Appl. Phys. Lett.* **68**, 2475 (1996).

[21] Y. Martin, S. Rishton, and H. K. Wickramasinghe, *Appl. Phys. Lett.* **71**, 1 (1997).

[22] E. Betzig, P. L. Finn, and J. S. Weiner, *Appl. Phys. Lett.* **60**, 2484 (1992).

[23] M. A. Paesler and P. J. Moyer, *Near Field Optics: Theory Instrumentation and Applications* Wiley-Interscience (1996).

[24] C. Girard and A. Dereux, Rep. Prog. Phys. **59**, 657 (1996).

[25] K. Fukuzawa and Y. Tanaka, *Appl. Phys. Lett.* **71**, 169 (1997).

[26] J. Jersch and K. Dickmann, *Appl. Phys. Lett.* **68**, 868 (1996).

[27] G. Bryant, *Appl. Phys. Lett.* **72**, 768 (1998).

[28] R. Schad, S. M. Jordan, M. J. P. Stoelinga, M. W. J. Prins, R. H. M. Groenenveld, H. van Kempen, and H. W. van Kesteren, *Appl. Phys. Lett.* **73**, 2669 (1998).

[29] E. Mei and D. Higgins, *Appl. Phys. Lett.* **73**, 3515 (1998).

[30] C. E. Talley, M. A. Lee, and R. C. Dunn, *Appl. Phys. Lett.* **72**, 2954 (1998).

[31] R. Chang, W. Fann, and S. H. Lin, *Appl. Phys. Lett.* **69**, 2338 (1996).

[32] P. A. Crowell, D. K. Young, S. Keller, E. L. Hu, and D. D. Awschalom, *Appl. Phys. Lett.* **72**, 927 (1998).

Chapter 3 Simulations of Scanning Apertureless Microscopy

3.1 Motivation

Since the invention of near field scanning optical microscopy (NSOM), there have been many near field optical (NFO) techniques that attempt to measure optical properties of materials below the diffraction limit as described in the previous chapter [1]. Scanning apertureless microscopy (SAM) appears to be an attractive NFO technique since the theoretical optical resolution proposed by Wickramasinghe is on the order of 1 Å [2–4]. As a result, the SAM has generated significant interest because it could allow optical imaging approaching atomic resolution. Wickramasinghe's predictions, however, were based on the minimum detectable phase shift calculated from a coupled dipole model [4]. Without an adequate understanding of the near-field interaction mechanism, accurate predictions for the resolution cannot be made. Since the physical nature of the contrast mechanism for apertureless microscopy is not known or verified, this chapter presents simulations to support the coupled dipole model.

3.2 Simulations of the Coupled Dipole Model

Simulations of a simple model of tip-sample coupling display features that can account for experimental observations and clearly indicate that optical information is contained in scanning apertureless microscopy images. We have performed simulations using AFM data as a topographical template and incorporating a tip-sample dipole coupling model as the source of optical signal. These simulations show that features of the model, such as a dependence on both the polarization of the external laser source as well as the size and index of refraction of the tip and sample being

imaged. Experimental evidence supports many of the theoretical aspects found from the simulations. Much controversy exists as to whether or not one can separate information that is topographical in nature from that which is optical in any near-field imaging technique [6]. Hence, we have simulated a set of controlled experiments with the tip-sample dipole interaction model. This model is found to be rich in features which indicate that much of the information in the data is indeed optical in nature with little topographical crosstalk. The dipole interaction and all others, however, will always be an unavoidable combination of topography and optical properties since the two are intimately connected (Chapter 2, Section 2.1.1). The following simulations calculate the detected far-field intensity pattern based on near-field perturbations induced by the coupling of induced on the tip and the sample.

In our simulations we model the AFM tip as a radiating dipole, where the expression for the far-field intensity pattern produced by such a dipole is [7]

$$I_t = \frac{c\epsilon_0 k^4}{(4\pi\epsilon_0)^2 d^2}\langle|\vec{p}_t|^2\rangle \sin^2\phi \tag{3.1}$$

where I_t is the intensity, $\vec{p}_t$ is the induced dipole moment of the tip, d is the distance to the detector, k is the wave number of the radiation, c is the speed of light, ϵ_0 is the permitivity of free space, and ϕ is the angle between the vector from the tip to the detector and the dipole moment of the tip. The term in the above equation that contains optical information about the sample is $\vec{p}_t$, since the induced dipole moment of the tip is given by

$$\vec{p}_t = 4\pi\epsilon_0\alpha_t(\vec{E}_{laser} + \vec{E}_s) \tag{3.2}$$

where α_t is the polarizability of the tip. The total field incident on the tip is the sum of the laser field $\vec{E}_{laser}$ and the sample's field $\vec{E}_s$, therefore it is necessary to calculate the very near-field of the sample in order to determine the far-field radiation pattern produced by the tip. A schematic of the situation is shown in Figure 3.1.

For simplicity, we model the features being imaged as dielectric nanospheres with an induced dipole moment which, to first order, is $\vec{p}_s = 4\pi\epsilon_0\alpha_s\vec{E}_{laser}$, where all of the symbols are the same as before except that they refer to the sample instead of the

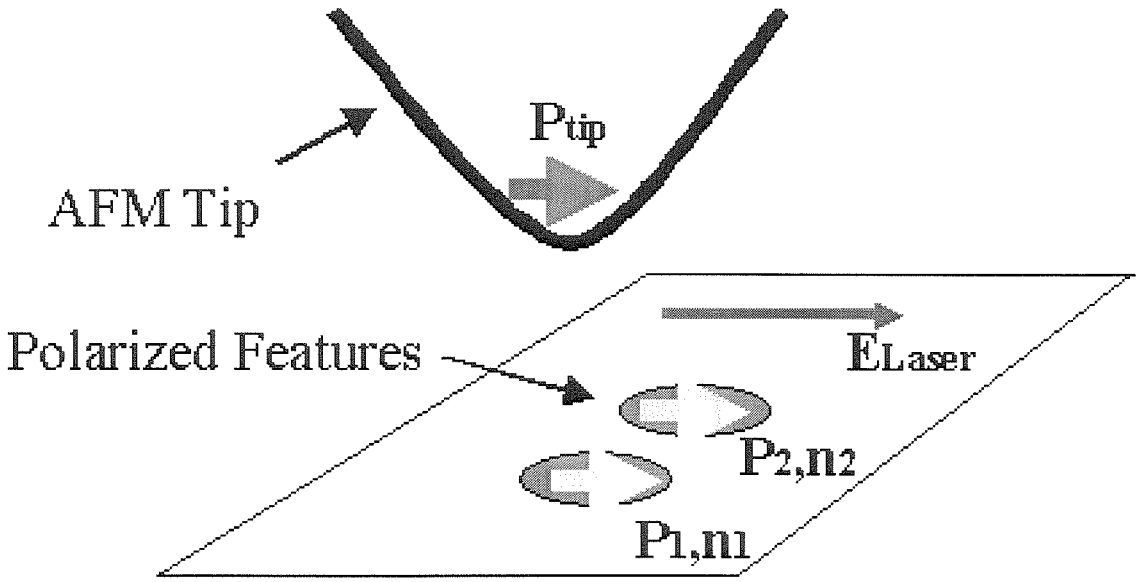

Figure 3.1: Schematic of the dipole configuration to be simulated representing the two spheres on a plane under illumination. The laser field polarizes all the features which then interact in the near-field to affect the far-field radiation.

tip. The value of the polarizability, α_s, is dependent on the structure of the sample and the wavelength of the external laser, and for spheres is expressed as

$$\alpha_s = \frac{\epsilon_s/\epsilon_0 - 1}{\epsilon_s/\epsilon_0 + 2} R_s^3 \tag{3.3}$$

where R_s is the radius and ϵ_s is the dielectric constant of the sphere. The dependence of the index on wavelength is contained in ϵ_s, since $n = \sqrt{\epsilon_s}$. The full expression for the near-field of the sample, accurate to first order in the external field and taking into account the finite dimensions of the dipole, is

$$\vec{E}_s = \frac{\alpha_s |\vec{E}_{laser}|}{2R_s^3} \left(\begin{array}{c} \left[\frac{(R-\cos\theta)\cos\omega t_-}{d_+^{3/2}} - \frac{\cos(R+\cos\theta)\omega t_+}{d_-^{3/2}} - \frac{\omega R_s \sin\omega t_-}{c d_+} - \frac{\omega R_s \sin\omega t_+}{c d_-} \right] \hat{e}_r \\ \sin\theta \left[\frac{\cos\omega t_-}{d_+^{3/2}} + \frac{\cos\omega t_+}{d_-^{3/2}} - \frac{\omega R_s \sin\omega t_-}{c d_+} - \frac{\omega R_s \sin\omega t_+}{c d_-} \right] \hat{e}_\theta \end{array} \right) \tag{3.4}$$

where r is the distance between the center of the sample and the observation point, θ is the angle between the sample's dipole moment and the vector locating the observation point, t is time, $d_\pm = 1 + R^2 \pm 2R\cos\theta$, $t_\pm = t - R_s d_\pm^{1/2}/c$ and $R = r/R_s$. This near-field, E_s, changes the induced dipole moment of the AFM tip and effectively

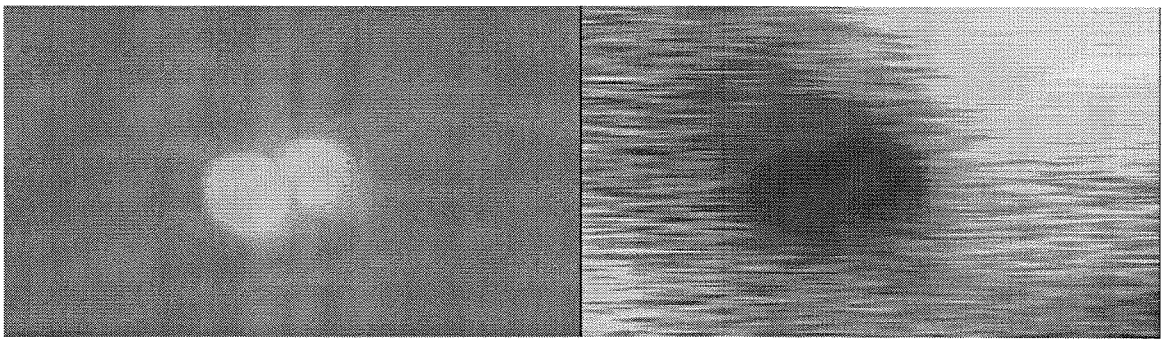

Figure 3.2: Experimental data to be compared to the simulations. Left: AFM image is of two adjacent 50 nm diameter polystyrene nanospheres on glass. Right: Apertureless microscope data taken with the illuminating laser randomly polarized.

modulates the scattered intensity measured at the detector as the AFM tip scans across the sample.

We have imaged polystyrene nanospheres of diameters ranging from 30 to 200 nm. In order to compare the simulations to the experimental data, the AFM image in Figure 3.2 is of two adjacent 50nm diameter polystyrene beads on glass. Also shown is apertureless microscope data taken with the illuminating laser randomly polarized.

Figures 3.3, 3.4, 3.6, and 3.7 are simulations which show the important features of the dipole model, notably the dependence on polarization, index and tip size. The AFM image is used as a topographical template for the simulations since the dipole field influencing the tip will be a function of the center-to-center separation between tip and sample. To the topography we add the locations and other pertinent information about the sample dipoles induced by the external laser polarization. With this information we can determine the scattered intensity at any point to construct the final image. Unless otherwise stated, all simulations use the parameters R_{tip}=10nm, n_{sample}=1.6, λ_{laser}=632.8nm. The scales in the simulations are normalized to unity for the level of background scattering off of the AFM tip in the absence of modulation due to the sample's electric field. All are linear plots of the normalized intensity with full scale from 0.70(black) to 1.8(white). Values outside this intensity range are clipped to the minimum or maximum value accordingly. Figure 3.4 shows how the near field of the dipole orients itself with the polarization of the external laser source.

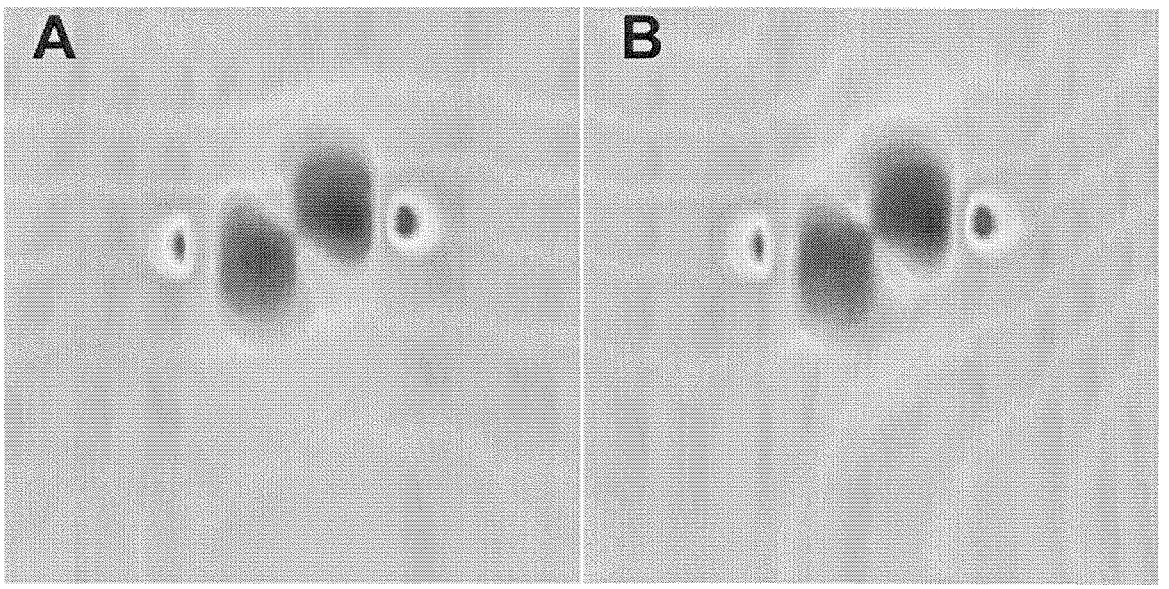

Figure 3.3: Simulations of the apertureless microscope image of two spheres on a plane under different illuminating wavelengths. The results indicate that the resolution is limited by the tip and not the illuminating wavelength. A. $\lambda = 630$nm and B. $\lambda = 543$nm

The figures suggest that an enhancement in resolution could be obtained with the proper orientation of the source polarization. Our initial experiments have shown a definite dependence on the polarization of the external laser source as indicated in Figure 3.5.

Figure 3.7 indicates how resolution decreases with increasing tip size. Although a larger tip radius means a larger scattering cross section and hence more signal, the change in signal intensity with respect to the background scattering is reduced with a larger tip. Figure 3.6 shows how the image intensity changes for features with different bulk indices of refraction. These images show clearly that the dipole model can account for differences in optical properties. Experimental images of adjacent features with different indices of refraction will be discussed in the next chapter.

3.3 Conclusions

In conclusion, we have used a dipole-dipole scattering model to demonstrate that the apertureless technique can, in theory, provide information about a sample that

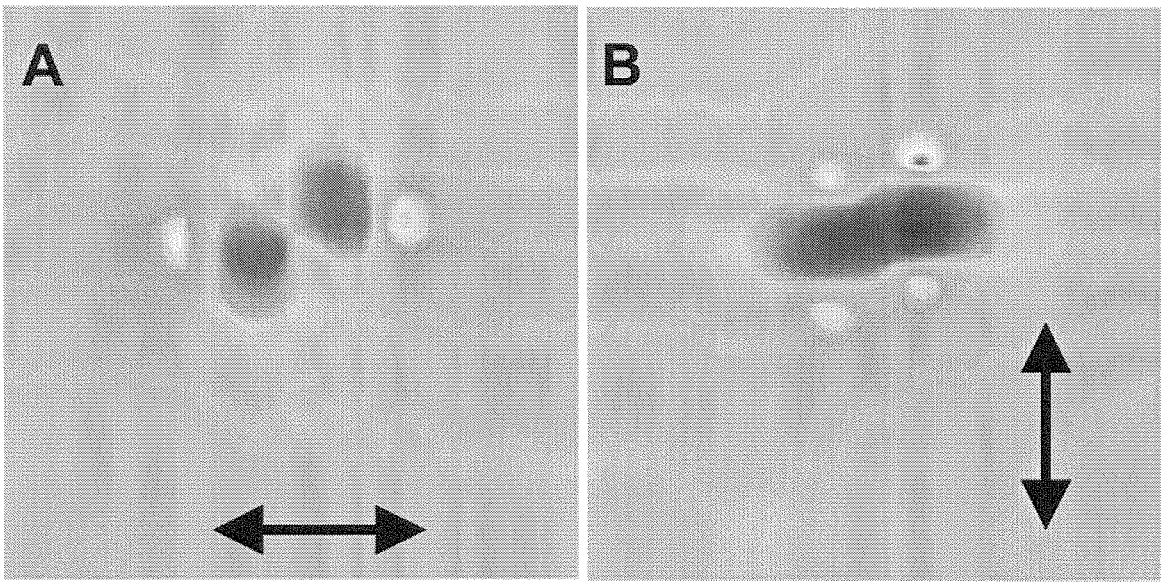

Figure 3.4: Simulations of the apertureless microscope image of two spheres on plane under different illuminating polarizations at a wavelength of $\lambda = 630$nm. The angular distribution of the dipole radiation aligned along the axis of polarization is clearly visible.

is indeed optical in nature. The model contains no fitting parameters; all physical constants used are well known or easily measured. A significant result from the dipole scattering model that agrees with experiments is a strong polarization dependence in the images as well as destructive interference lowering the signal intensity when the tip is above the sample. Both of these important observations shed light on the physical mechanism of the near-field interaction.

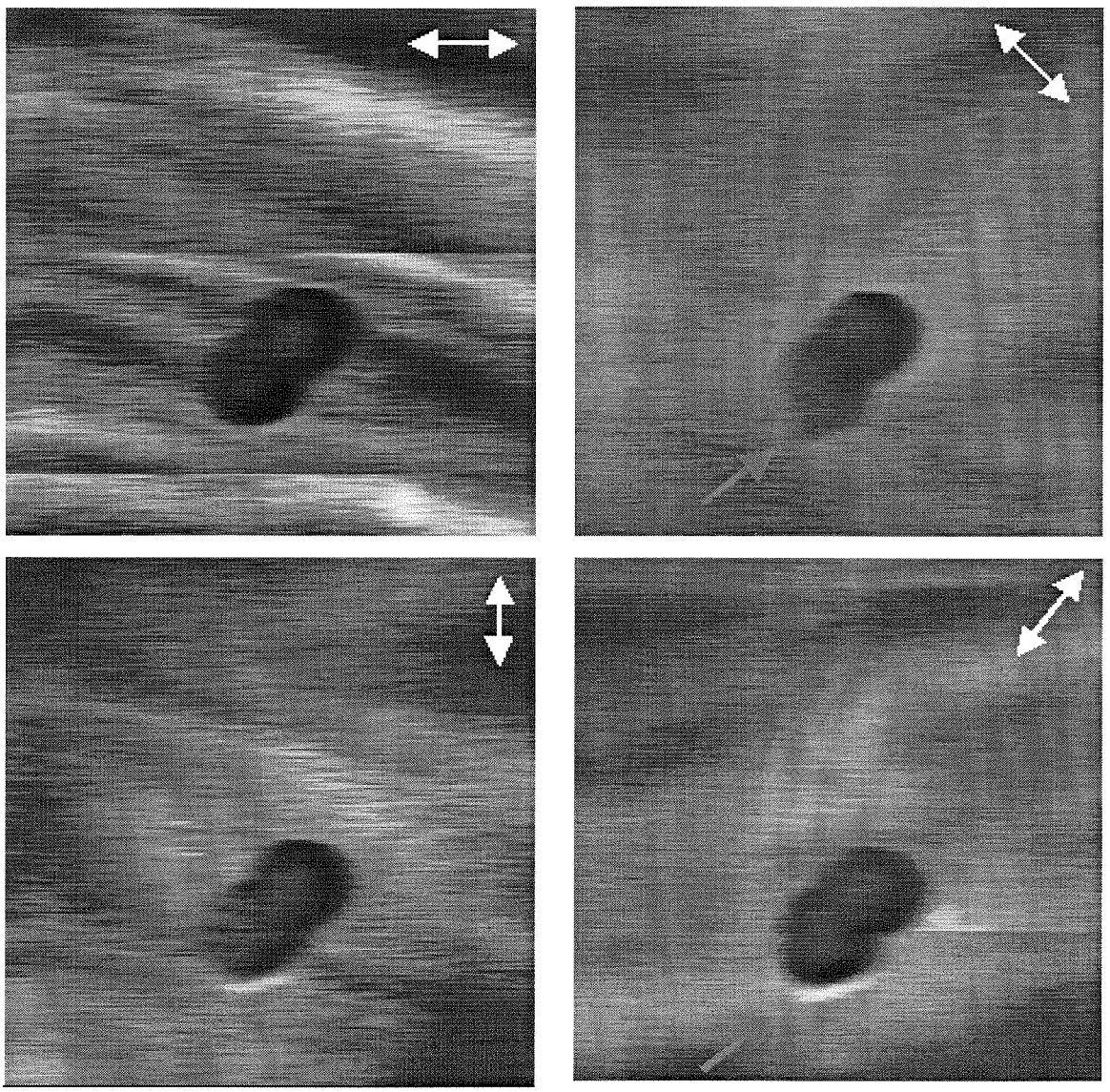

Figure 3.5: Aperturless microscope image of two spheres on plane under different illuminating polarizations. The wavelength was $\lambda = 630$nm and the polarization is indicated in the upper right corner of each of the four figures. The angular distribution of the dipole radiation aligned along the axis of polarization is clearly visible as indicated by the arrows and is in agreement with the simulations.

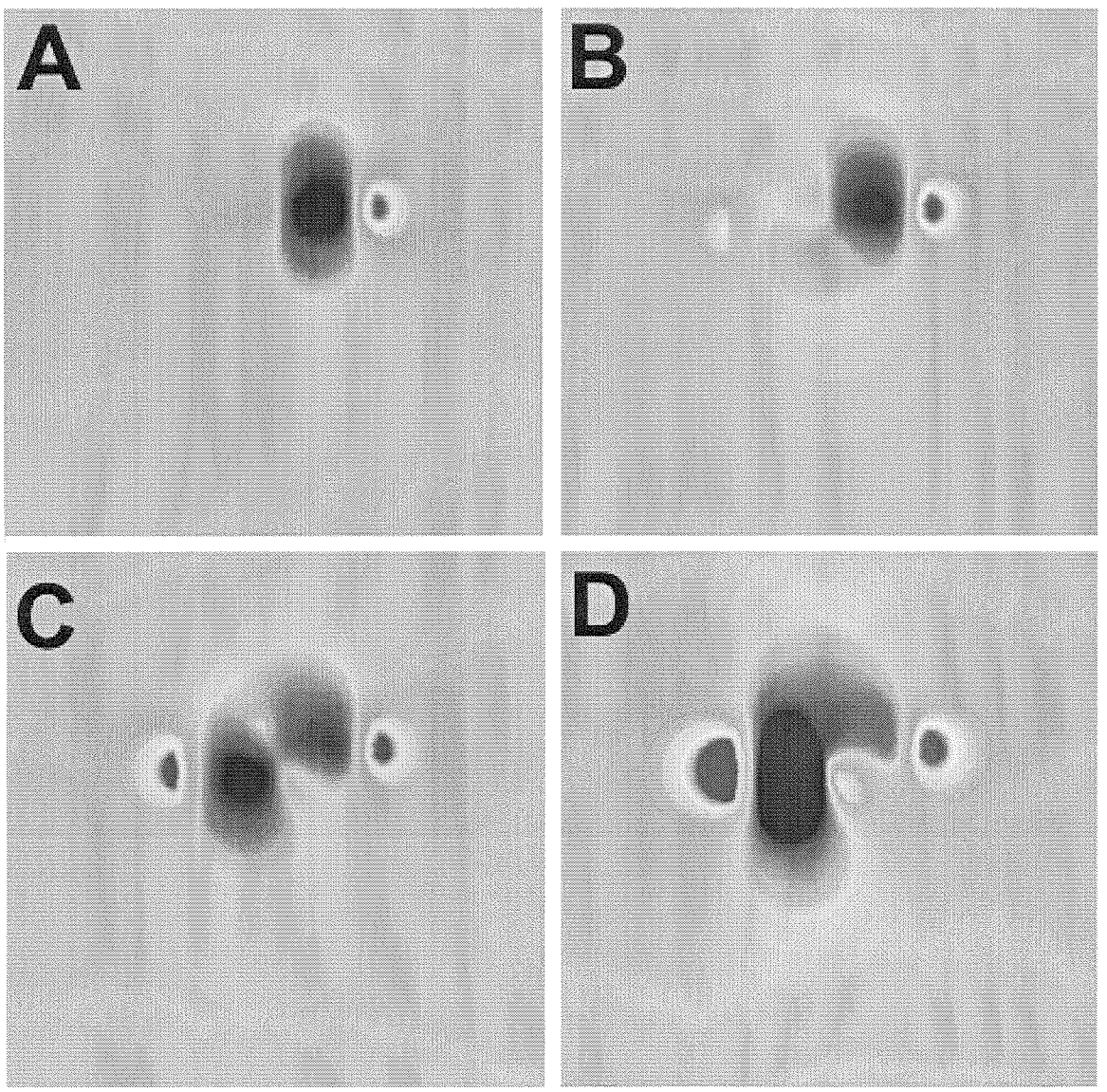

Figure 3.6: Simulations of the apertureless microscope image of two spheres on plane. The index of refraction of the sphere on the left in each of the images changes from 1.0 in image A to 1.3 in B, 1.8 in C, and 4.0 in D. The index of the sphere on the right is held constant at n = 1.6.

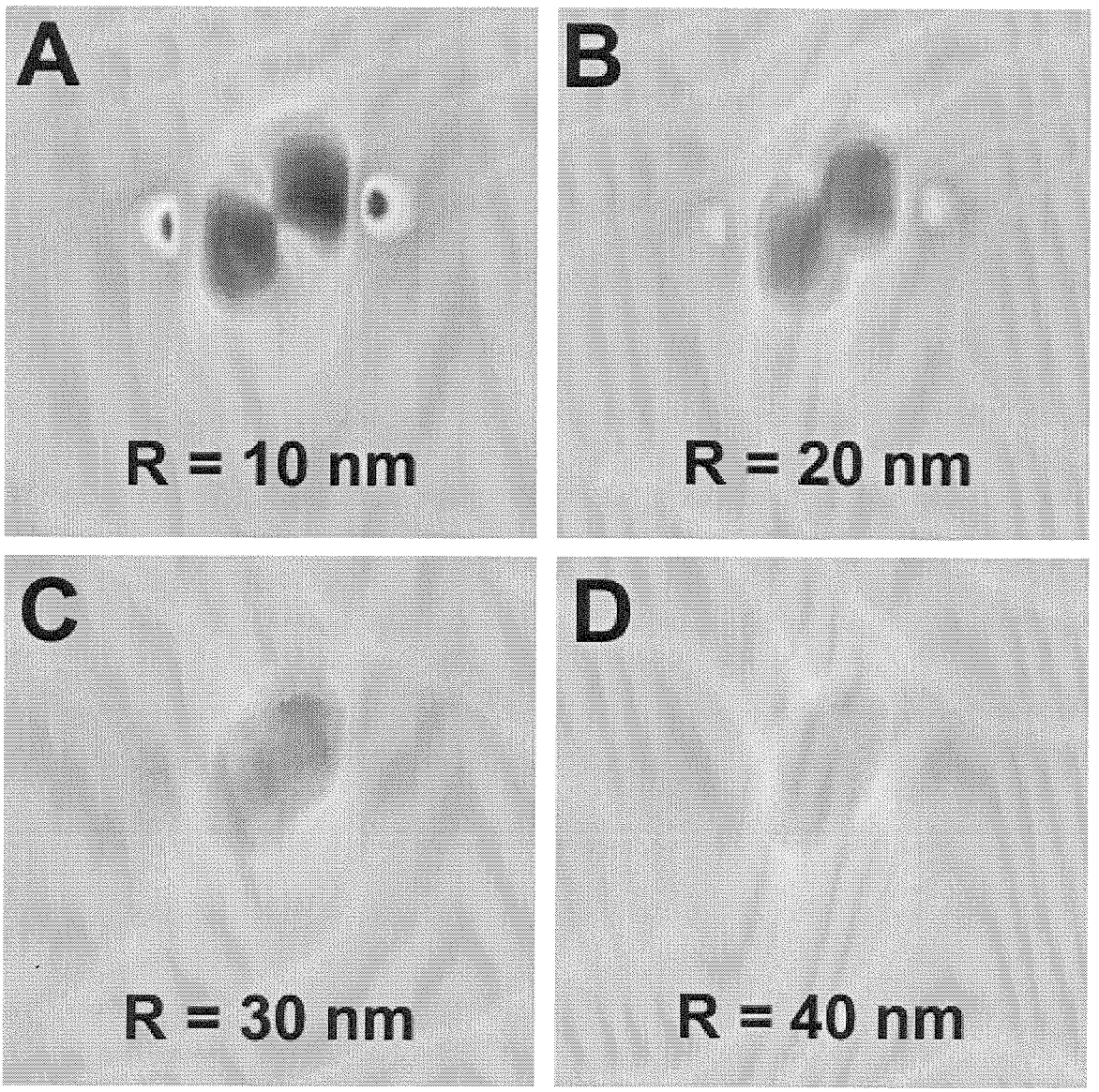

Figure 3.7: Simulations of the effect of tip size on the resolution of the apertureless technique. R indicates the radius of curvature of the tip used in the simulations. Clearly, as the tip increases in size resolution is lost as well as washing out the angular dependence of the dipole radiation.

Bibliography

[1] D. Courjon and C. Bainier, Rep. Prog. Phys. **57**, 989 (1994).

[2] H. K. Wickramasinghe and C. C. Williams, Apertureless Near Field Optical Microscope, U.S. Patent 4,947,034 (April 28, 1989).

[3] F. Zenhausern, M. P. O'Boyle, and H. K. Wickramasinghe, *Appl. Phys. Lett.* **65**, 1623 (1994).

[4] F. Zenhausern, Y. Martin, and H. K. Wickramasinghe, *Science* **269**, 1083 (1995).

[5] M. Born and E. Wolf, *Principles of Optics* 6^{th} Ed. Cambridge University Press, 1980.

[6] B. Hecht, H. Bielefeldt, Y. Inouye, L. Novotny, and D. W. Pohl, *J. Appl. Phys.* **81**, 2492 (1997).

[7] J.D. Jackson, *Classical Electrodynamics*, 2nd ed. (John Wiley, New York, 1975).

[8] E. Betzig, M. Isaacson, and A. Lewis, *Appl. Phys. Lett.* **51**, 2088 (1987).

[9] N. Garcia and M. Nieto-Vesperinas, *Appl. Phys. Lett.* **66**, 3399 (1995).

[10] Y. Martin, F. Zenhausern, and H. K. Wickramasinghe, *Appl. Phys. Lett.* **68**, 2475 (1996).

[11] Y. Martin, S. Rishton, and H. K. Wickramasinghe, *Appl. Phys. Lett.* **71**, 1 (1997).

[12] C. Schönenberger and S. F. Alvarado, Rev. Sci. Inst. **60**, 3131 (1989).

[13] M. Pluta, Advanced Light Microscopy. Vol. 1 (1988).

Chapter 4 Apertureless Microscopy: Experiment

4.1 Introduction

In this chapter, we describe a series of experiments to explore the limits of spatial resolution, the measurement of optical properties, and applications of apertureless microscopy. We feel that there are two important issues. First is the decoupling of the measured optical signal from topography. Second is the discrimination of local variations of susceptibility below the diffraction limit. The first issue has been examined by Hecht et al. [1] for NSOM and is important since crosstalk in the optical image due to topography can give rise to misleading image artifacts. In their paper, they give the following criteria to satisfy before a near-field optical (NFO) image can be "credible"

1. The NFO image is obtained in constant height or constant intensity mode. Constant height mode is taken to mean that the probe is scanned in a plane parallel to the average surface of the sample. Constant intensity mode is when the probe-sample distance is regulated to give a constant intensity at the detector.

2. The NFO image is taken in constant gap mode but has the following characteristics. Constant gap mode meaning that the probe-sample distance is constant.

2a. Topographic and NFO images are highly uncorrelated. For example, magnetic force microscopy can also suffer from topographic artifacts; however, images of magnetic tape show that the tracks are unrelated to the topographic structure.

2b. Correlated structures are displaced by a constant amount.

2c. The resolution of the NFO and scanning force images are clearly different.

Although Wickramasinghe has demonstrated apertureless microscopy on dye molecules and dyed samples at different wavelengths, [2] no attempt was made to differentiate between objects. Hence, the second issue has not yet been examined in a controlled set of experiments. We examine the decoupling and differentiation issues first then introduce applications at the end of the chapter.

4.2 Instrument Description

In our scanning apertureless microscope, an optical microscope focuses a laser to a diffraction limited spot which is perturbed by an AFM tip operating in tapping mode where the RMS voltage of an oscillating tip at resonance is kept constant. Unfortunately, there is some confusion over the use of the term "tapping mode." The way it is used here is fundamentally different than the "tapping mode" described in Reference [9] where the entire cantilever position is modulated at a frequency much lower than the resonance frequency. When the tip oscillation amplitude being kept constant, the average tip-sample distance is constant over the lock-in integration time. Therefore, there is less risk of introducing artifacts that could be due to simply measuring the cantilever position with light reflected from the cantilever. In previous experiments, however, the entire cantilever position is being modulated relative to the sample so there is a great risk that the images are simply a more accurate measurement of the tip position. (Ref. [10] is a reference to the Tapping Mode patent for the correct use of the term.) On the return path, a spatial filter blocks light that may be reflected from the shank of the cantilever and passes that from the tip. A laser line filter in the return path passes only $\lambda = 632.8$nm, excluding light from the AFM laser ($\lambda = 670$nm). The light then passes through a Wollaston prism and onto a differential photodiode where optical intensity or phase is measured with an EG&G 5302 lock-in amplifier. The drive signal for the AFM is used as the reference frequency [11]. The SAM used a Nikon Diaphot 200 inverted optical microscope as the platform with a Digital Instruments Bioscope as the AFM component. In this case, the objective had

a numerical aperture (NA) of 0.75 and the laser was a Spectra Physics 145-01 HeNe, $\lambda = 632.8$nm. A schematic of the optical path in the experiment is shown in Figure 4.1. A critical element of the apparatus is the laser line filter to reject ambient light and any signal from the AFM control laser. Since the silicon cantilever thickness of 3.5μm is roughly the light penetration depth at the AFM laser wavelength, stray light can have a significant impact on the results.

4.2.1 Nanospheres

A proposed explanation for the NFO signal has been described previously in two theories [12, 13]. To reiterate, one is based on a theory of coupled dipoles. The result of this theory is that the modification of the incident field is due to the interaction between the tip and sample induced dipoles. The other theory due to Garcia accounts for refractive index variations of the sample and scattering from a spherical tip. In either case, the perturbation signal contains a contribution from both the tip and the sample refractive indices (susceptibility). Measurement of these perturbations as the tip scans over the sample forms the NFO image. The feature common to both theories under consideration here is the contribution from the tip and sample susceptibilities. Since the signal depends on the local susceptibility of the sample, it should be possible to measure adjacent objects which have different susceptibilities and are smaller than the diffraction limit.

To address the issue of discriminating the susceptibility below the diffraction limit it is necessary to determine the resolution of the instrument. To do this in a controlled way, polystyrene nanosphere size standards in water suspension were deposited on a glass cover-slip by dilution to an appropriate density, pipetting a small amount onto the glass, and letting the water evaporate in a dry nitrogen environment. The nanospheres had a tendency to clump together so some searching was required to find a reasonable distribution.

Dyed and undyed nanospheres of the same size were imaged to decouple any potential topographic signal from that due to the near-field optical interaction. Since

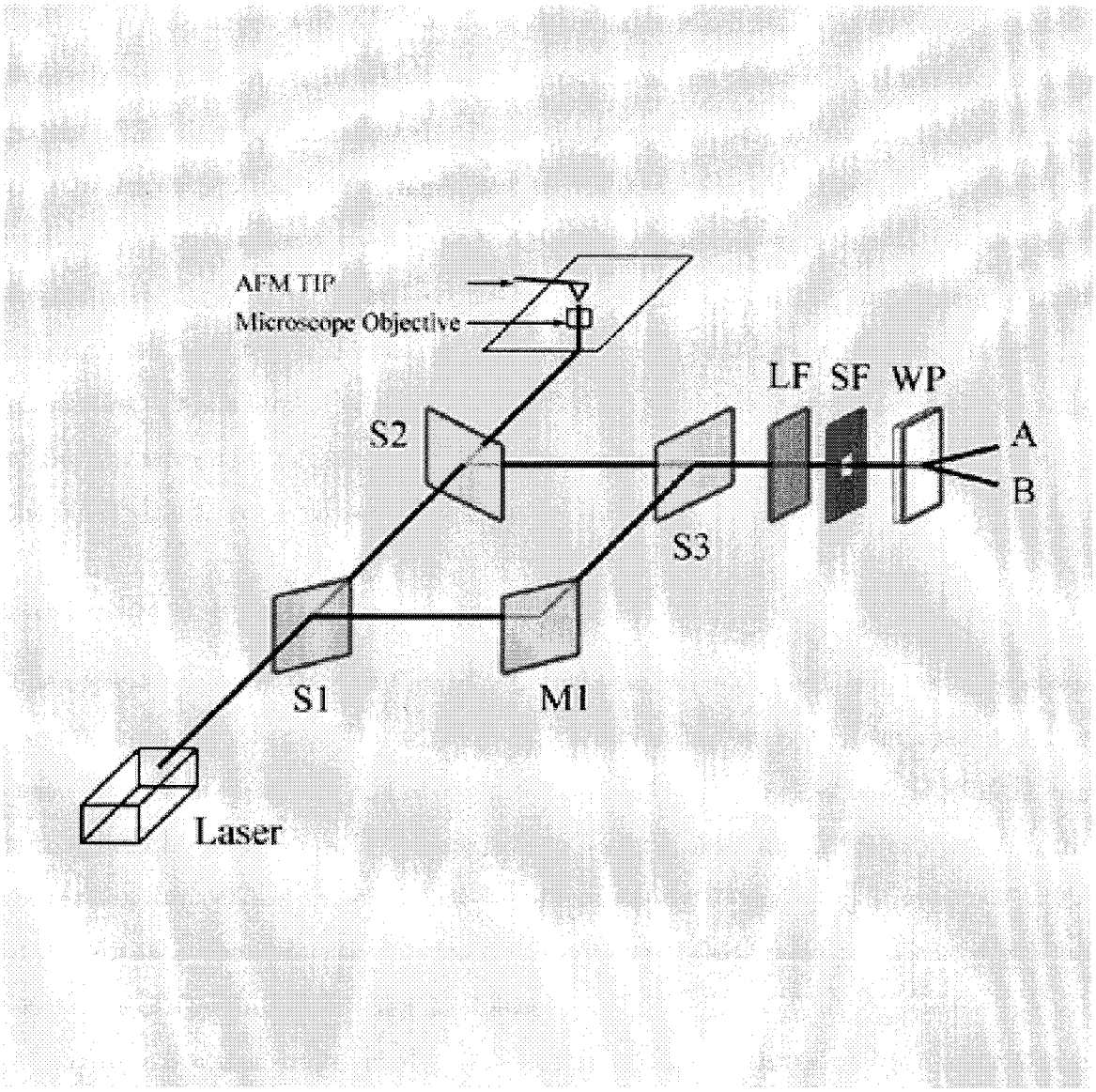

Figure 4.1: Schematic of the apparatus. Light from a HeNe laser is split into a reference beam and a sample beam at the beam splitter S1. The sample beam continues to the beam splitter, S2, where part of it is dumped and part of it is focussed onto the AFM tip by a microscope objective (NA 0.75). Since the depth of field of the microscope objective is only 1 μm, compared to a tip height of 15μm, only the apex of the tip is imaged. Light scattered from the AFM tip is collected by the same objective and combined with the reference beam (reflected from mirror M1) at the beam splitter, S3. A laser line filter, LF, then rejects all light except the laser light. A spatial filter, SF, passes only light from the AFM tip while excluding light that may be reflected from the cantilever. The light is then split by a Wollaston prism, WP, and incident on differential photodiodes, A and B.

any artifacts due to the tip motion will be identical for all the objects (same shape and size), any differences will be a result of their susceptibilities. We used polysciences fluoresbrite nanospheres in which the dye resides in the outer 10% of the nanosphere radius. The fluorescein based dye is propriatory but has a fluorescence spectrum that peaks at 540 nm and extends out to 700 nm. For this experiment, the dyed and undyed nanospheres were mixed in equal proportions and then deposited on a coverslip in the manner described above and imaged with the instrument. Dyed nanospheres have the additional advantage that they all have the same mechanical properties. This is important for lock-in detection since both the phase and amplitude of the tip vibration will change as the tip scans over different materials. To detect the NFO signal, we measured optical intensity.

Resolution

The optical intensity image of Figure 2 shows the small region at the interface between two 200 nm nanospheres. The scan size is 250 nm so the entire nanosphere cannot be seen. From this image we can observe that the edge response of the SAM is 15 nm and the minimum observable feature is 3 nm in size. As a matter of comparison, the diffraction limit of the objective lens is approximately 700 nm. [14] Since the FWHM of a step is a commonly used resolution criterion, this is closer to the predicted resolution of Garcia rather than Zenhausern.

Figure 4.3 was also obtained by measuring optical intensity and is a scan of two adjacent, identical 50 nm nanospheres. Since the two are still distinguishable, and 50 nm nanospheres were the smallest available to us at the time, we can say that the resolution of the SAM is better than 50 nm. Later, we obtained nanospheres 30 nm in diameter which could also be detected as shown in Figure 4.4; however, 30 nm spheres clump together significantly and we could not find an instance of only two adjacent spheres. Notice that the destructive interference on the background for the measured signal in Figure 4.3 corresponds with the theoretical prediction from the dipole scattering model. More complicated geometries may not have as simple an image and are the subject of future simulations.

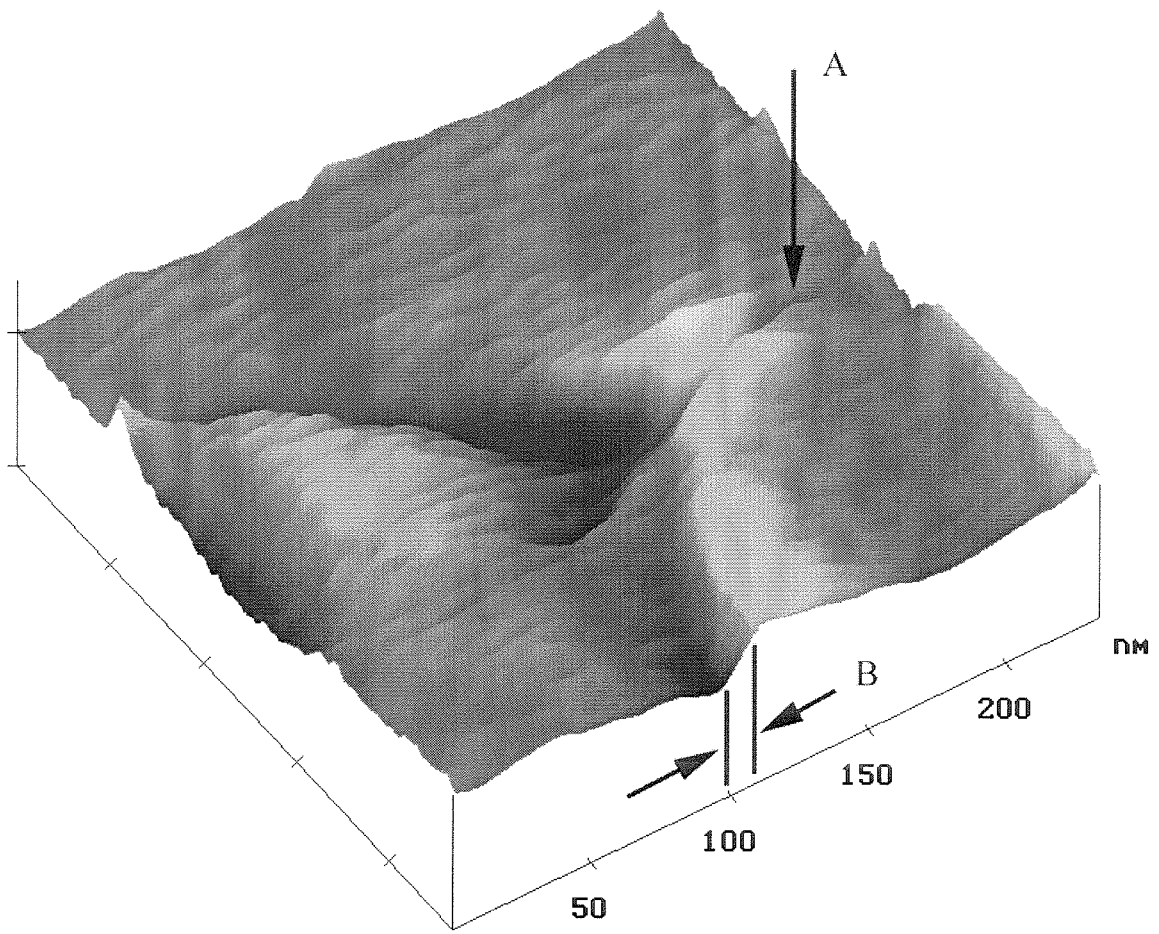

Figure 4.2: Raw NFO image from the microscope of a region between two adjacent 200nm polystyrene nanospheres with a 3nm minimum observable feature size (A) and a 15nm step response (B).

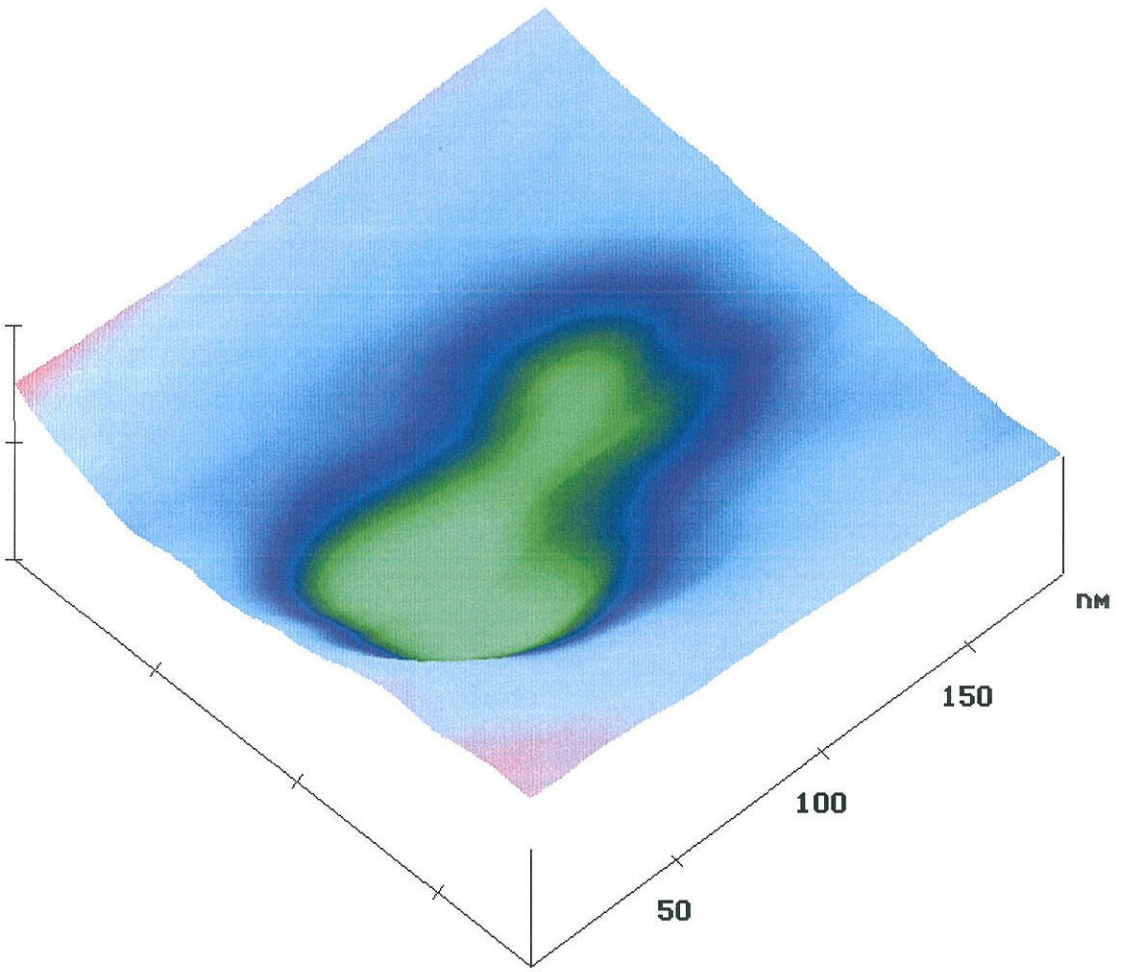

Figure 4.3: Raw NFO image from the microscope demonstrating 50nm resolution. The sample is two identical nanospheres adsorbed on a cover slip and imaged by detecting scattered amplitude. The scan size is 180nm.

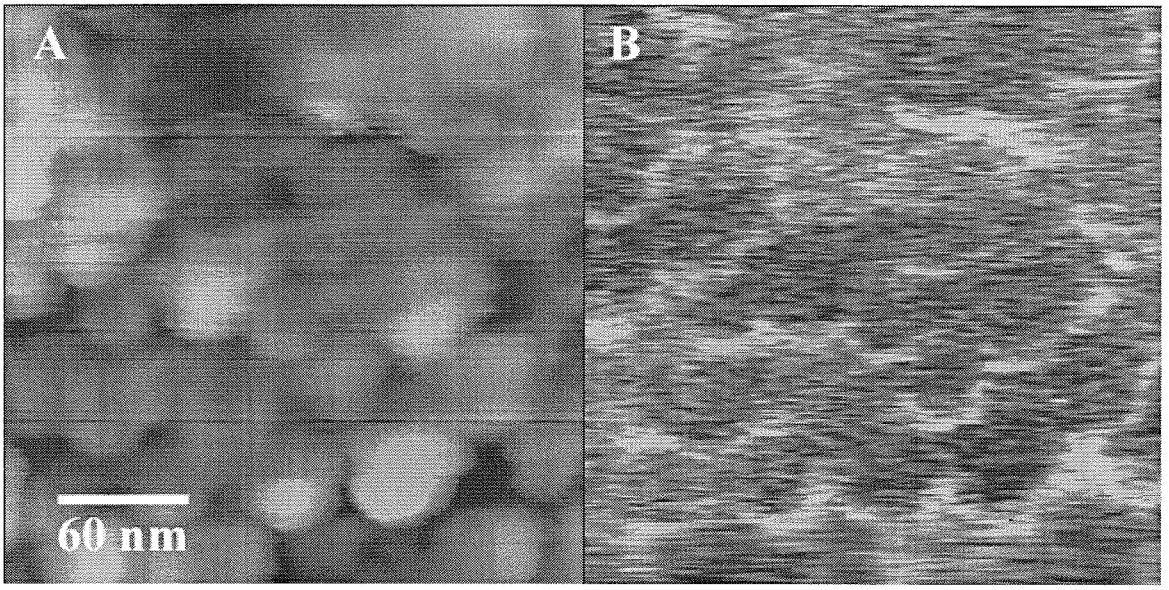

Figure 4.4: Raw NFO image from the microscope demonstrating 30nm resolution. The sample is a layer of 30nm nanospheres adsorbed to a glass cover-slip. The noise in the AFM image is the tip pushing on the spheres.

Optical phase imaging is shown in Figure 4.5. Although noisy, clusters of 50nm nanospheres roughly 200 nm in size are just resolved. Resolution here is conservatively taken to mean a two point resolution similar to the Rayleigh criterion where two sources are considered resolved when the intensity maximum of one falls on the intensity minimum of the other and not edge sharpness or minimum feature size .

At present, the resolution of the instrument appears to be limited by the AFM tip radius of curvature since switching to sharper tips gives sharper features.

Both the issues of topographic artifacts and the measurement of local susceptibility are dealt with in Figure 4.6. Dyed and undyed nanospheres are distinguishable with adjacent nanospheres appearing as bright and dark. We attribute this to the properties of the dye since any topographic artifacts that may exist will be identical for the same size and shape nanospheres. A good indication that the dye does affect the susceptability is illustrated in Figure 4.7. Samples that were previously imaged were reused some time later when the dye had leached out of the nanospheres creating a "halo" around an otherwise dark sphere in the optical image.

Comparing the AFM and SAM images, from the point of view of meeting the

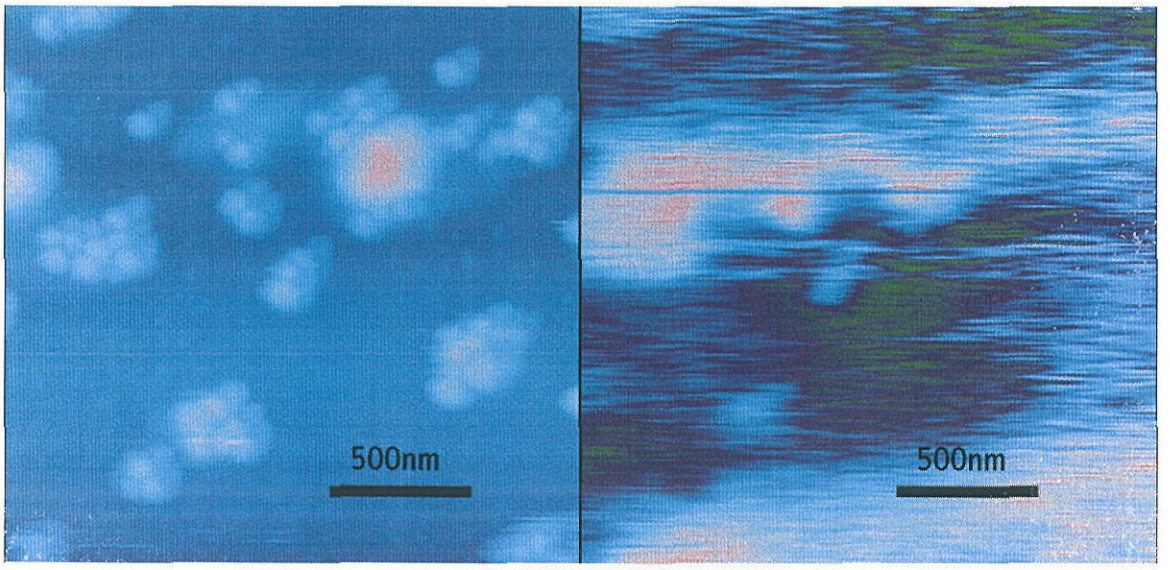

Figure 4.5: Clusters of 50 nm nanospheres. Left: Simultaneously acquired AFM data. Right: Raw NFO image from the microscope demonstrating approximately 200nm resolution by detecting optical phase.

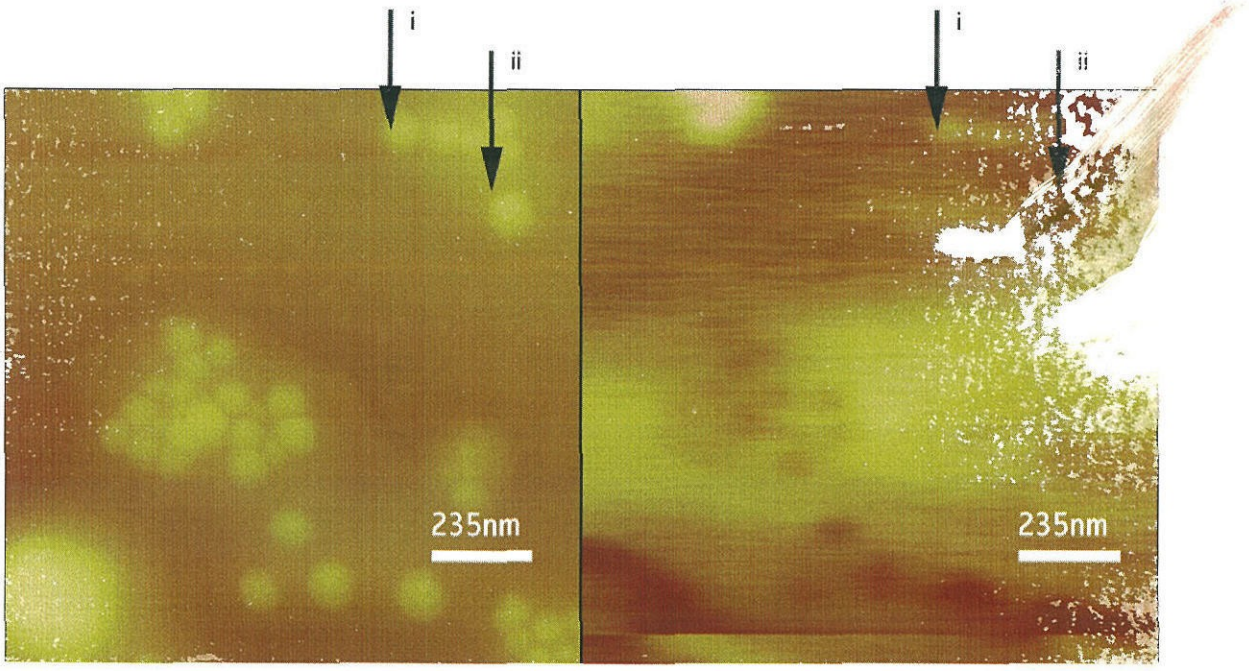

Figure 4.6: 50nm scale optical property discrimination. False color image of differently dyed 50nm nanospheres. The left image is AFM data, the right image is the raw NFO data from the microscope. i) 50nm spheres resolved by the microscope which show up as "low" next to ii) 50nm spheres appearing as "high."

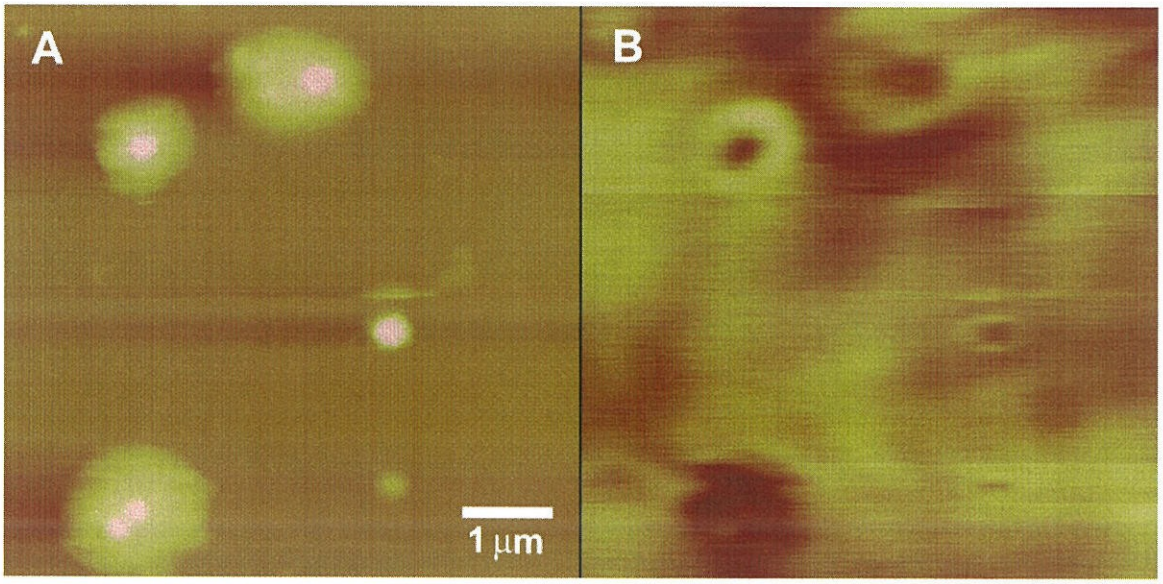

Figure 4.7: A. AFM image of an old sample of dyed nanospheres. B. Corresponding apertureless microscope image indicating that the dye has leached out of the spheres creating a halo in the near-field optical image.

criteria set down by Hecht et al. [1] for a true NFO image, one finds that several of them are met. First, the resolutions of the AFM and SAM are clearly different. Second, in the case of the dyed size standards, the two images are uncorrelated. Namely, nanospheres that appear identical to the AFM appear different in the NFO image. Third, the AFM and NFO images are displaced by a constant amount. Finally, the images were taken in tapping mode which is nearly equivalent to constant height mode (CHM). There is, however, some surface tracking that takes place in tapping mode operation in order to keep the oscillation amplitude constant. An example of the artifacts that are introduced in constant gap mode is given in Figure 4.8 where the optical data was collected when the AFM is lifted off a constant distance (30 nm) from the sample surface.

To summarize, we have carried out a series of controlled experiments using nanosphere size standards where we observe significant differences in resolution and structure between the AFM image and the simultaneously acquired near-field optical image. For nanospheres 30, 50 and 200 nm in diameter, the two point resolution was at least 200 nm when detecting optical phase and 30 nm when detecting optical inten-

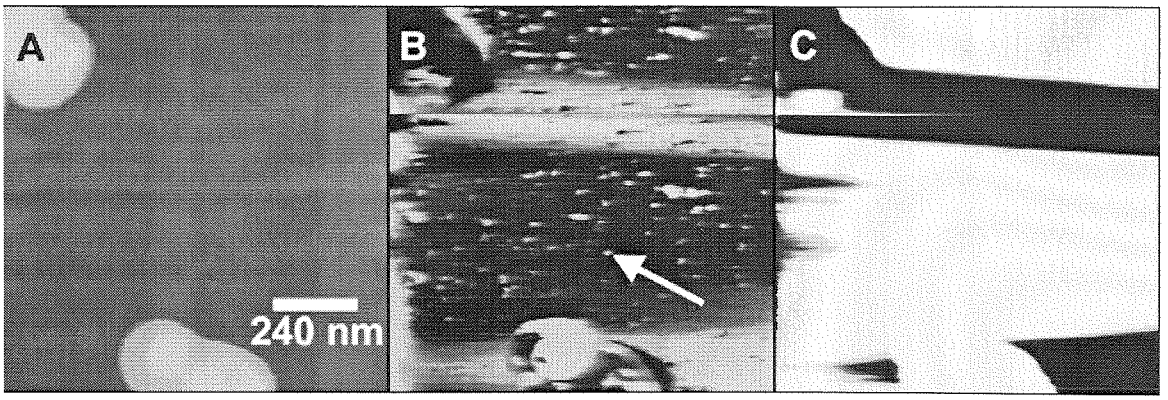

Figure 4.8: A. AFM image of nanospheres on an anti-reflection film. B. Apertureless microscope image taken in tapping mode simultaneously with the AFM data. C. Apertureless microscope image representing constant gap gap contribution to the optical signal. In this case the tip-sample gap was maintained at 30 nm.

sity. The edge response was typically 15 nm and minimum observable features were on the order of 3 nm. Further, in experiments employing a mix of dyed and undyed nanospheres, we find that we can observe differences in the same NFO image for adjacent nanospheres which we attribute to differences in susceptibility. Therefore, we conclude that near field scanning apertureless microscopy not only meets the criteria for a NFO image but is also capable of measuring optical properties below the diffraction limit. We believe that this is the first demonstration that adjacent objects with different susceptibilities and sizes below the diffraction limit can be differentiated.

4.3 Applications

4.3.1 Anti-reflection films

We have studied anti-reflective thin films with the apertureless microscope as shown in Figure 4.9. These films were found to be quite sensitive to perturbations in the interference condition as indicated by Figure 4.10. Although variations in the topography of the film are only 9 Åin height, they show up quite clearly as an enhancement in the near-field image. The smallest areas in Figure 4.9 are 10 nm in size and as a result could not be seen with conventional optics.

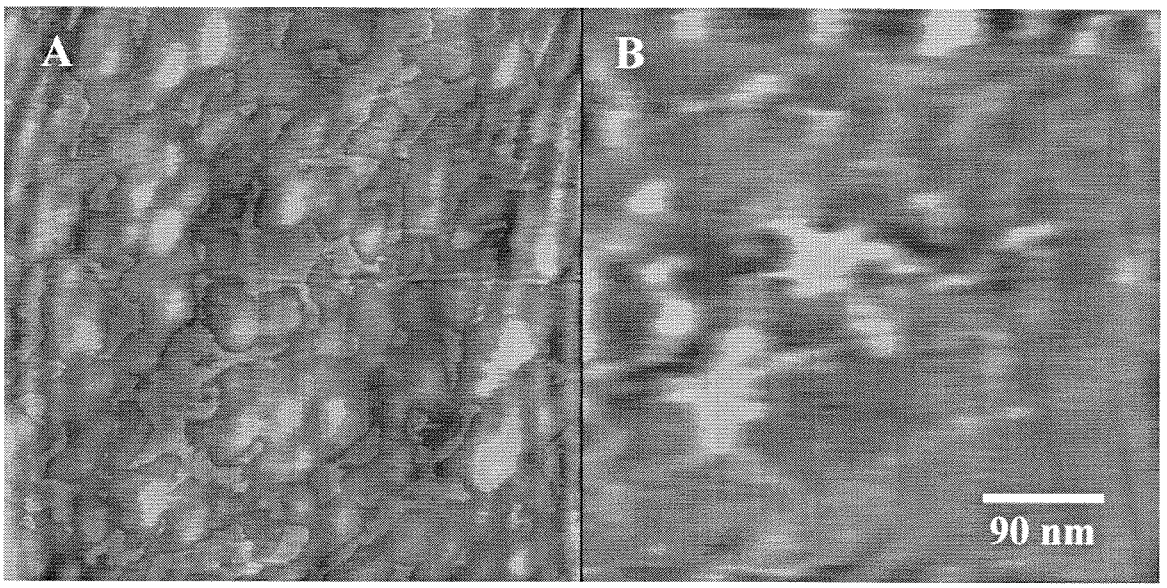

Figure 4.9: Aperture less microscope image of anti-reflection thin film at 633nm.

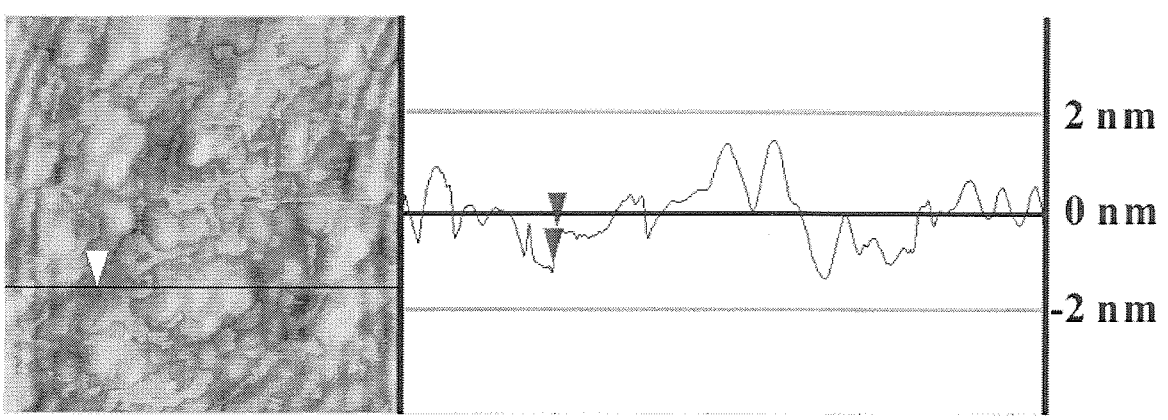

Figure 4.10: AFM image and section indicating topography of only 0.9nm.

4.3.2 Chromosomes

The Near-field optical structure of the centromere region of undyed polytene chromosomes has been observed by using the apertureless microscope in intensity detection mode. The centromere is of primary importance to the functioning of the chromosome in the cell during cell division. It is also particularly interesting for structural/optical studies since its DNA repeat sequences are highly conserved among organisms and it is possible that they play a part in the centromere self assembly [21–23]. Polytene chromosomes on glass were obtained commercially (Bioforce labs) and dessicated. They were imaged by positioning the AFM tip on the chromosome with the inverted optical microscope, since chromosomes are many microns in size, and then engaging the SAM.

Figure 4.11 is a result of the measurement of polytene chromosomes. The first three images (4.11 A, B, C) are a series of AFM scans to indicate where on the chromosome the near-field optical data was taken. The fourth image in the series is the raw near-field optical signal which was obtained simultaneously with the AFM data. The small features are approximately 100nm in size and are believed to represent the near field structure of the chromosome since they are not in direct correspondence with the topography as determined by the AFM. Since chromosomes are both structurally and chemically complicated, it is believed that future spectroscopic studies will be necessary to extract the function of these features that cannot be determined by single wavelength illumination.

In summary, we have demonstrated a new application of scanning apertureless microscopy to the near-field optical imaging of chromosomes. Structure 100nm in size has been observed and was not simply a measure of the topography. Future applications in biology could include apertureless imaging of viruses (50 nm) or proteins (10 nm) since their size is within the demonstrated resolution of the SAM.

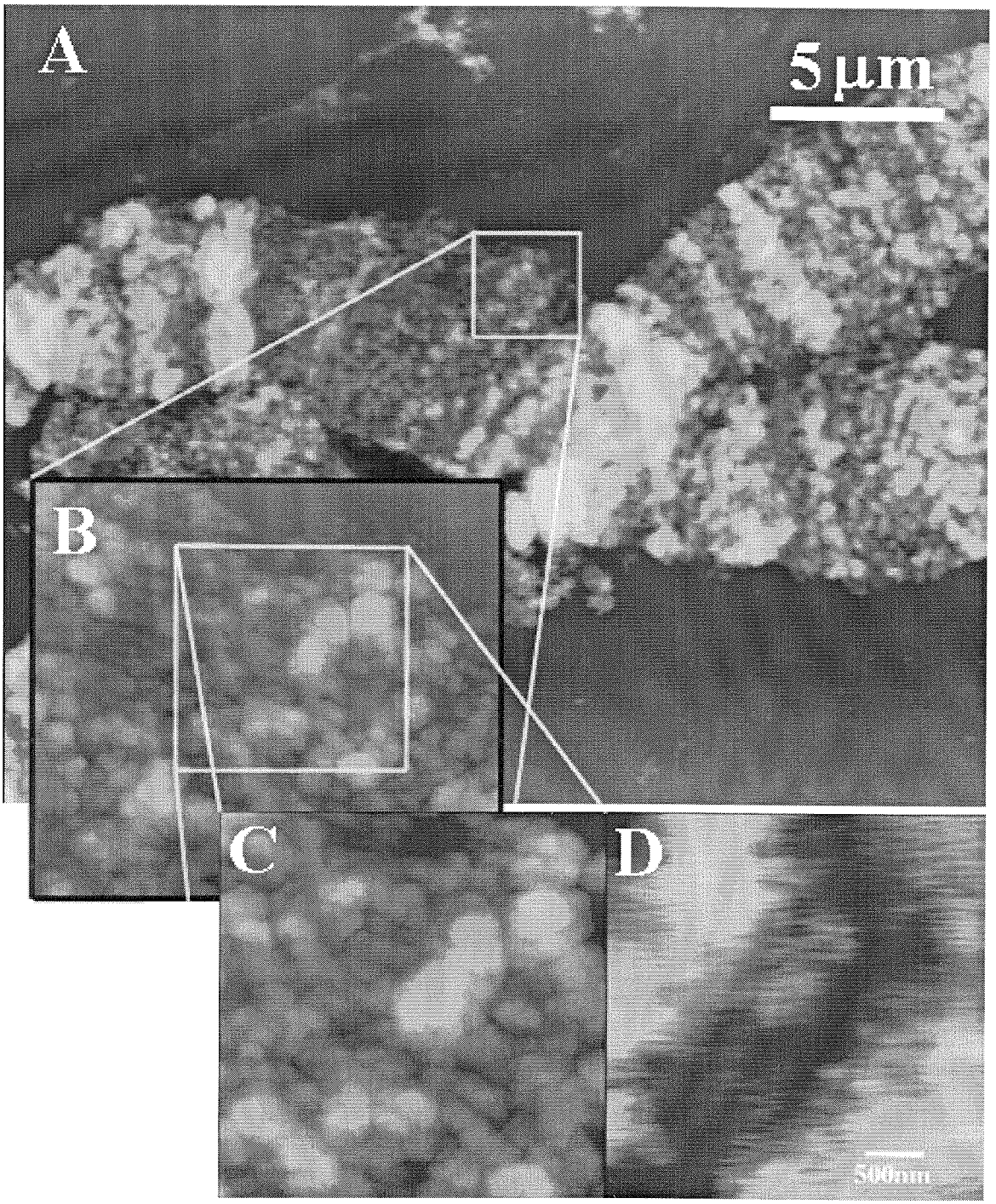

Figure 4.11: Apertureless microscopy of polytene chromosomes. A-C) AFM images of the chromosome with progressively smaller scan sizes of the regions indicated. D) Apertureless microscope image of a small region of the centromere of the chromosome simultaneously acquired with the AFM image C.

Bibliography

[1] B. Hecht, H. Bielefeldt, Y. Inouye, L. Novotny, and D. W. Pohl, *J. Appl. Phys.* **81**, 2492 (1997).

[2] Y. Martin, F. Zenhausern, and H. K. Wickramasinghe, *Appl. Phys. Lett.* **68**, 2475 (1996).

[3] M. Born and E. Wolf, *Principles of Optics* 6^{th} Ed. Cambridge University Press, 1980.

[4] D. Courjon and C. Bainier, Rep. Prog. Phys. **57**, 989 (1994).

[5] E. Betzig, M. Isaacson, and A. Lewis, *Appl. Phys. Lett.* **51**, 2088 (1987).

[6] L. P. Ghislain and V. B. Elings, *Appl. Phys. Lett.* **72**, 2279 (1998).

[7] H. Hatano, Y. Inouye, and S. Kawata, Opt. Lett., **20** 1532 (1997).

[8] H. K. Wickramasinghe and C. C. Williams, Apertureless Near Field Optical Microscope, U.S. Patent 4,947,034 (April 28, 1989).

[9] F. Zenhausern, M. P. O'Boyle, and H. K. Wickramasinghe, *Appl. Phys. Lett.* **65**, 1623 (1994).

[10] V. B. Ellings and G. A. Gurley, Tapping Atomic Force Microscope, U.S. Patent 5,412,980 (May 9, 1995).

[11] C. Schönenberger and S. F. Alvarado, Rev. Sci. Inst. **60**, 3131 (1989).

[12] F. Zenhausern, Y. Martin, and H. K. Wickramasinghe, *Science* **269**, 1083 (1995).

[13] N. Garcia and M. Nieto-Vesperinas, *Appl. Phys. Lett.* **66**, 3399 (1995).

[14] M. Pluta, Advanced Light Microscopy. Vol. 1 (1988).

[15] H. F. Hamann, A. Gallagher, and D. J. Nesbitt. *Appl. Phys. Lett.* **73**, 1469 (1998).

[16] Y. Martin, S. Rishton, and H. K. Wickramasinghe, *Appl. Phys. Lett.* **71**, 1 (1997).

[17] A. Larech, R. Bachelot, P. Gleyzes, and A. C. Boccara Opt. Lett., 1315 (1996).

[18] R. Bachelot, P. Gleyzes, and A. C. Boccara Opt. Lett., 1924 (1995).

[19] R. Bachelot, G. Wurtz, and P. Royer *Appl. Phys. Lett.* **73**, 3333 (1998).

[20] C. Hubert and J. Levy *Appl. Phys. Lett.* **73**, 3229 (1998).

[21] M. S. Clark and W. J. Wall, *Chromosomes* Chapman and Hall, London, 1996.

[22] H. F. Willard, Current Opinion in Genetics and development **8**, 219 (1998).

[23] T. J. Yen and B. T. Schaar, Current Opinion in Cell Biology **8**, 381 (1996).

Part II

Semiconductor Applications of Force Microscopy

Chapter 5 Correlation Between the Surface Defect Distribution and Minority Carrier Diffusion Lengths in GaN

5.1 Introduction and Motivation

Gallium Nitride based devices are currently of great interest for optoelectronic [1–3] as well as high power and high temperature electronics [4, 5]. Since many of the the performance characteristics of bipolar devices are determined by the minority carrier transport properties (diffusion lengths and lifetimes) [6], it is useful to determine how they are affected by the defect structure. In the past it had been assumed that linear dislocations were electrically inert [7–9] since they had little effect on the performance or reliability of GaN light emitting diodes. However, the correlation between cathodoluminescence (CL) and surface morphology observed as dislocations terminating as pits in the surface shown by Rosner *et al.* indicated that linear dislocations are important in recombination processes. [10] Electron beam induced current (EBIC) measurements provide a way to directly measure the minority carrier diffusion length in semiconductors.

In the EBIC measurement, electron-hole pairs are generated by a high energy electron beam in an electron microscope near the Schottky contact of a Schottky diode. The high energy electrons create an excess of minority carriers which diffuse to the Schottky contact on the semiconductor. The resulting current in the diode is collected and measured as a function of the distance from the contact. Fitting the data to an exponential decay gives a direct measurement of the diffusion length.

In this chapter, we correlate the measured diffusion length with the defect structure measured by atomic force microscopy.

5.2 Experiment Outline

In the experiment, we determined both electron and hole diffusion lengths from EBIC measurements on material that was characterized by atomic force microscopy (AFM). We then compare the distribution of defect induced depressions on the surface with the measured diffusion lengths. Because the density of linear dislocations threading the GaN is believed to be approximately the same as those reaching the top surface of the film for thin films [7], the 2D AFM data should represent the 3D distribution of those dislocations. For thicker films, however, the density of threading dislocations reaching the surface of the film decreases with film thickness. Moreover, the AFM does not reveal all types of defects. Nevertheless, it is the non-uniform distribution of the defects and not their absolute number that is considered here.

5.2.1 Details of the AFM and EBIC Experiments

The AFM data was obtained using a Digital Instruments Multimode AFM operating in Tapping Mode and a Nanoscope IIIa controller. A cross check of the topographic data was performed using contact AFM with oxide sharpened tips and no significant differences were found. The EBIC experiments were conducted in a JEOL 6400V electron microscope with a GW Electronics pre-amplifier followed by GW Electronics specimen current amplifier or Keithly 486 picoammeter. The entire apparatus was enclosed in an active electromagnetic interference (EMI) cancellation cage as well as being mechanically isolated. A schematic of the experiment is illustrated in Figure 5.1. Due to the large concentration of holes in p-type sample (or electrons in UID n-type sample) compared to the generated electron-hole concentration, only minority carriers are effectively generated, assuming low electron beam currents. This is the reason why a p-type sample is required for measurement of electron (as a minority carrier) transport parameters, and n-type sample is required for measurement of hole transport properties.

Gold and Ti/Al/Ni/Au were used as the Schottky and ohmic contacts in the case of n-type GaN while Ni/Au and Ti/Au were used in the p-type case. For more

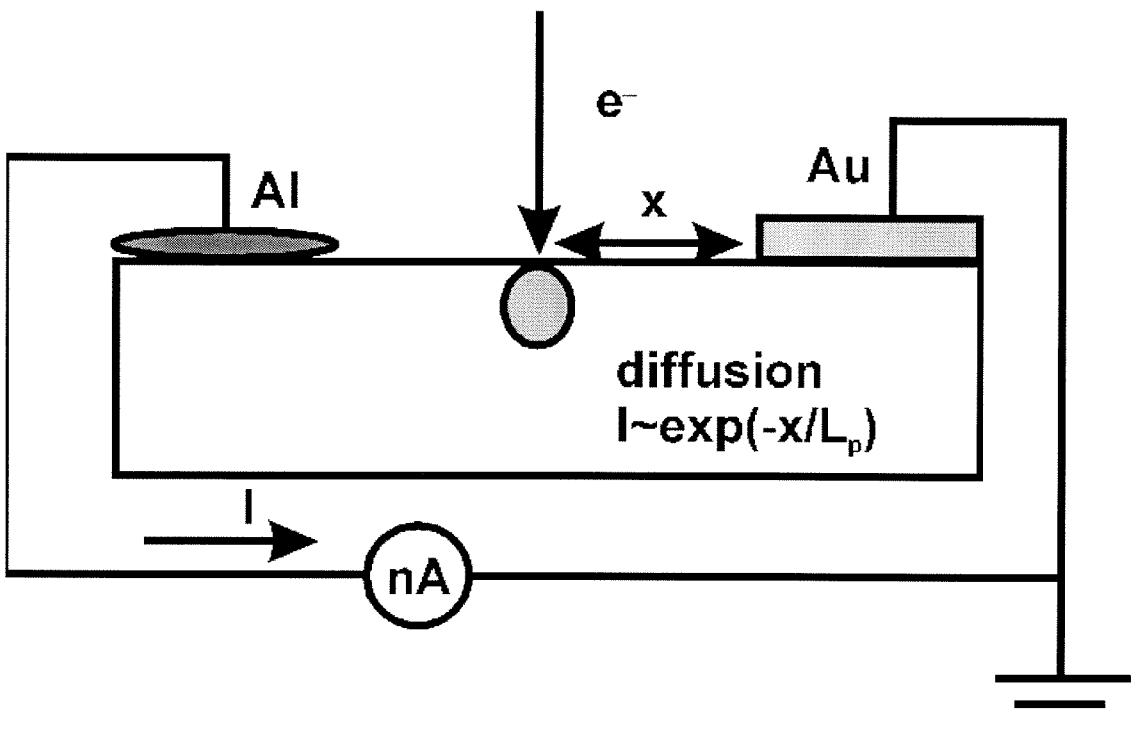

Figure 5.1: A schematic of the EBIC measurement conducted in the SEM. Al and Au represent the ohmic and Schottky contacts to the GaN film for the diode required to perform the EBIC measurement. Minority carriers generated by the high energy electron beam diffuse to the Schottky contact where they are collected and form the current measured by the amplifier.

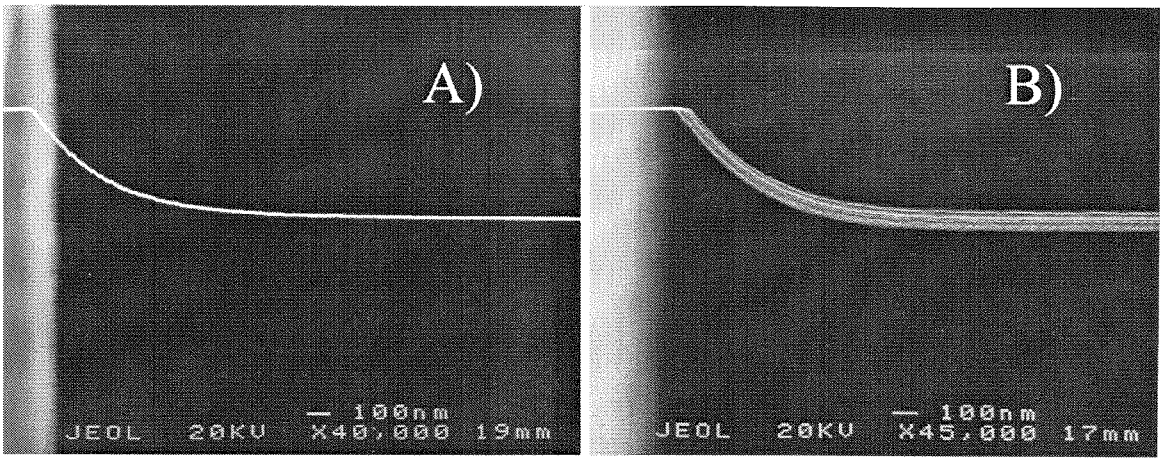

Figure 5.2: Line Scan profiles of the EBIC superimposed on the secondary electron image of the Schottky contact. A) P-type MOCVD grown GaN. The beam current was 0.5nA at an accelerating voltage of 20kV. B) N-type MOCVD grown GaN. The beam current was 1.06nA at an accelerating voltage of 20kV. The profile of the EBIC as a function of distance from the edge of the Schottky contact is fitted to the theoretical relation $I = kx^{-1/2}exp(-x/L)$ in order to determine the diffusion length.

detailed discussions of EBIC measurements see References [6] [11] and in general Reference [13]. A sample of the EBIC data is shown in Figure 5.2. The profile of the EBIC as a function of distance from the edge of the Schottky contact is fitted to the theoretical relation $I = kx^{-1/2}exp(-x/L)$ to determine the diffusion length.

5.2.2 GaN Samples

The n-type MOCVD films for this study were commercially grown, unintentionally doped 2μm thick GaN on sapphire with a carrier concentration in the 10^{17}cm^{-3} range. The p-type MOCVD films were commercially grown, Mg doped 2μm thick GaN on sapphire with a carrier concentration in the 10^{17}cm^{-3} range. The HVPE sample was a commercially grown, 10μm thick GaN layer on sapphire. The 10μm layer consisted of a 8μm thick low conductivity ($\approx 10^{16}$cm^{-3}) layer and a highly conductive bottom layer.

The molecular beam epitaxy (MBE) samples were grown by E. C. Piquette in our MBE facility. Ga-polar samples were grown on sapphire using a thin AlN buffer layer and an RF plasma source for active nitrogen. The film was grown at 800C, near

stoichiometric conditions, to a thickness of 820 nm. Layer thickness were confirmed by variable angle spectroscopic ellipsometry (VASE). The surface of the film shows hillocks which may be a result of gallium flux deficiency during growth or the presence of inversion domains due to the growth on bare sapphire.

5.3 Results

Figure 5.3 shows representative results for n-type MOCVD GaN. The small pits observed are 30 nm in size as was the case in Reference [10]. Although the two images are different (in one case the defects appear to lie along the grain boundaries and in the other terminating steps), the "defect free" regions are typically on the order of 0.5 μm which also appears to be the case in Reference [10]. Grains of similar size have also been observed by scanning capacitance microscopy [14]. The corresponding thresholded images are shown to accentuate the distribution of surface defects. The average measured hole diffusion lengths for both samples were the same to within experimental error; $L_p = 0.28 \pm 0.02\mu$m.

Figure 5.4 shows results for p-type MOCVD and n-type MBE grown GaN which also exhibited surface terminated defects. In the p-type sample (left) long trains of defects clearly outlined the grain boundaries which were in the same size range as the n-type material, 0.5μm. Electron diffusion lengths in this p-type sample were measured to be $L_e = 0.2 \pm 0.05\mu$m. The MBE film (right) clearly shows pyramidal hillocks associated with inversion domains that thread the GaN film [15]. The flat regions between the hillocks are roughly 0.25μm in size and the hole diffusion length for this material was $L_p = 0.22 \pm 0.03\mu$m. Figure 5.5 shows the n-type HVPE sample at a boundary between regions of flat and spiral growth. Very small surface pits are visible at the step boundaries in the spiral region whereas larger pits of the same size as those in Figures 5.4 and 5.4 are visible in the flat region. A boundary between the two regions is shown in Figure 5.5. Preliminary measurements of the hole diffusion length in this sample gave regions of higher and lower L_p, which might correspond to the different growth regions which appear to have less and more surface defects as

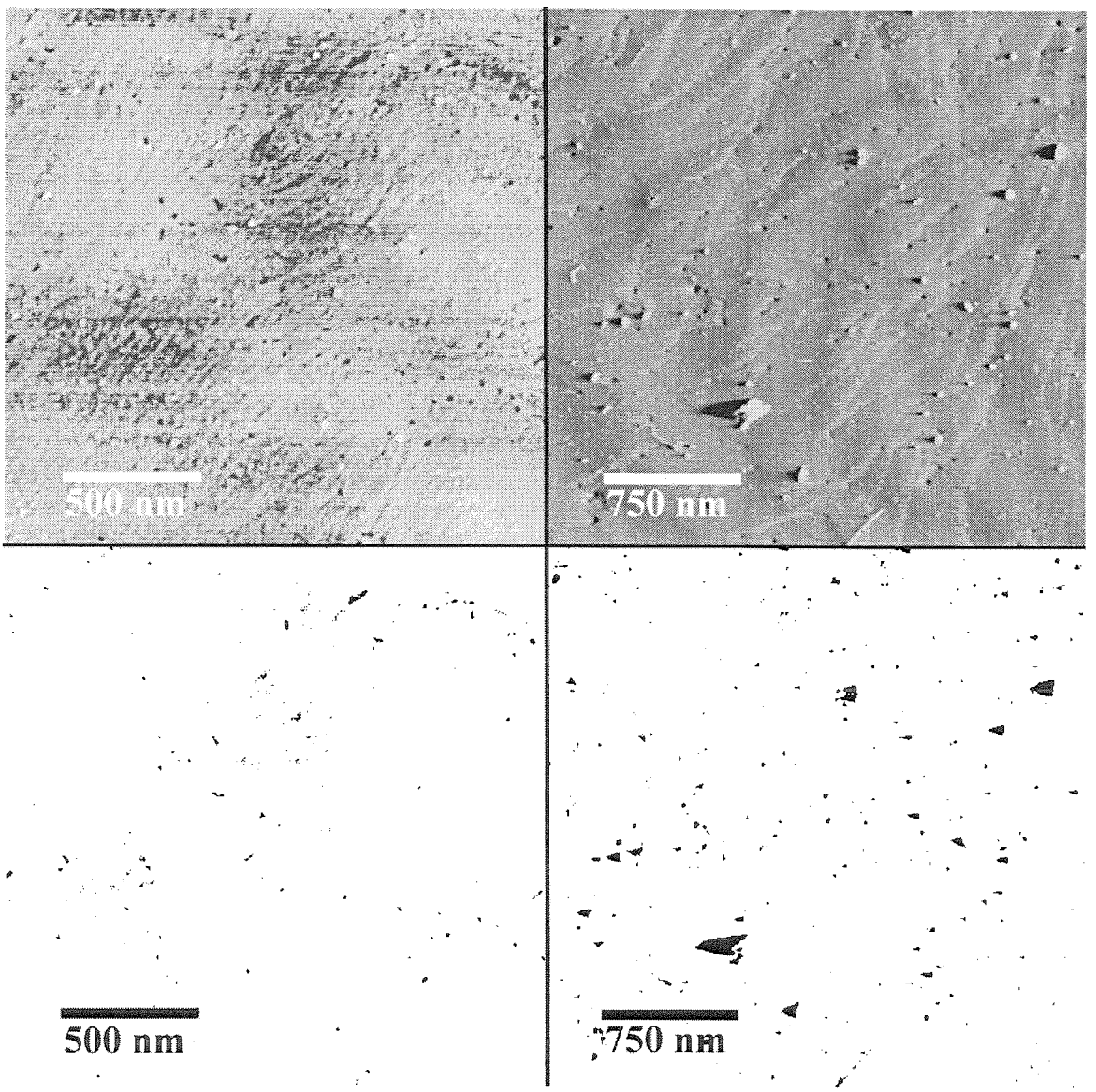

Figure 5.3: Two samples of n-type MOCVD Grown GaN. The top left image is a 3μm AFM scan and the top right image is a 2μm scan. Corresponding thresholded images are shown below to accentuate the defects which appear as 30nm dark areas. Their distribution does not appear to be random, but decorating the grain boundaries.

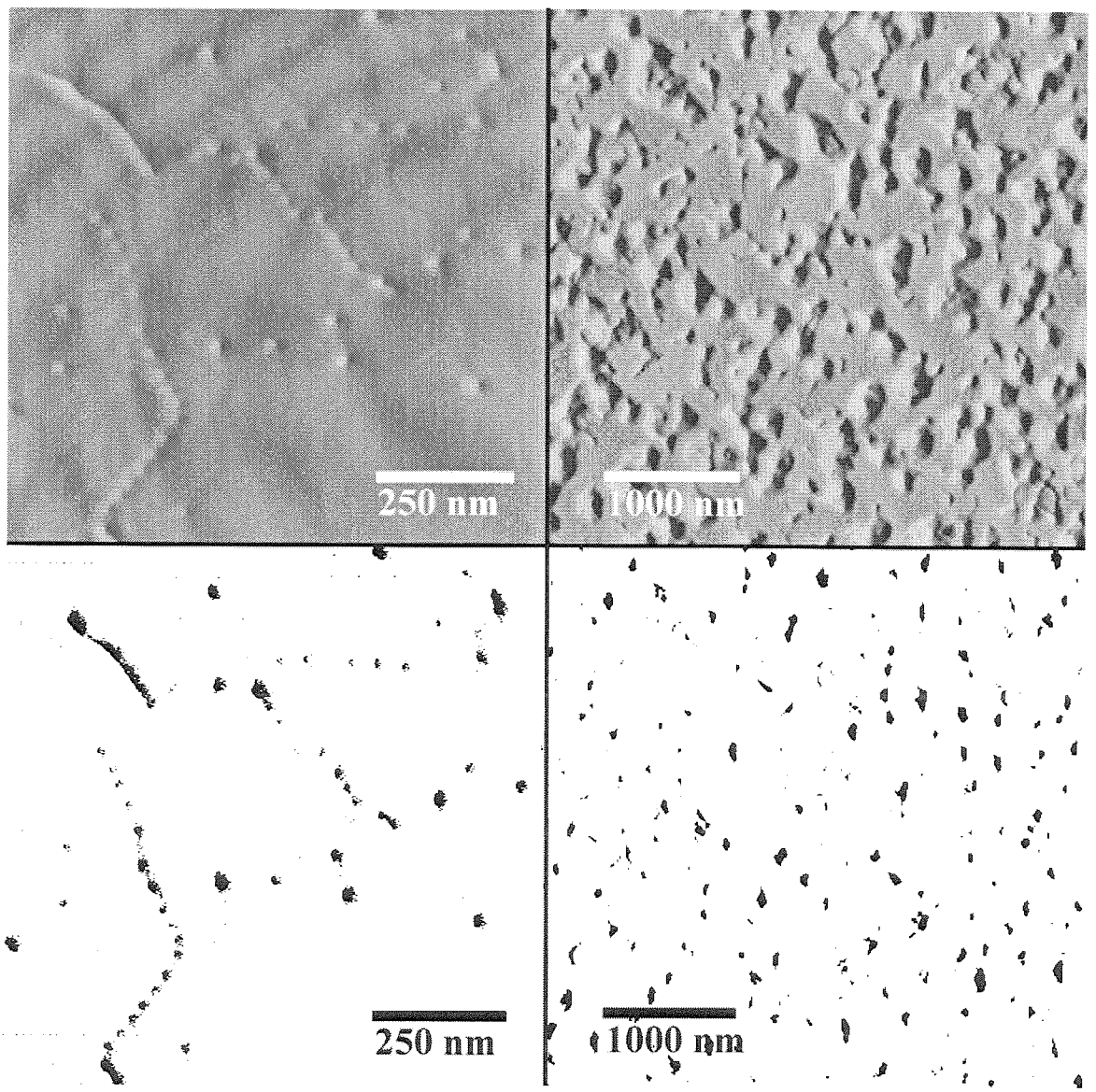

Figure 5.4: Left: 1μm AFM image of p-type MOCVD Grown GaN showing the pits on the surface from the termination of linear defects at the surface. Right: 4μm AFM image of n-type MBE grown 1μm thick GaN film on sapphire. The bottom left and right images are the thresholded data to accentuate the distribution of the defects.

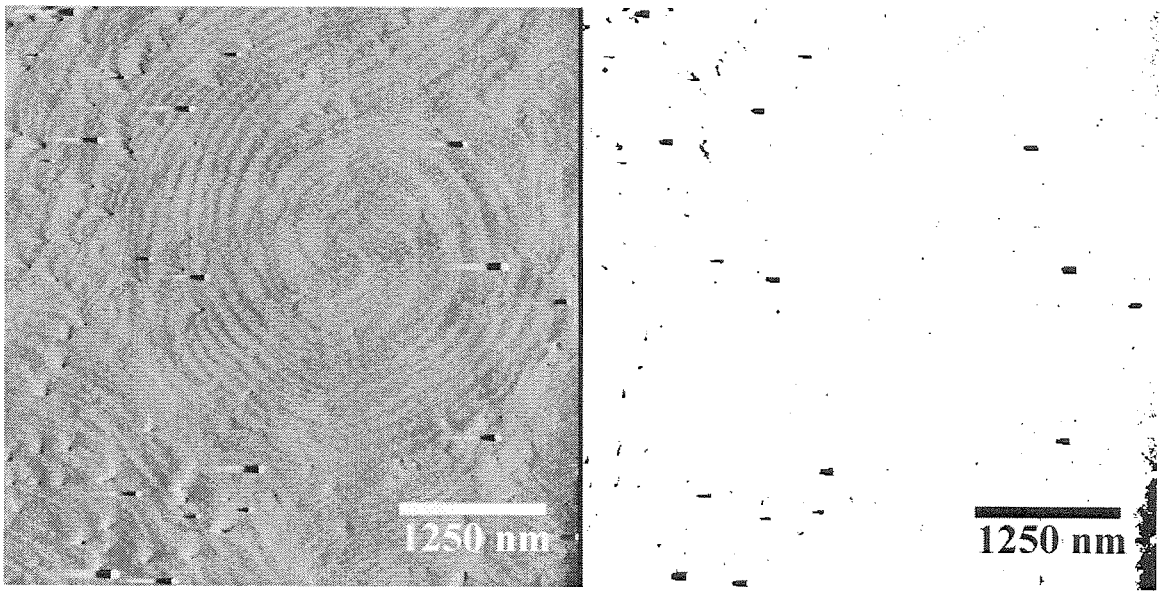

Figure 5.5: Left: 5μm AFM image of n-type HVPE grown GaN showing the boundary between the two distinct regions. Right: The corresponding thresholded image to accentuate the defects.

indicated by the right-hand image in Figure 5.5.

A summary of the EBIC results is shown in Table 5.3. We can notice that the minority carrier diffusion lengths are always smaller than either the average grain size or average column size delineated by inversion domains.

5.4 Models for the diffusion length and lifetime

A simple model can be used to explain our observations. By solving the 1D diffusion equation for minority hole recombination on periodic grain boundaries (due to defects or inversion domains) in a manner similar to [16], we have

$$D\frac{d^2p}{dx^2} = \frac{\partial p}{\partial t} \tag{1}$$

with the periodic boundary condition $p(m * d) = 0$, where m is an integer and d is the distance between grain boundaries or columns separated by inversion domains. The boundary condition is set by the assumption that *all* the carriers recombine at

Sample	$CC[cm^{-3}]$	Diffusion length	$DD[cm^{-2}]$
n-MOCVD	10^{17}	$L_p = 0.28 \pm 0.02\mu$m	$(2-5)\cdot 10^9$
n-MBE	10^{16}	$L_p = 0.22 \pm 0.03\mu$m	10^9
n-HVPE	10^{16}	$L_p > 2\mu$m	10^8
p-MOCVD	10^{17}	$L_n = 0.20 \pm 0.05\mu$m	$5\cdot 10^9$

Table 5.1: Summary of the EBIC measurements on several GaN samples. The second column labeled with CC represents carrier concentration. The diffusion lengths in each row of the table are averages over a range of beam currents and different measurement positions on the sample. The last column labeled with DD gives density of linear dislocations for each sample.

the boundary. The separable solutions are of the form

$$p(x,t) = e^{\frac{-t}{\tau}} p(x) \tag{2}$$

where

$$p(x) = p_0 sin(\frac{n * x}{L_p}). \tag{5.1}$$

At the boundary, $p(md) = 0$ which gives $L_p = d/\pi$. Substituting measured values for $d = 0.5\mu$m, we find $L_p \approx 0.17\mu$m which is in good agreement with the measured values.

5.4.1 2D models for minority carrier diffusion length and lifetime: dislocation density or grain size

If minority carrier recombination on grain boundaries is the limiting mechanism for minority carrier transport, then a two-dimensional model should give a better representation of the observed grain structure. Similar models have been previously derived in case of GaP [20] and were derived for GaN by Z. Z. Bandić as given in the following section [21].

Random distribution of dislocations

If we assume that linear dislocations are distributed in a hexagonal "honeycomb-type" array, then the dislocation density can be expressed as $N_{dd} = 1/(\pi r_s^2)$, where $2r_s$ is the distance between two first-neighbor dislocations. Dislocations are assumed to have core diameter $2r_0$. The minority carrier concentration (holes, for example) is obtained by solving the two-dimensional diffusion equation for the minority carrier concentration p:

$$D_p \nabla^2 p = \partial p / \partial t. \tag{5.2}$$

Boundary conditions at the dislocations are given by:

$$(i) \quad p|_{r=r_0} = 0 \tag{5.3}$$

$$(ii) \quad \left.\frac{\partial p}{\partial r}\right|_{r=r_s} = 0. \tag{5.4}$$

Boundary condition (i) is for complete recombination at the dislocation. Therefore, the minority carrier concentration must be zero. Condition (ii) is approximation to the periodic boundary condition. [20] After solving Eq. 5.2 in cylindrical geometry, the minority carrier lifetime τ_{scat} is obtained: [20]

$$\tau_{scat} = \frac{1}{2\pi D_p N_{dd}} \left(ln \frac{2}{r_0 \sqrt{\pi N_{dd}}} - 0.57 \right) \tag{5.5}$$

If the intrinsic minority carrier lifetime without scattering at dislocations is given by τ_0, then the total minority carrier lifetime becomes $\tau_p^{-1} = \tau_0^{-1} + \tau_{scat}^{-1}$. The hole lifetime and corresponding diffusion length obtained from the model are shown in Figure 5.6 as a function of dislocation density. For the calculation shown in Figure 5.6, we used the measured value for hole diffusivity, $D_p = 0.12\,\mathrm{cm}^2/\mathrm{s}$, obtained from MOCVD samples, and dislocation core radius of $r_0 = 30$ nm, which is typically observed by AFM measurements.

Dislocations occupying grain boundaries

In the majority of samples, experimental observation of the linear dislocation patterns show that they are distributed at the boundaries of otherwise defect-free grains. Random distribution does occur, but not in the majority of cases.

The schematic of this type of distribution of linear dislocations is also shown in Figure 5.7. In this case, the boundary conditions for the diffusion equation become:

$$(i) \quad p|_{r=r_s} = 0 \tag{5.6}$$

$$(ii) \quad \frac{\partial p}{\partial r}\Big|_{r=0} = 0. \tag{5.7}$$

The solution for the minority carrier lifetime in this case is

$$\tau_{scat} = \frac{r_s^2}{D_p} \frac{1}{2.4^2}. \tag{5.8}$$

The hole lifetime and diffusion length obtained from Eq. 5.8 are shown in Figure 5.7, using $\tau_p^{-1} = \tau_0^{-1} + \tau_{scat}^{-1}$, where τ_0 is the intrinsic lifetime as before.

Both models, either in the case of uniform distribution of linear dislocations, or in the case of linear dislocations occupying boundaries of defect-free grains, predict that minority carrier lifetime and diffusion length should be grain size limited for grain sizes 1 μm or smaller or dislocation limited at dislocation densities of 10^9cm^{-2} and higher. This is in qualitative agreement with our experimental observations as indicated in Table 5.3.

5.5 Conclusions

We have studied linear dislocations and surface defects in p and n-type metal organic chemical vapor deposition(MOCVD), hydride vapor phase epitaxy (HVPE) and molecular beam epitaxy (MBE) grown GaN films on sapphire with atomic force microscopy. The surface pits due to threading dislocations were found not to be distributed randomly but on the boundaries of growth columns. The dislocations

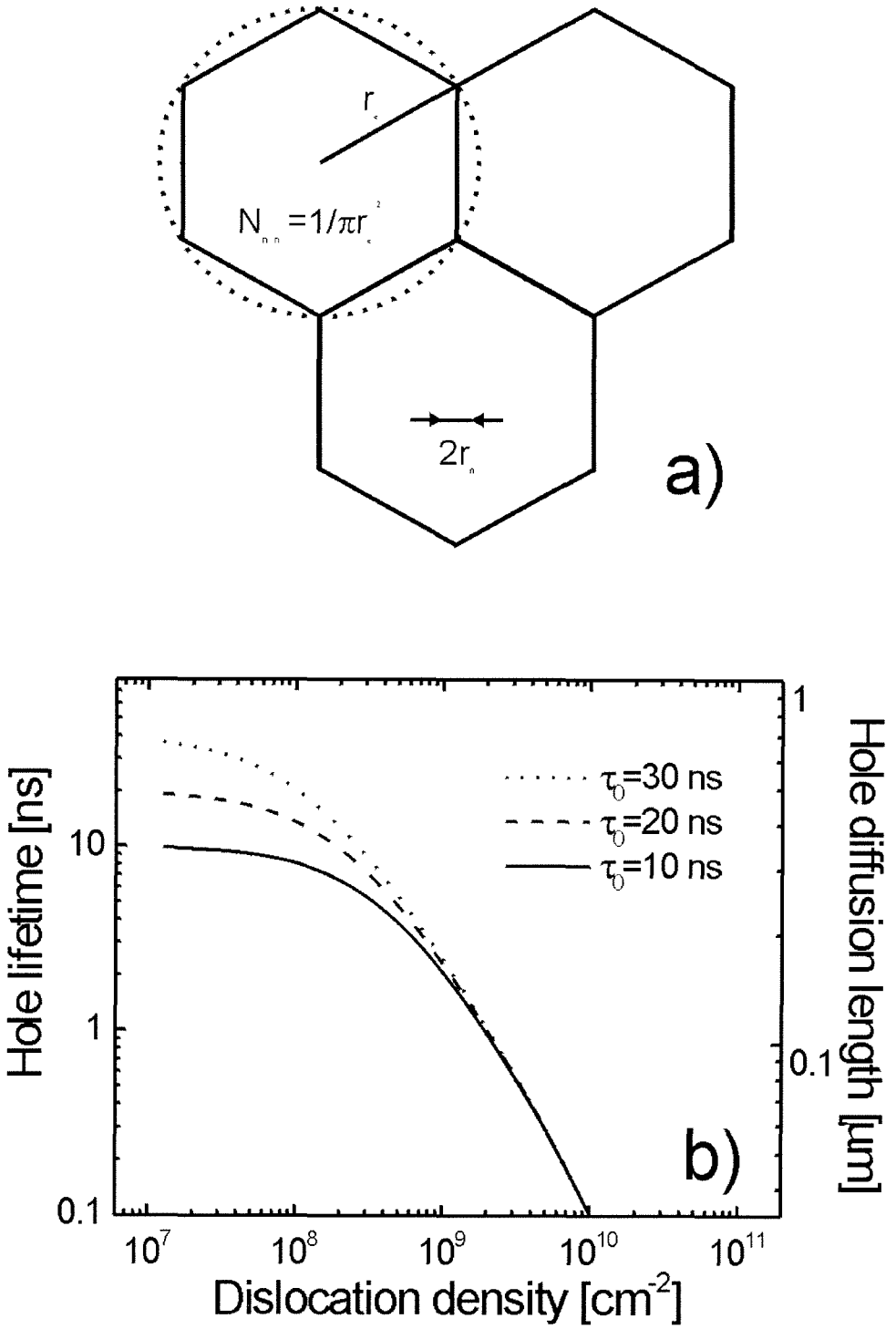

Figure 5.6: Hole lifetime and diffusion length as a function of dislocation density. a) Uniform array of linear dislocations. The dislocation core radius is r_0, and distance between dislocation is $2r_s$. b) Hole lifetime and diffusion length as a function of dislocation density, assuming uniform distribution of dislocations. The data is plotted using a diffusivity measured for MOCVD samples. The hole lifetime τ_0 without recombination at dislocations is used as an parameter in the plot.

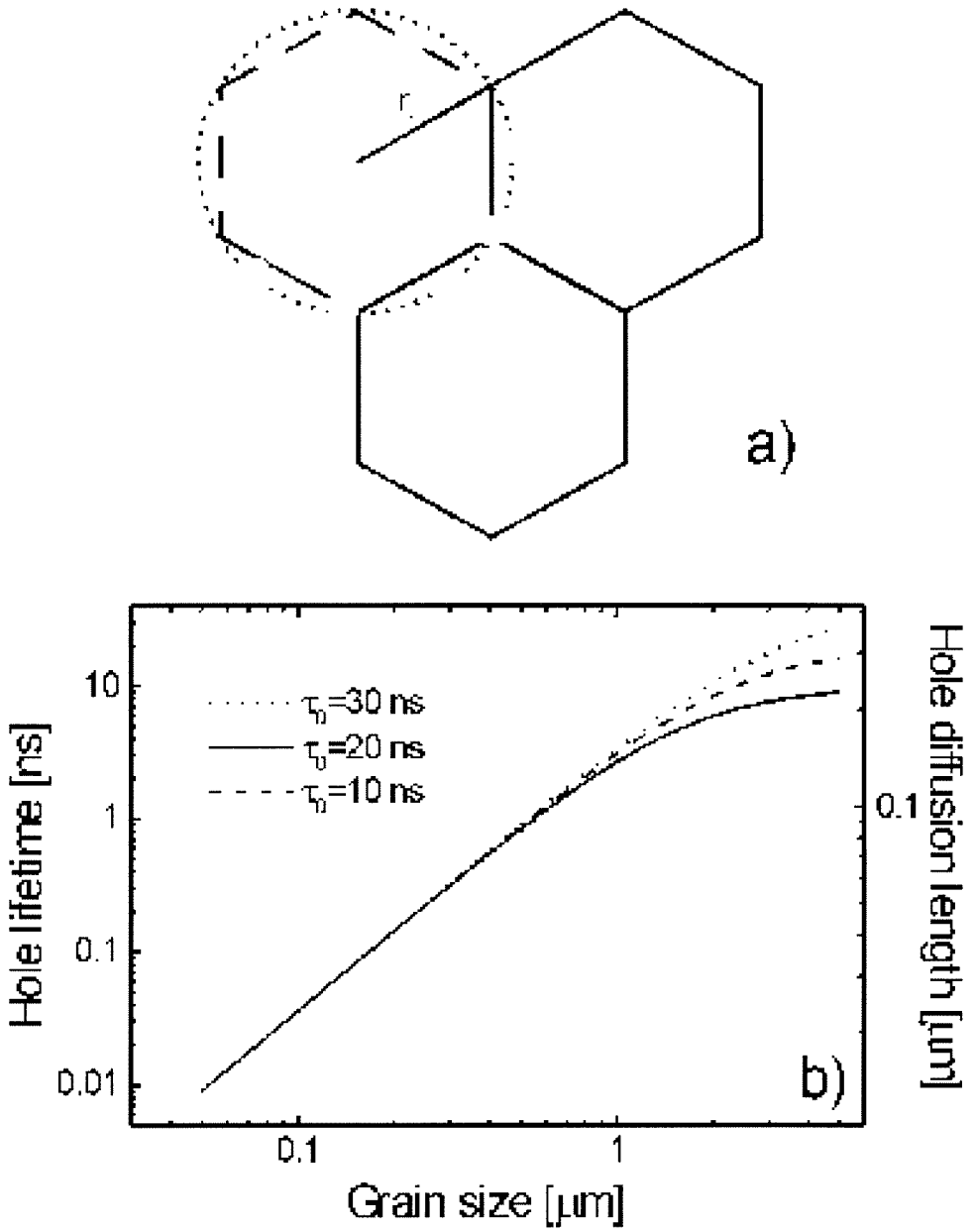

Figure 5.7: Hole lifetime and diffusion length as a function of average grain size. a) Dislocations occupying boundaries of otherwise defect-free grains. The radius of grains is r_s. b) Hole lifetime and diffusion length as a function of average grain size in the case of linear dislocations occupying grain boundaries of defect-free grains. The data is plotted using a diffusivity measured for MOCVD samples.

are thought to be electrically active since the average distance between them (average column size) is comparable to minority carrier diffusion lengths as measured by electron beam induced current experiments on Schottky diodes fabricated with the same material. Diffusion lengths found for holes and electrons were found to be $L_p = 0.28 \pm 0.03 \mu$m and $L_e = 0.2 \pm 0.05 \mu$m. This distance corresponds to the sizes of regions free from surface dislocations in both cases and can be described by a simple model of recombination on grain boundaries. A non-uniform distribution of defects would offer one explanation why, on the assumption that defects are involved in recombination, a high "average" dislocation density would not necessarily yield small diffusion lengths.

Bibliography

[1] S. Nakamura, M. Senoh, S. Nagahama, N. Iwasa, T. Yamada, T. Matsushita, Y. Sugimoto, and H. Kiyoku, *Appl. Phys. Lett.* **70**, 1417 (1997).

[2] M. A. Kahn and M. S. Shur, Mater. Sci. and Eng. B **46**, 69 (1997).

[3] J. M. Van Hove, R. Hickman, J. J. Klaassen, P. P. Chow, and P. P. Ruden, *Appl. Phys. Lett.* **70**, 2282 (1997).

[4] S. M. Mohammad and H. Morkoc, Prog. Quantum Electron. **20**, 361 (1996).

[5] Y. F. Wu, B. P. Keller, S. Keller, N. X. Nguyen, M. Le, C. Nguyen, T. J. Jenkins, L. T. Kehias, S. P. DenBaars, and U. K. Mishra, IEEE Electron. Device Lett. **18**, 438 (1997).

[6] Z. Z. Bandić, P. M. Bridger, E. C. Piquette, T. F. Kuech, and T. C. McGill, MRS Symposium Proceedings Vol. 483, 399 (1997).

[7] S. D. Lester, F. A. Ponce, M. G. Craford, and D. A. Steigerwald, *Appl. Phys. Lett.* **66**, 1249 (1995).

[8] L. Sugiura, *J. Appl. Phys.* **81** 1633 (1997).

[9] F. A. Ponce, MRS Bulletin, **22** No. 2, 51 (1997).

[10] S.J. Rosner, E. C. Carr, M. J. Ludowise, G. Girolami, and H. I. Erikson, *Appl. Phys. Lett.* **70**, 420 (1997).

[11] Z. Z. Bandić, P. M. Bridger, E. C. Piquette, and T. C. McGill, *Appl. Phys. Lett.* **72**, 3166 (1998).

[12] Z. Z. Bandić, P. M. Bridger, E. C. Piquette, and T. C. McGill, *Appl. Phys. Lett.* **73**, 3276 (1998).

[13] D. Chan, V. Ong, and J. Phang, IEEE Trans. on Elect. Devices **42** 5, 963 (1995).

[14] P. J. Hansen, Y. E. Strausser, A. N. Erickson, E. J Tarsa, P. Kozodoy, E. G. Brazel, J. P. Ibbetson, U. Mishra, V. Narayanamurti, S. P. DenBaars, and J. S. Speck, *Appl. Phys. Lett.* **72**, 2247 (1998).

[15] L. T. Romano and T. H. Myers, *Appl. Phys. Lett.* **71**, 3486 (1997).

[16] W. R. Harding, I. D. Blenkinsop, and D. R. Wright, Electron. Lett. **12**, 502 (1976).

[17] Z. Z. Bandić, P. M. Bridger, E. C. Piquette, R.A. Beach, V. M. Phanse, R. P. Vaudo, J. Redwing, and T. C. McGill, Presented at Materials Research Society Spring Meeting (1998).

[18] L. Chernyak, A. Osinsky, H. Temkin, J. W. Yang, Q. Chen, and M. A. Kahn, *Appl. Phys. Lett.* **69**, 2531 (1996).

[19] D. Kapolnek, X. H. Wu, B. Heying, S. Keller, U. K. Mishra, S. P. DenBaars, and J. S. Speck, *Appl. Phys. Lett.* **67**, 1541 (1995)

[20] W.R. Harding, I. D. Blenkinsop, and D.R. Wright, Electron. Lett. **12**, 502 (1976).

[21] Z. Z. Bandić, *Novel Devices Employing Epitaxial Wide Bandgap Semiconductors: Physics, Electronics and Materials Characterization* CIT Thesis 1999.

[22] B. Garni, J. Ma, N. Perkins, J. Liu, T. F. Kuech, and M. G. Lagally, *Appl. Phys. Lett.* **68**, 1380 (1996).

Chapter 6 Electric Force Microscopy of GaN

6.1 Introduction

Electric force microscopy (EFM) provides a sensitive way to measure electrostatic forces and potentials. In the past it has been used to measure buried surface topography, dielectric constants [1], deposit and image charge [2, 3], ferroelectric domain walls [4], and the potential across a pn junction. More recent applications include imaging and charging nanocrystals [5] as well as the modification of ferroelectric films.

In this chapter, we present several novel applications of EFM. In the first sections, we study molecular beam epitaxy (MBE) grown GaN films of both polarities using electric force microscopy to detect sub 1 micron regions of charge density variations associated with GaN extended defects. The large piezoelectric coefficients of GaN together with strain introduced by crystalline imperfections produce variations in piezoelectrically induced electric fields around these defects. The consequent spatial rearrangement of charges can be detected by electrostatic force microscopy and was found to be on the order of the characteristic Debye length for GaN at our dopant concentration. Additionally, the surface charge could be modified by externally applied strain and illumination. The electric force microscope signal was also found to be a linear function of the contact potential between the metal coating on the tip and GaN. Analysis of the data allowed us to measure both the surface state density and energy.

6.2 Theory of Electric Force Microscopy

Electric force microscopy can be performed in two ways: by detecting electrostatic forces and by detecting the surface potential. To detect the electrostatic forces, a voltage is applied to a conductive AFM tip (typically coated with metal) which is then scanned across the surface at a constant tip-sample separation. Phase differences induced by electrostatic forces on the oscillating tip during scanning are detected and give a qualitative measurement of the local charge density.

In order to find the force on the tip, we use a model like that for Kelvin force microscopy. The metal tip is modeled as a small capacitive element, in similar fashion to Ref. [6–8] only there is no external feedback loop to control the tip voltage. The energy of the tip is the sum of the Coulomb energy due to free charges and the energy in the small capacitor formed by the tip and the surface.

$$E = \frac{q_s q_t}{4\pi\epsilon_0 z} + \frac{1}{2}C(V_{applied} - V_{contact})^2 \tag{6.1}$$

where C is the sample-tip capacitance, q_s are surface charges, q_t are charges induced on the tip, and $V_{contact}$ is the contact potential between the tip metal and the surface material. The tip-sample separation, z, was set at either 30 nm or 50 nm for the experiments that will be discussed later. The force felt by the tip under an applied DC bias will be the derivative of the energy:

$$F = \frac{q_s q_t}{4\pi\epsilon_0 z^2} + \frac{1}{2}\frac{dC}{dz}(V_{applied} - V_{contact})^2 \tag{6.2}$$

Surface Potential

Local surface potential measurements are more complicated than either Kelvin force or electrostatic force microscopy. In short, to detect the local surface potential, an oscillating voltage plus a DC bias is applied directly to the AFM tip:

$$V_{applied} = V_{dc} + V_0 \cos(\omega t). \tag{6.3}$$

The tip then feels a force (at frequency ω) of

$$F = \frac{dC}{dz}(V_{dc} - V_{sample})V_0 \tag{6.4}$$

where $\frac{dC}{dz}$ is the vertical derivative of the tip-sample capacitance. To determine the surface potential of the sample, the tip voltage is adjusted by an additional feedback loop to equal the sample potential so that the tip feels no force. The essential difference between this technique and the one above is that at the zero force condition there is no tip motion and consequently no charge variation on the capacitor formed by the tip and the surface. As a result, the image is formed by the surface potential and not by the charge/contact potential.

For more detail, Appendix A derives the force on the tip from the Maxwell stress tensor.

6.3 Electric Force Microscopy of GaN

Nitride based devices have been of great interest in the last few years, notably due to their success in optoelectronics, where lasers and diodes have been demonstrated and successfully commercialized [9]. Further applications of nitrides are expected in the arena of high power, high power microwave and high temperature devices [10–12], as well as solar blind ultra-violet detectors [13]. It has been recently demonstrated that the large intrinsic piezoelectric coefficients of GaN and AlN are responsible for a high concentration two-dimensional electron gas at the AlGaN/GaN interface in heterojunction field effect transistors (HFET) [14, 15]. Other possibilities exist for the enhancement of electric properties of contacts to nitrides by piezoelectric engineering as recently demonstrated in the case of Schottky contacts [16]. While most of the recent research has emphasized electronic device aspects of the piezoelectric effect [14–16], comparatively little work has concentrated on the investigation of fundamental properties and nanoscale characterization of piezoelectrically induced phenomena. One consequence of the piezoelectric effect is that it allows electrostatic force imaging

of charge redistribution around defects due to local variations in strain caused by crystalline imperfections. Although the measurement of the magnitude of the charge density is non-quantitative, electric force microscopy (EFM) of charge density distributions can provide interesting insight into the nature of defects, the piezoelectric effect in nitrides, as well as Schottky barrier analysis and surface band bending. On the other hand, surface potentiometry can quantitatively map the change in surface potentials due to charge redistribution [1, 6].

6.3.1 GaN Growth

The gallium nitride layers studied here were grown by E. C. Piquette on c-plane sapphire substrates by radio frequency plasma assisted molecular beam epitaxy (MBE) in our MBE facility. Ga-polar GaN films were nucleated using AlN buffer layers whereas N-polar films were nucleated using a GaN buffer layer. Polarity was determined by RHEED reconstruction at low temperature [27], and by KOH etching [28, 29]. Other details of the growth conditions are presented in [24, 25]. Growth conditions for the Ga-face GaN were slightly Ga-rich, leading to locally flat (0001) Ga-face films which contain pits on the surface induced by dislocations or most likely $(000\bar{1})$ inversion domains threading along the growth direction. These pits are readily observed in atomic force microscopy (AFM) images [30] and are sites for the charge accumulation which will be imaged by the EFM.

6.3.2 Metal Deposition

A variety of different metals were used for coating the AFM tips to vary the metal work function for electric force microscopy and to provide the contact necessary for applying a bias to the tip. Cobalt coated AFM tips were obtained commercially from Digital Instruments. Titanium, Al, Pt, Pd, Ce, W, and Au coated tips were fabricated in the following manner. Commercial silicon tapping mode AFM tips were plasma cleaned in a 30W Ar plasma at a pressure of 8×10^{-4} Torr. A 15 nm metal layer was then sputter deposited in sputter chamber at a base pressure of 1×10^{-7}

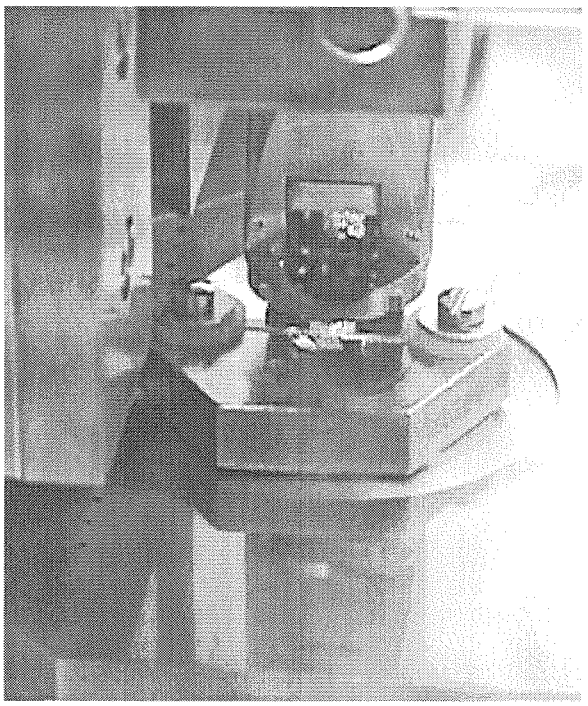

Figure 6.1: Photo of the Bioscope configured for surface charge studies of strained piezoelectric materials.

Torr. Electrical contact to the tip was made through the metallic clip on the AFM tip holder.

6.3.3 EFM Results: Contact Potential

All the EFM data presented here was collected using a Digital Instruments Nanoscope IIIa controller and a Bioscope scanning probe microscope operating in Tapping Mode. Although mechanically noisy, the Bioscope platform has many advantages for customization. For example, Figure 6.1 shows the Bioscope head with a custom stage for applying strain to the sample during imaging. Moreover access to the internal jumpers to apply external signals, independent grounds, etc., is simplified compared to the multimode microscope. This configuration gave us the unique capability for the strain and light enhancement experiments to be described later.

First, the electric field gradient was measured as a function of tip voltage to rule out topographical artifacts since they should not depend on the tip bias. Variation in the induced surface charges result in a force differential between the tip and the

surface that increases with tip voltage which can be observed in the series of EFM images in Figure 6.2. A complication here is that topography can affect the EFM image for films with a permanent polarization, $\mathbf{P}$, such as GaN. For such films, the surface charge, $\sigma_s = \mathbf{P} \cdot \hat{\mathbf{n}}$ where $\hat{\mathbf{n}}$ is the surface normal, will not be constant over a rough surface. Here, however, the topography is not severe enough to observe this effect since the induced pits are approximately 0.5 μm wide and only 25 nm deep giving a surface normal angle of only 3 degrees. Artifacts at high tip voltages due to capacitive effects are also problematic. To avoid them, it is necessary to keep the imaging voltages low which results in weak contrast. Despite these complicating factors, it is possible to obtain EFM images of the charge distributions.

It was found that the electrostatic force was a function of the magnitude of the tip voltage and not the sign, consistent with the theoretical V^2 dependence from Eq. 6.2. Another feature of Eq. 6.2 we can observe is a force minimum when the applied bias is equal to the contact potential between the GaN and the metallic tip. More specifically, $V_{contact} = \phi_m - \chi_{GaN} - \Delta E_{fn} - \Delta\phi$ is the contact potential between metallic tip and the semiconductor. In this formula, ϕ_m is metal work function, χ_{GaN} is the electron affinity of GaN (4.2 eV [31]), $\Delta\phi$ is band bending caused by surface states, and ΔE_{fn} is the Fermi level position in the GaN referenced to the bottom of the conduction band. This was experimentally observed, and Figure 6.2 illustrates this effect with a signal "null" at a tip voltage of 0.5 Volts in case of cobalt coated tips. The inset of Figure 6.3 is a plot of the signal RMS roughness (in arbitrary units) as a measure of contrast against the tip voltage to illustrate the minimum force condition. Typically, complete cancellation of the signal is not expected due to the first term in the Eq. 6.2 leaving some residual image due to electrostatic forces.

Figure 6.3 is a plot of the measured tip null voltage V_{null} as a function of the difference between metal work function and electron affinity of GaN. The observed dependence between V_{null} and $\phi_{metal} - \chi_{GaN}$ is indeed linear. Aluminum and cerium were found to be anomalous where the opposite sign of the voltage was required to null the EFM signal. This is attributed to different work functions of oxides which formed when the tips were exposed to air. A least squares linear fit of this experimentally

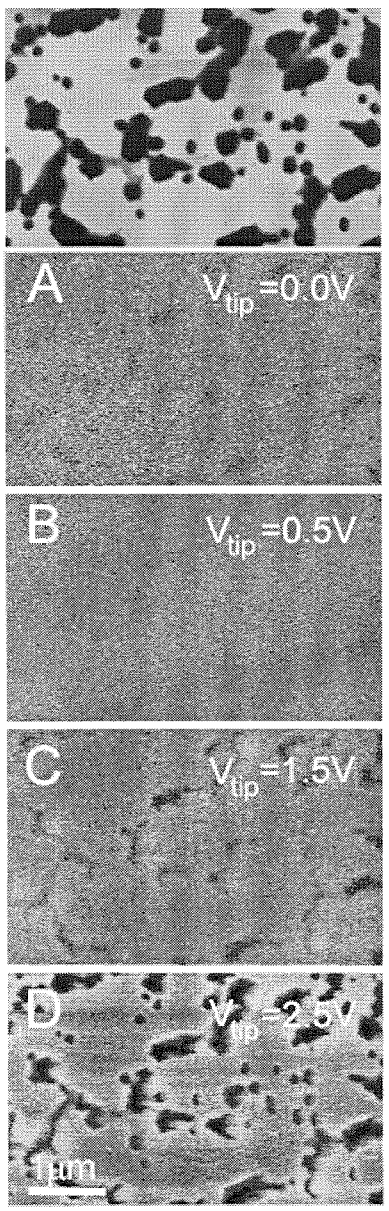

Figure 6.2: Electrostatic force image of the surface of MBE grown GaN as a function of tip applied voltage for a Ga-polar sample. For reference, the top image is the AFM scan of the same area imaged with EFM. Scans A-D are the EFM data with the tip bias increasing from A-D. Notice the signal "null" at a tip bias of 0.5 V. The tip sample separation was 50 nm in all the EFM images.

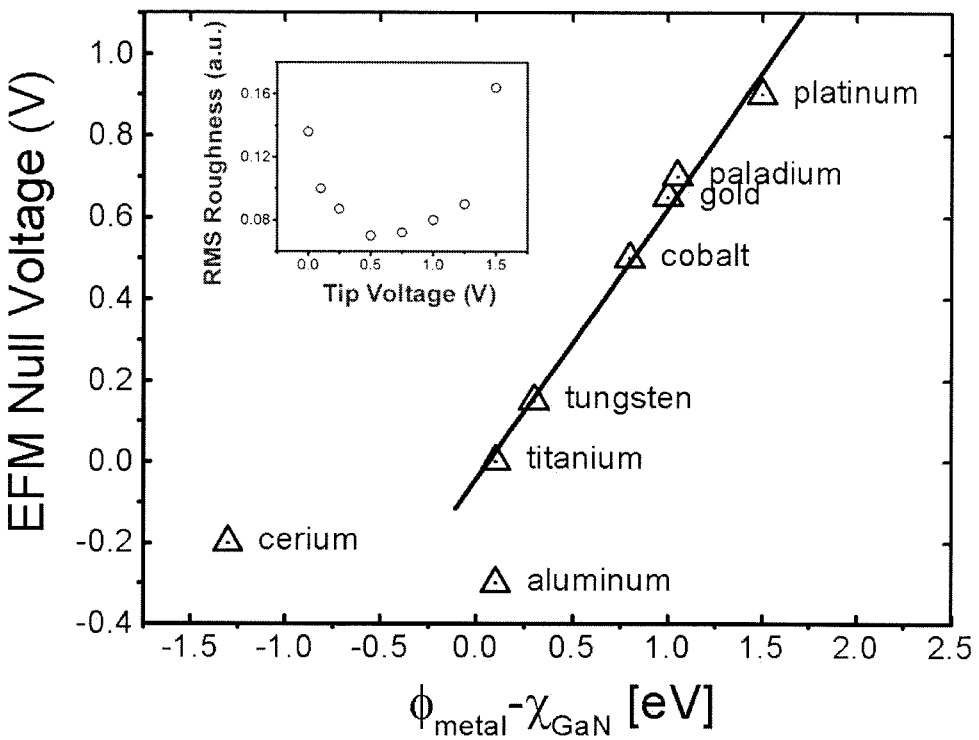

Figure 6.3: Plot of the tip voltage for a minimum force condition vs the work function difference between the tip metalization and GaN. Inset: Plot of the RMS contrast against the tip bias in arbitrary units illustrating the "null" condition for the cobalt coated tips.

observed dependence gives slope of 0.66 ± 0.03, and an intercept of -0.04 ± 0.03. A slope less than 1 and indicates presence of the surface states.

The situation will be considered as an electrostatic analysis of the following: 1) An ideal metal with work function ϕ_m. 2) A dielectric interface region with a thickness of the tip-sample separation. 3) A semiconductor surface with surface states that fill up to a particular energy. An analysis of the barrier energy as a function of the metal work function and semiconductor electron affinity [32] gives the following expression.

$$\phi_{Bn} = a(\phi_m - \chi) + (1 - a)\left(\frac{E_g}{q} - \phi_0\right) - \Delta\phi \tag{6.5}$$

Where ϕ_{Bn} is the barrier energy between a metal and an n-type semiconductor, ϕ_m

is the metal work function, χ is the electron affinity, E_g is the bandgap, $\Delta\phi$ is the barrier lowering, which is assumed constant, and ϕ_0 is the maximum energy of the surface states relative to the valence band. The quantity a arises from collecting terms while deriving Eq. 6.5 and is written as:

$$a = \frac{\epsilon_i}{D_s \delta q + \epsilon_i}. \tag{6.6}$$

D_s is the density of surface states, ϵ_i is the dielectric constant of the interface, and δ is the thickness of the metal-semiconductor interface. For the regression analysis we write $\phi_{Bn} = m(\phi_m - \chi) + b$ where m and b are determined by the slope and intercept. Regrouping terms in Eq. 6.5 $a = m$ is determined directly by the slope. The intercept, b, is written as

$$b = (1 - a)\left(\frac{E_g}{q} - \phi_0\right) - \Delta\phi. \tag{6.7}$$

The density and energy of the surface states can now be expressed in terms of the regression slope and intercept, m and b.

$$\phi_0 = \frac{E_g}{q} - \frac{b + \Delta\phi}{1 - m} \tag{6.8}$$

$$D_s = \frac{(1 - m)\epsilon_i}{m\delta q} \tag{6.9}$$

Substituting for the slope and intercept, the surface state energy, ϕ_0, lies 30 mV $\pm$ 90 mV above the valence band. This is consistent with an observation of surface states at or below the valence band maximum using x-ray photoemission spectroscopy [33, 34].

Using an air gap as the dielectric for the interface, the calculated density of surface states is $9.4 \pm 0.5 \times 10^{10}\text{cm}^{-2}$. If water, $\epsilon_i = 80\epsilon_0$, is used as the dielectric to try to account for a typical surface contaminant, the surface state density becomes $7.5 \pm 0.4 \times 10^{12}\text{cm}^{-2}$. Since the density of chargeable defects required to pin the Fermi level is on the order of 10^{14}cm^{-2} [35], we conclude that the GaN surface is unpinned in this case.

6.4 Surface Charge Distributions: Debye Length

Figure 6.4 shows that the nature of the charge rearrangement is due to screening of the piezoelectrically induced charges caused by strain relaxation at numerous defects. The N-polar (Figure 6.4 A and B) and Ga-polar (Figure 6.4 C and D) films have different defect structure and hence different surface morphology. Figure 6.4 A and B show EFM and AFM image and the associated profile for N-polar film. We can observe steps (approximately 5 nm in height) in the Figure 6.4 B, and associated charge accumulated on these steps (Figure 6.4 A). In case of Ga-polar films, charge accumulation (Figure 6.4C) is observed at the edges of the hexagonal pits. However, in both cases the strain relaxation and consequent charge rearrangement has a spatial extent of 60 nm. A calculation of the Debye length gives $L_D = \sqrt{\epsilon_s kT/q^2 N} \leq 100$ nm where both films have $N \geq 10^{15}$ cm^{-3}, ϵ_s is the dielectric constant of GaN, q is the elementary charge, and $T = 293$K. The 60 nm spatial extent of the measured charge is within the experimental error in the determination of the doping density. Therefore, since the spatial extent of the charge density surrounding the defects is approximately equal to the Debye length within experimental error, it is believed that the observed charge is a screening charge rather than the bare surface charge density that would be induced on the surface due to the termination of the polarization of the film. The Debye length observation is probably not precisely correct since a number of complicating factors exist. First, in the degree of screening at the surface both the bulk carrier density and the surface mobile carrier density will play a role; the second is quite difficult to determine, but probably plays a role since EFM is affected by above bandgap illumination which will be discussed in the next section. Also, the length scale over which stress relaxation occurs near a large topographic feature will determine the amount and spatial extent of piezoelectric charge density at the surface. For the future, a useful, and potentially important, calculation would be to estimate this and see how it compares with the calculated Debye lengths and observed contrast in EFM.

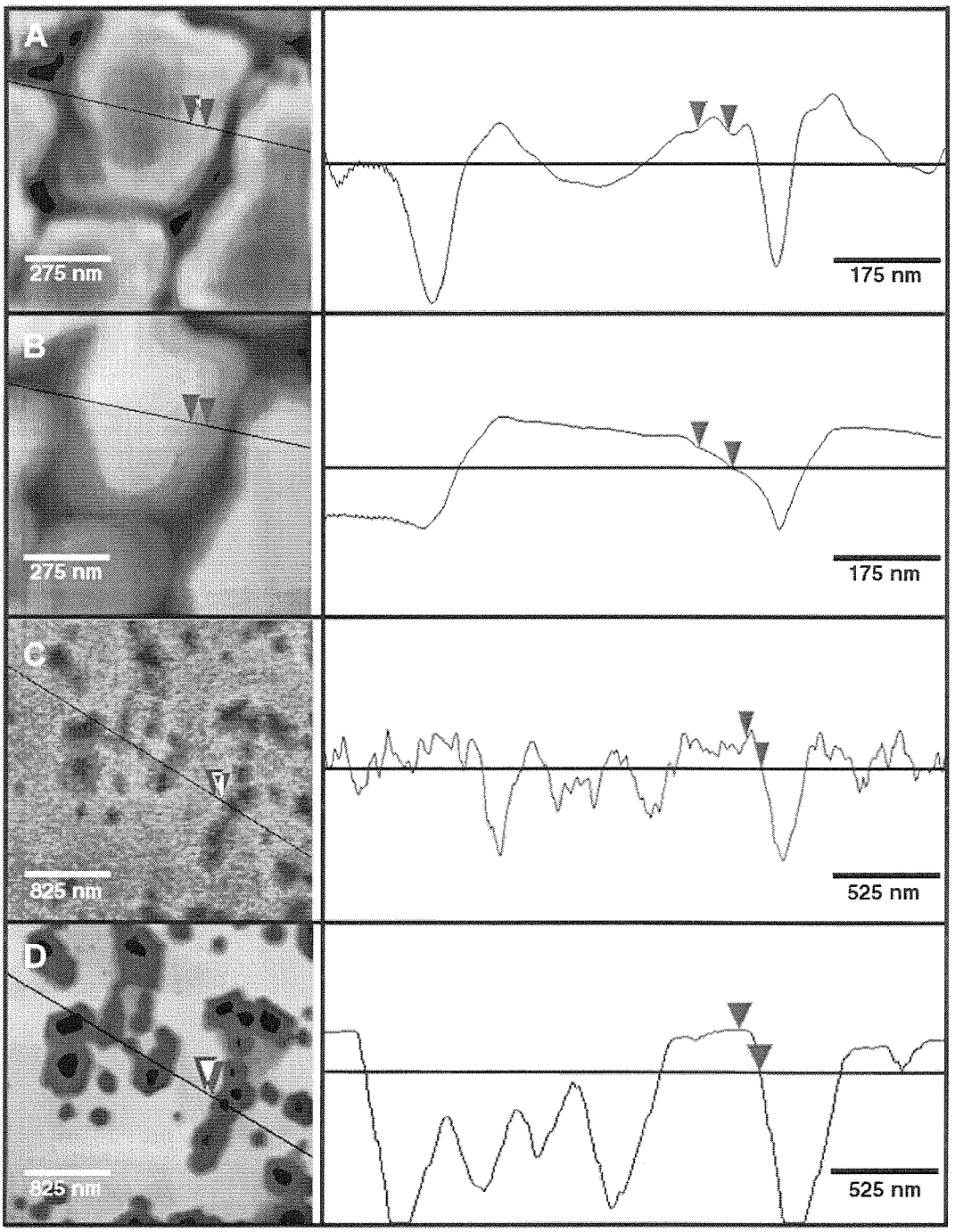

Figure 6.4: A. EFM image of the surface of N-polar GaN and its associated line profile. The arrows indicate the 60nm spatial extent of the screening charge associated with strain relaxation at the steps indicated in the following image. B. The AFM and associated line profile for the same area in A. Arrows indicate the steps of interest. C. EFM of Ga-polar GaN and its associated line profile. Again, arrows indicate the spatial extent of the screening charge associated with the defect structure indicated by the AFM image in D. In all cases the tip-sample separation was 30 nm.

6.4.1 Surface Charge Redistribution Due to Optical Generation and Strain

Light Enhancement Effect

The electric force was found to be light sensitive and was measured at several discrete wavelengths above and below the GaN bandgap energy (3.4 eV = 365 nm) using lasers at 635nm, 594.1nm, 543.5nm, and 325 nm as shown in Figure 6.5. The sample was illuminated at a small glancing angle to eliminate interference with the AFM as shown in Figure 6.6. The tip voltage was held constant at 5 mV, creating weak contrast in the EFM image without illumination as observed in Figure 6.2. The choice of tip bias was arbitrary since the experiment was conducted before we knew which tip voltages were likely to cause artifacts. When the sample was illuminated with a photon energy below bandgap (Figure 6.5(A-C)), no apparent difference in surface charge could be observed, even with optical powers above 1 mW. However, there is a significant increase in surface charge when the sample is exposed to light with a photon energy above the band gap (Figure 6.5 D). This increase is associated with the generation of electron-hole pairs, which cannot be obtained with photons of energy smaller than the GaN band gap. We speculate that the separation of generated charges by internal polarization fields, as well as the increase in the sample conductivity, are responsible for the observed change.

Figure 6.7 shows the EFM images obtained with tip voltage held constant at 5 mV, illuminated with the 325 nm laser, as a function of the optical power. The optical power required to produce a visible change in the EFM image was found to be as small as 1 μW. No change could be observed for the longer wavelengths even for optical powers up to three orders of magnitude greater.

Strain Effects

Since the piezoelectric effect will change the magnitude of the internal fields and consequently the surface charge distribution/potential, a home built stage was used to externally apply strain to GaN films by bending the sapphire substrate. The

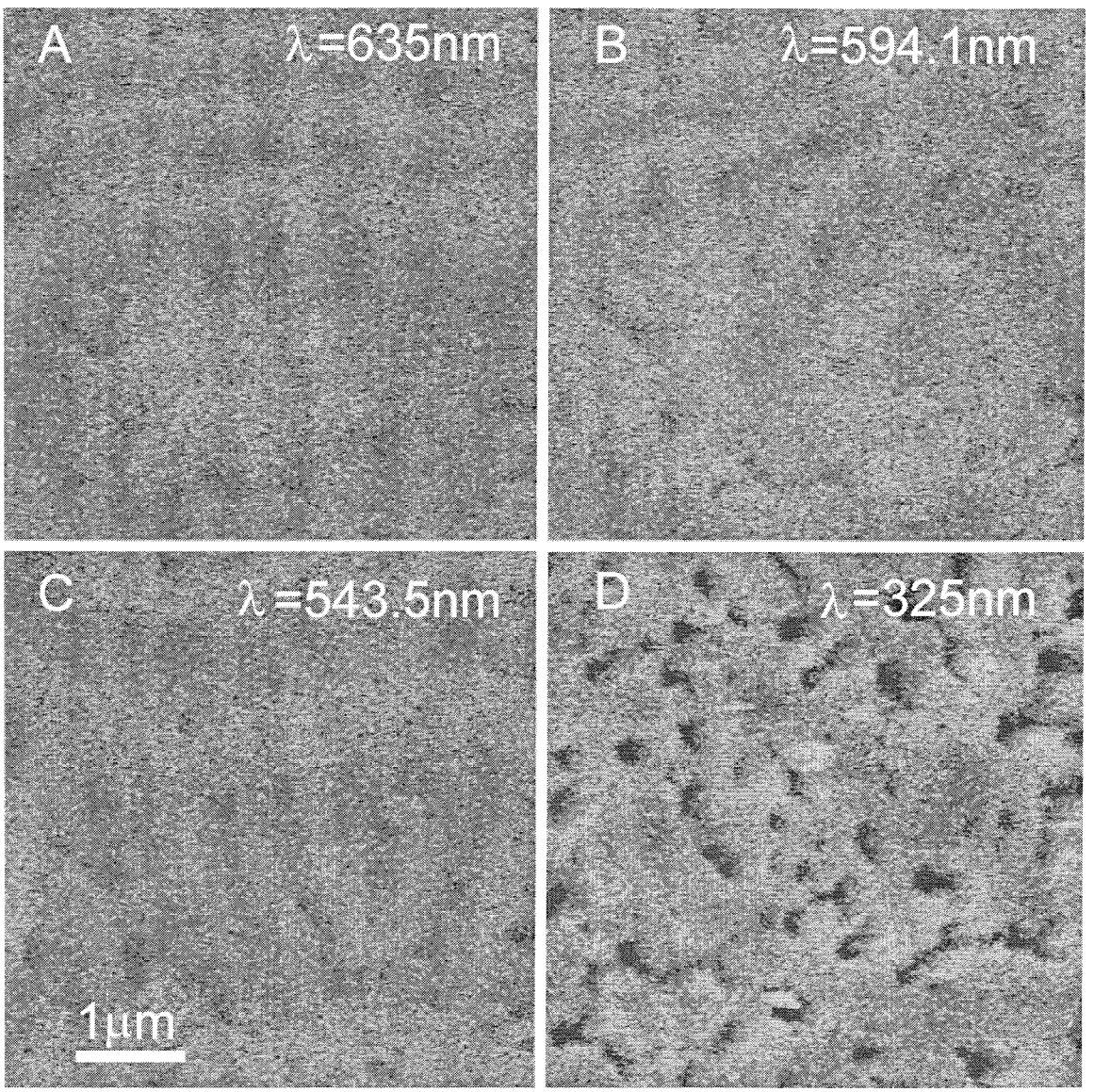

Figure 6.5: Electric field gradient (charge density) images at different illuminating wavelengths indicated in the upper right of each image. The tip bias was held at 5 mV with 50 nm tip-sample separation in all cases. A) 20 mW red diode laser. B) 1 mW Yellow HeNe laser. C) 1 mW Green HeNe laser. D) 10 μW from a UV HeCd laser.

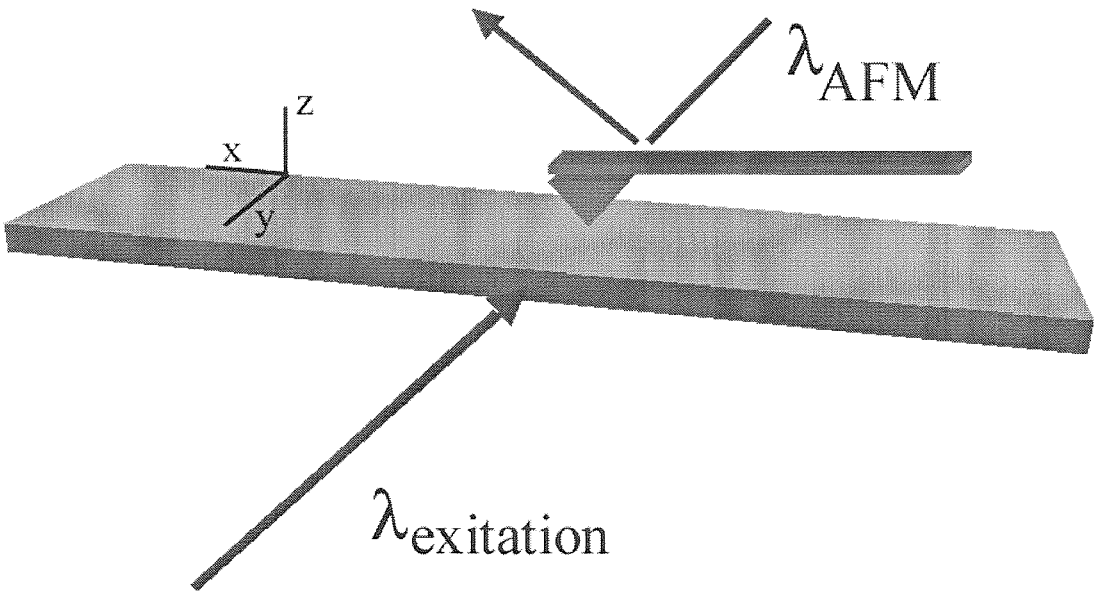

Figure 6.6: Illustration of the illumination geometry for the light enhancement effect. It is important to minimize the stray light from the external illumination. Light, other than from the AFM laser, that is collected by the AFM photodiodes affects the engage offset. Hence, as the intensity is changed during the experiment the AFM can lose the surface.

induced strain is tensile and approximately 1%. Subsequently, both electric field gradient and surface potential measurements were made on unstrained and strained samples and are shown in Figure 6.8. Contrast reversal is observed in the surface charge of the strained sample as shown in Figures 6.8A and B. Strained samples also showed regions which had changes in the surface potential of approximately 0.1V as indicated in Figures 6.8 C and D. One explanation of the observed light and strain effects is due to inversion domains as mentioned in Section 6.3.1. The spontaneous and strain-induced polarizations are anti-parallel to that of the bulk crystal within these inversion domains. Since polarization, which is perpendicular to the sample (0001) surface, induces free charge separation in such way to cancel the electric field, the domains of different orientation will induce different surface charges. This will create regions of opposite surface charge corresponding to inversion domain defect structure. In the light enhancement effect, opposite internal polarization fields separate the optically generated holes and electrons to create opposite contrast. The presence of inversion domains can also explain the observed contrast reversal. Since tensile strain

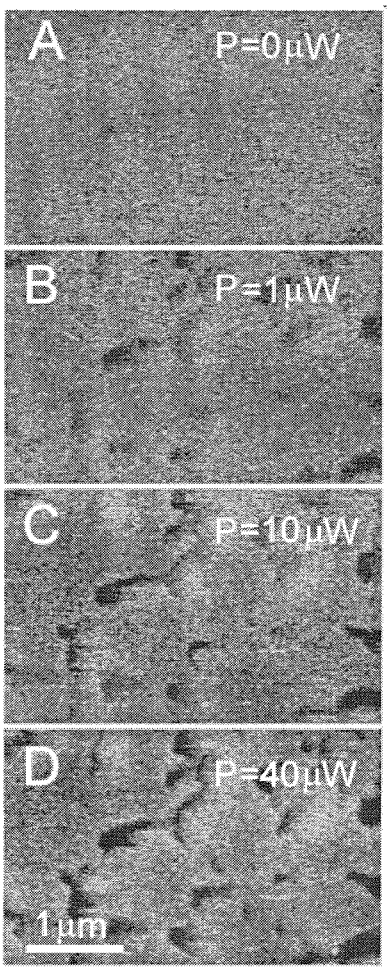

Figure 6.7: Electric field gradient (charge density) image as a function of optical power at 325 nm. Optical power increases from A-D. Tip Bias = 5 mV, and the tip-sample separation was 50 nm.

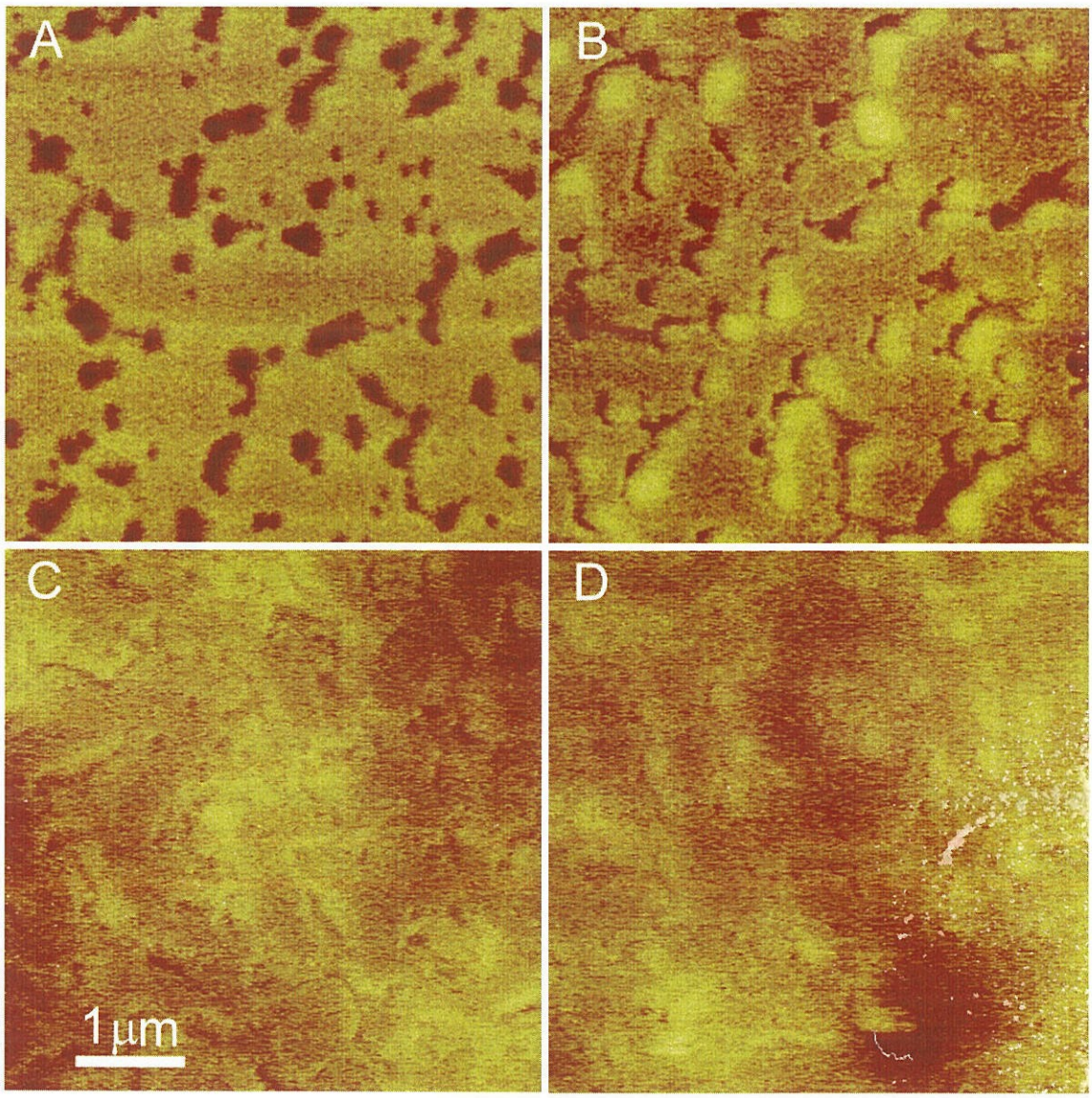

Figure 6.8: A) Electric field gradient (charge density) of an unstrained sample. B) Electric field gradient of a strained sample. In both cases, the tip voltage was held at 2.0V. C) Surface potential of an unstrained sample. D) Surface potential of a strained sample. In all cases the sample was unilluminated and the tip-sample separation was 50 nm.

will induce a piezoelectric polarization that adds to the spontaneous polarization, it is believed that the induced polarization charge is sufficient to overwhelm the available screening charge to reverse the sign of the surface charge. In subsequent experiments on N-polar films (which were not believed to have inversion domains) contrast reversal under strain was not observed. This supports the inversion domain argument; however, a direct observation of the inversion domains with TEM would be necessary for confirmation.

6.5 Summary

In summary, we have successfully demonstrated that EFM techniques can be used to detect local variations in piezoelectrically induced charge and potential on the sub 1 micron scale. These charges are believed to be screening charge on the surface since their spatial extent was comparable to the Debye length. We have also demonstrated that the EFM signal could be minimized by applying a voltage roughly equal to the contact potential between the tip metal and the GaN. An analysis of this contact potential variation gave a surface state density of $9.4 \pm 0.5 \times 10^{10} \mathrm{cm}^{-2}$ at an energy of 30 mV above the valence band. This technique also provides a method complementary to Kelvin probe microscopy for determining work function differences as well as a new way to determine surface state densities.

Bibliography

[1] Y. Martin, D. W. Abraham, and H. K. Wickramasinghe, *Appl. Phys. Lett.* **52**, 1103 (1988).

[2] D. M. Schaadt, E. T. Yu, S. Sankar, and A. E. Berkowitz, Appl. Phys. Lett. **74**, 472 (1999).

[3] J. E. Stern, B. D. Terris, H. J. Mamin, and D. Rugar, Appl. Phys. Lett. **53**, 2717 (1988).

[4] F. Saurenbach and B. D. Terris, *Appl. Phys. Lett.* **56**, 1703 (1990).

[5] R. M. Nyffenegger, R. M. Penner, and R. Schierle, Appl. Phys. Lett. **71**, 1878 (1997).

[6] Dror Sarid, *Scanning Force Microscopy*, Oxford University Press, New York, 1991.

[7] W. Nabhan, B. Equer, A. Broniatowski, and G. DeRosny, Rev. Sci. Inst. **68**, 3108 (1997).

[8] M. Nonnenmacher, M. P. O'Boyle, and H. K. Wickramasinghe, Appl. Phys. Lett. **58**, 2921 (1991).

[9] S. Nakamura, M. Senoh, S.Nagahama, N. Iwasa, T. Yamada, T. Matsushita, Y. Sugimoto and H. Kiyoku, Appl. Phys. Lett. **70**, 1417 (1997).

[10] M.A. Khan and M.S. Shur, Mater. Sci. and Eng. B **46**, 69 (1997).

[11] S.M. Mohammad and H. Morkoc, Prog. Quantum. Elecron. **20**,361 (1996).

[12] Z.Z. Bandić, E. C. Piquette, P. M. Bridger, R. A. Beach, T. F. Kuech, and T. C. McGill. Solid State Electronics **42**, 2289 (1998).

[13] J.M. Van Hove, R. Hickman, J.J. Klaassen, P.P. Chow, and P.P. Ruden, Appl. Phys. Lett. **70**, 2282 (1997).

[14] G. Zandler, J.A. Majewski, M. Stadele, P. Vogl, and F. Compagnone, Phys. Stat. Solidi B (**204**, 133 (1997).

[15] A. Bykhovski, B. Gelmont, and M. Shur, J. of Appl. Phys. **74**, 6734 (1993).

[16] E.T. Yu *et al.*, Appl. Phys. Lett. **71**, 2794 (1998).

[17] A. D. Bykhovski, V. V. Kaminski, M. S. Shur, Q. C. Chen, and M. A. Kahn, Appl. Phys. Lett. **69**, 3254 (1996).

[18] S. Muensit and I. L. Guy, Appl. Phys. Lett. **72**, 1896 (1998).

[19] X. C. Long, R. A. Myers, S. R. J. Brueck, R. Ramer, K. Zheng, and S. D. Hersee, *Appl. Phys. Lett.* **67**, 1349 (1995).

[20] R. D. Underwood, P. Kozodoy, S. Keller, S. P. DenBaars, and U. K. Mishra, *Appl. Phys. Lett.* **73**, 405 (1998).

[21] E.T. Yu et al., *Appl. Phys. Lett.* **73**, 1880 (1998).

[22] F. Bernardini, V. Fiorentini, and D. Vanderbilt, Phys. Rev. B **56** (16), 56 (1997).

[23] H. Yokoyama and T. Inoue, *Thin Solid Films*, 242, 33, (1994).

[24] E. C. Piquette, P. M. Bridger, Z. Z. Bandić, and T. C. McGill, presented at the 17th North American Conference on MBE, Penn State, 1998, talk G.1. Submitted to J. Vac. Sci. Technol. B.

[25] E. C. Piquette, P. M. Bridger, Z. Z. Bandić, and T. C. McGill, Mater. Res. Soc. Symp. Proc. 512, 387 (1998).

[26] Y. Leng, C. C. Williams, L. C. Su, and G. B. Stringfellow, Appl. Phys. Lett. **66**, 1264 (1995).

[27] A. R. Smith, R. M. Feenstra, D. W. Greve, M.-S. Shin, M. Skowronski, J. Neugebauer, and J. E. Northrup, Appl. Phys. Lett. **72**, 2114 (1998).

[28] M. Seelmann-Eggebert, J. L. Weyher, H. Obloh, H. Zimmermann, A. Rar, and S. Porowski. Appl. Phys. Lett. **71**, 2635 (1997).

[29] J. M. Van Hove, M. F. Rosamond, R. Hickman II, J. J. Klaassen, C. Polley, A. Wowchak, and P. P. Chow, presented at the 17th North American Conference on MBE, Penn State, 1998, talk G.3. Submitted to J. Vac. Sci. Technol. B.

[30] P. M. Bridger, Z. Z. Bandić, E. C. Piquette, and T. C. McGill, Appl. Phys. Lett., **73**, 3438 (1998).

[31] Q. Z. Liu and S. S. Lau, *Solid State Electronics* **42** (5), 677 (1998).

[32] S. M. Sze. *Physics of Semiconductor Devices* Wiley, New York, NY, 1981.

[33] K. E. Smith, S. S. Dhesi, C. B. Stagarescu, J. Downes, D. Doppalapudi, and T. D. Moustakas, Mat. Res. Soc. Symp. Proc. Vol. 482, 787, 1998.

[34] K. E. Smith, S. S. Dhesi, L. C. Duda, C. B. Stagarescu, J. H. Guo, J. Nordgren, R. Singh, and T. D. Moustakas, Mat. Res. Soc. Symp. Proc. Vol. 449, 787, 1998.

[35] A. Zur, T. C. McGill, and D. L. Smith, Phys. Rev. B **28** (4), 2060 (1983).

[36] S. Wang, *Fundamentals of Semiconductor Theory and Device Physics*, Prentice-Hall Englewood Cliffs, NJ, 1989.

[37] M. W. Wang, J. O. McCaldin, J. F. Swenberg, and T. C. McGill, Appl. Phys. Lett. **66**, 1974 (1995).

Chapter 7 Directed Charge Storage in Double Barrier CeO_2/Si/CeO_2/Si Structures Using Electric Force Microscopy

7.1 Introduction

In this chapter, an electric force microscope was used to induce and image localized dots of charge in a double barrier CeO_2/Si/CeO_2/Si(111) structure. By applying large charging voltages and reducing the tip to sample separation to 3-5 nm, dots 50-200 nm in radius of both positive and negative charge have been written. These charge dots are shown to be stable over periods of time greater than a day, with a very slow spreading and decrease in total stored charge. It is shown that the dots may be rewritten and replaced by charge of the opposite sign by application of the opposite charging voltage. The dependence of dot size on various writing parameters such as tip voltage, tip to sample separation, and write time is examined.

7.1.1 Cerium Oxide Background

Cerium oxide (CeO_2) is an insulating material with a lattice mismatch of only 0.35% to silicon (Si) and has an energy bandgap of $\sim$ 5.5 eV, an attractive set of properties with the potential to lead to a fully functional silicon heterojunction technology. A significant amount of work has been done examining the growth and characterization of CeO_2 crystals on Si [1–5], and the growth of single crystal Si on to CeO_2/Si heterostuctures has been recently reported [6]. Based on these promising results, a silicon resonant tunneling diode, an improved silicon-on-insulator (SOI) technology,

and stacked silicon electronics have all been proposed. A valuable and interesting addition to this array of technologies would be the capacity for electrostatic data storage.

Superparamagnetism

It will be useful to compare the current state of the art density (bit sizes) for magnetic recording to any proposed data storage scheme. While there are important benchmarks for recording technology such as signal to noise and data rates, limitations on the bit size will determine the ultimate areal density. Magnetism has its own, thermodynamically defined, size limit which cannot be subverted to achieve smaller bit sizes. At very small particle sizes, thermal energy is sufficient to switch the magnetization. For example, if an ensemble of particles is magnetized by the application of a field which is then removed, the magnetization decays as [7]:

$$M(t) = M(0)exp\left(\frac{-t}{\tau}\right) \tag{7.1}$$

The relaxation time τ is given by

$$\tau = 10^{-9}exp\left(\frac{0.5M_sH_cv}{kT}\right). \tag{7.2}$$

When the particle's energy $0.5M_sH_cv$ is 50 times the thermal energy, the relaxation time is 100 s. Since the relaxation time is *exponential*, it changes very quickly with particle volume, v. Practically, this occurs at particle sizes around 100 nm. The data storage market may very well push beyond this limit in its development of magnetic materials. Nevertheless, a realistic upper limit for bit densities in magentic media is (optimistically) believed to be around 100 Gb/in^2 or bit sizes around 80 nm. 80 nm will be the size benchmark for our charge dots.

7.1.2 Charge Deposition Experiment

Growth of CeO_2/Si Structures

Samples were produced by J. T. Jones from commercially available 3" Si(111) wafers, n-type with 3.0-4.3 Ω-cm resisitivity. After being subjected to a standard acetone, isopropyl alcohol, de-ionized water degrease in ultrasound, the wafers were etched in 50:1 HF solution until hydrophobic, rinsed in de-ionized water, and immediately introduced into vacuum. Prior to growth, samples were introduced to the chamber from the load lock and the chamber background pressure was brought to less than 5×10^{-10} Torr. Two manually shuttered electron beam evaporators were used to deposit material from an undoped Si charge and a 99.99% CeO_2 charge to grow the structures. A reflection high energy electron diffraction (RHEED) setup allowed for *in situ* film surface characterization during growth. Initially, a Si buffer layer was grown by depositing 0.3 Å/s Si at 850 °C for 60 seconds, and then depositing a 200 Å Si film at 550 °C. Buffer layer RHEED patterns were examined to assure the characteristic (7×7) reconstruction was apparent, indicative of a clean Si surface ready for further growth.

Cerium oxide thin films were grown at a wafer temperature of 550 °C, with chamber pressures ranging from $1 \times 10^{-7} - 2 \times 10^{-6}$ Torr due primarily to outgassing from cerium oxide pellets. Silicon thin films were also grown at a wafer temperature of 550 °C, with chamber pressures of $5 \times 10^{-8} - 2 \times 10^{-7}$ Torr. A double barrier structure CeO_2/Si/CeO_2/Si(111) was produced with symmetric CeO_2 barriers of 35 Å. The intermediate silicon film thickness was 25 Å for the sample and shown by RHEED to be polycrystalline.

7.1.3 Electric Force Microscopy: Charge deposition and Imaging

To place charge in the structures, the sample was placed in a conductive holder which used the AFM ground as a reference as shown in Figure 7.1. Depositing charge in

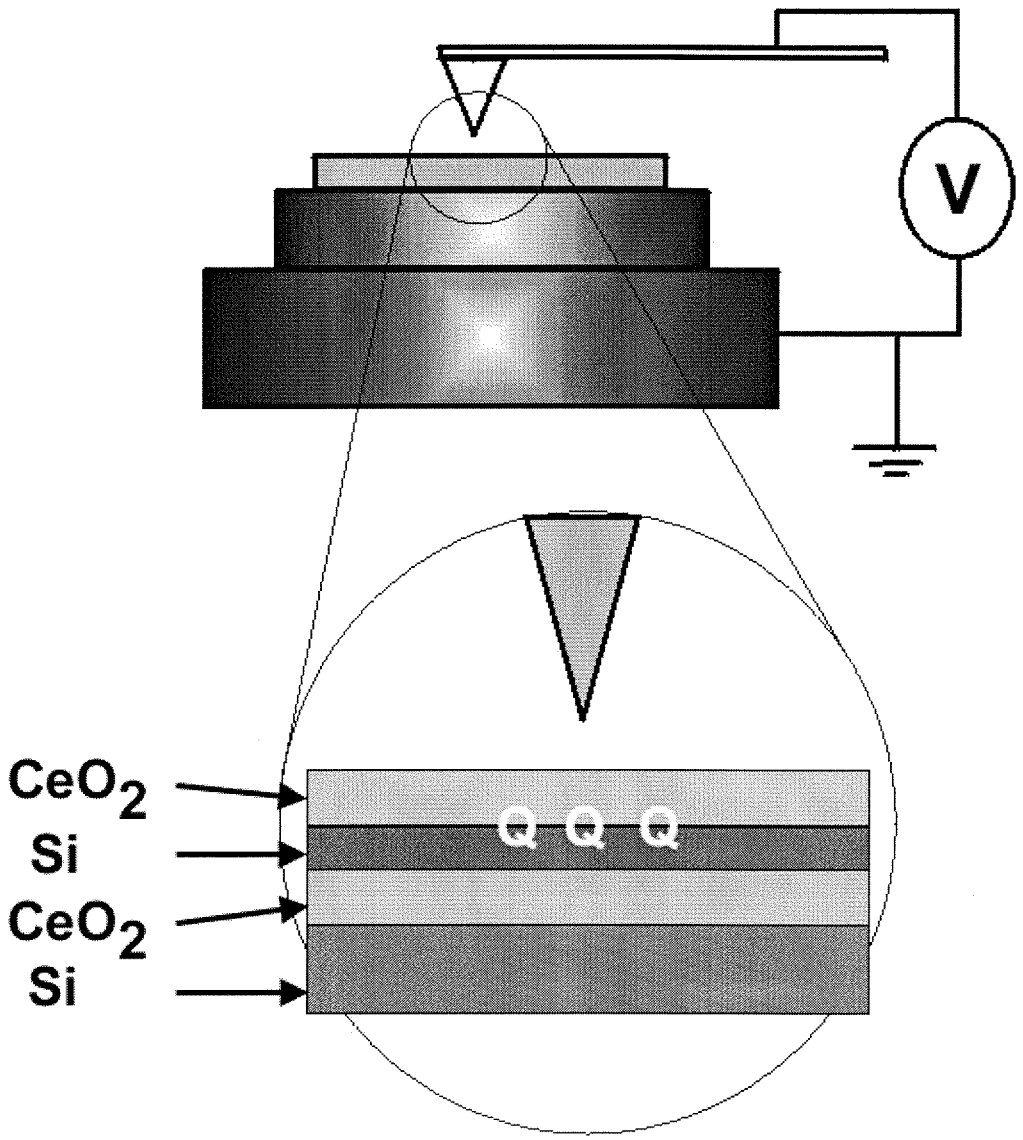

Figure 7.1: Electric force microscope configuration for depositing charge in the layers. The double barrier structures CeO_2/Si/CeO_2/Si(111) were produced with symmetric CeO_2 barriers of 35 Å. The intermediate silicon film thickness was 25 Å for each sample and shown by RHEED to be polycrystalline. Typical tip-sample separations were 3-5 nm during deposition and 20-30 nm during imaging.

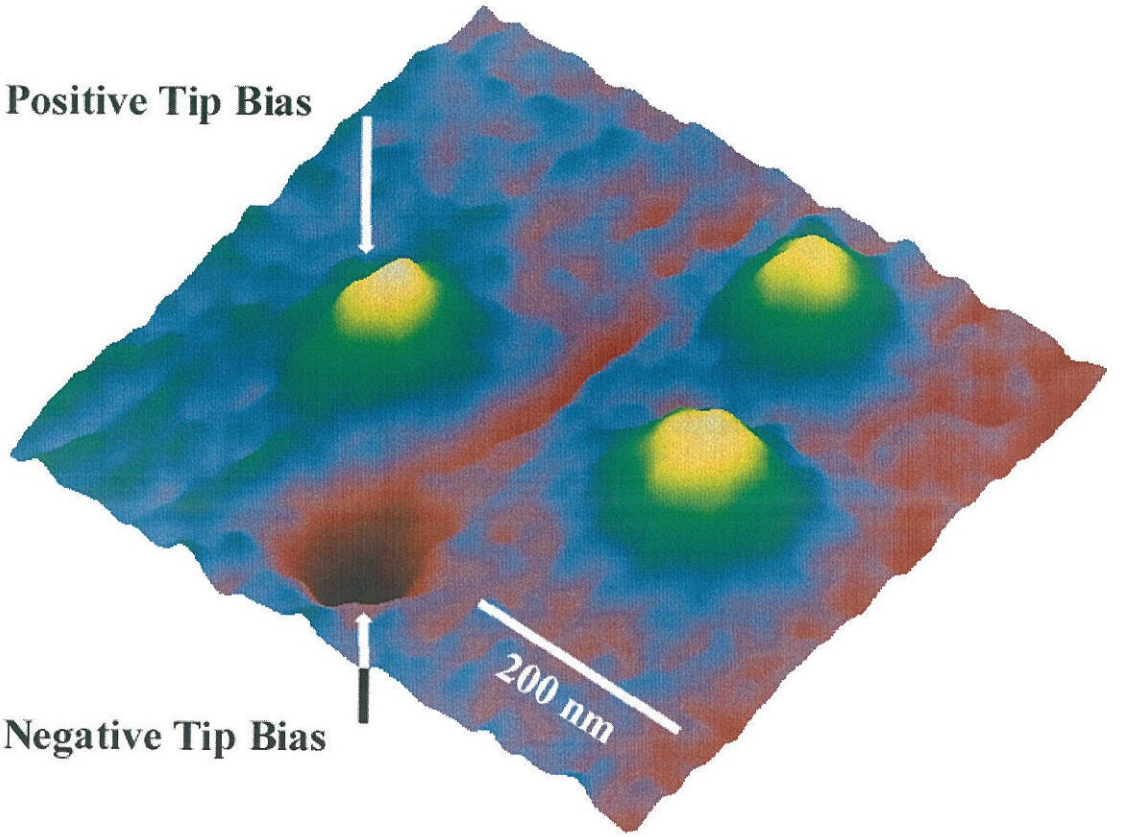

Figure 7.2: A square array of 150 nm FWHM dots of charge, 3 positive and 1 negative, written with an EFM to a $CeO_2/Si/CeO_2/Si$ structure. No topographical changes in the oxide were detected by AFM after writing, but the dots are clearly visible in the EFM image. Dots of both positive and negative charge can also be rewritten over one another by application of the opposite writing voltage.

the structure was performed by reducing the tip - sample separation and applying a relatively large tip voltage (10 V) for approximately 30s. By applying either positive or negative bias, regions of either positive or negative charge could be written. Figure 7.2 shows an example of writing a square array of charged regions; 3 positive and 1 negative. Figure 7.3 shows an example of rewriting one of the positive regions with a negative one. Some residual positive charge remains since the tip piezos did not return exactly to the write coordinates. In detail, the writing process for depositing charge in the structure was as follows.

1 Move to the desired position.

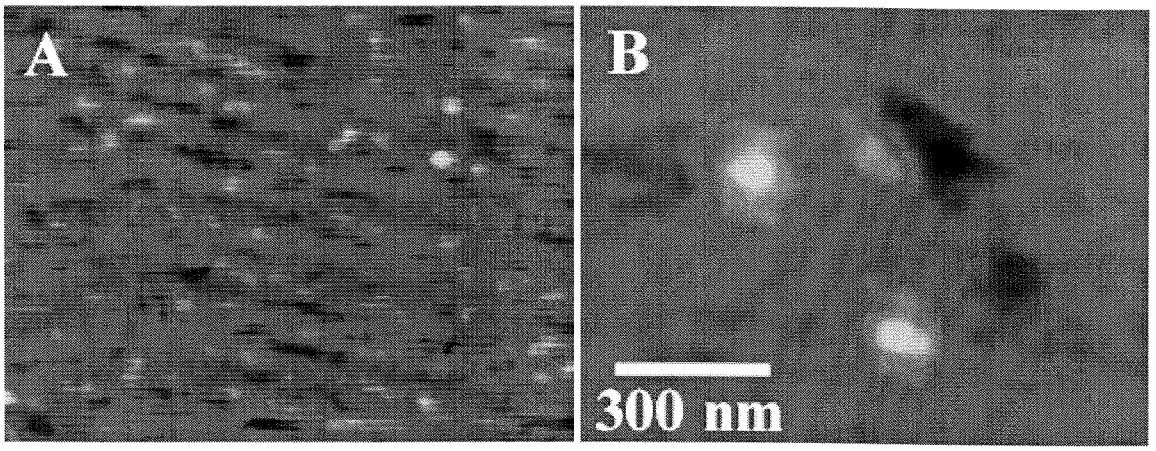

Figure 7.3: A. Atomic force microscopy of the CeO_2 layer indicating that it is unchanged during the deposition of charge of either sign. B. Electric force microscopy of charge dots of both signs. The dot in the upper right was originally positive and was rewritten to be negative. Some residual positive charge remains since the tip piezos did not return exactly to the write coordinates. One interesting feature of the image is the close proximity of the two types of charge which remained distinct without leakage.

2 Reduce the scan size to 1 nm or to 0 nm.

3 Set the tip-sample distance to 30 nm.

4 Set the "write" voltage by applying the appropriate tip voltage (Typically 10 V).

5 Reduce the tip-sample distance to approximately 5nm.

6 Wait.

7 Set the tip voltage to 0V and the lift height to 30nm.

8 Repeat.

After the patterns were written, electrostatic force imaging data was taken in the manner described in Chapter 6, Section 6.2. The tip voltage was held around 1V during imaging since in practice large tip voltages tend to introduce topographic artifacts at tip biases around 3V. When the phase differences are very small, the relationship between the phase shift and the frequency shift can be approximated by a linear relationship. Which, when calibrated for the cantilevers in this experiment,

was found to be $\delta f \approx 3.5\Delta\theta$ Hz/deg . No changes in the topography were measureable with the AFM after the charge regions were written.

To compute the total stored charge, Q, we first use an electrostatic analysis given in Reference [8] to compute the localized charge stored in an insulator, q. The frequency shift, δf, is related to the gradient of the force by the expression $\Delta f = -f_0 f'(z_0)/(2k)$, where $z_0 = 30$ nm is the tip to sample separation during imaging, $f_0 = 59.8$ kHz is the resonant frequency of the tip, and $k = 3$ N/m is the estimated spring constant of the tip. The electrostatic force the tip feels under an applied DC bias due to charge-charge interactions for charge buried in a dielectric layer is given by

$$F(z) = \frac{1}{(z + (2d_{CeO_2}/\epsilon_{CeO_2}) + (d_{Si}/\epsilon_{Si}))^2} \times \left(- \frac{d_{CeO_2}^2 q^2}{\epsilon_{CeO_2}^2 \epsilon_0 a} + \frac{2 d_{CeO_2} q V_{EFM}}{\epsilon_{CeO_2}} + \frac{\epsilon_0 a V_{EFM}^2}{2} \right) \tag{7.3}$$

where z is the tip to sample separation, d and ϵ are the thickness and dielectric constant of the CeO_2 and Si films, as indexed, V_{EFM} is the bias applied to the tip, and a is the area of the charged region. The first term in the bracket in Eq. 7.3 is found to be negligibly small, and the last term provides a constant background independent of the charge. Using only the middle term and the values given above, an approximation to the localized stored charge is then given by $q = 43\Delta\theta$ e/deg. If this expression is used directly as in the case of Reference [8], we obtain q = 2 to 10 e. Since this was such a low value for the amount of stored charge, we modified the above model based on the following observation. Simple force modeling predicts the EFM image of a single localized charge to be 56 nm FWHM, with an area $a = 2450$ nm^2. This is less than the 150 nm FWHM that is typically observed. Therefore, we estimate the total stored charge in our EFM images by scaling the expression for q above by the ratio A/a where A is the experimentally observed area of the charge. Hence, we estimate the total charge contained in the region as $Q = q(A/a)$ e. For the dots in Figure 7.2, $\Delta\theta = 0.23°$ over an area of $A = 1 \times 10^5$ nm^2, we compute $Q = \pm 42$ e.

It is not unreasonable to speculate that the amount of charge could in fact be a single electron which is the case for the smallest dots with a FWHM of 50 nm. For a

single charge, the self potential, V = 3kT for room temperature, at reasonable read distances so thermal noise would not swamp the cantilever. The image charge force of a single electron on a grounded tip is F= 0.06 pN which is within the AFM's detection limit. Therefore, it would be an interesting experiment to look for quantization effects after depositing a small amount of charge.

To examine the effects of writing parameters on the resultant charge dot size and intensity, an array of positive charge dots was written at various EFM tip biases, tip to sample distances, and write times as shown in Figure 7.4. Line scans were taken across the low-pass filtered image to extract charge dot sizes and relative intensities. It is found in general that both the size and the intensity of the charge dots scale linearly with the same slope in relation to the various writing parameters. From a nominal starting point of 10 V, 60 s, and 5 nm, it is found that the size and intensity of the charge dot may be expected to decrease 10% for each 0.5 V decrease in charging voltage or 10 s decrease in charging time, and increase 10% for a 2 nm decrease in tip to sample separation.

To examine the time evolution of stored charge in our system, single charge dots were written and monitored over time. In all cases, the general trend was for a slow leakage of charge accompanied by an increase in FWHM of the charge dot, as shown in Figure 7.5 (A,B). To estimate the lifetime associated with the stored charge, a single charge dot was written and continuously monitored over several days. After writing at $V_{EFM} = 10$ V, $z = 3$ nm, and $t = 60$ s, the resulting charge dot was continuously imaged at $V_{EFM} = 1$ V and $z = 30$ nm at a read speed of 21 reads/hr for the first 4 hrs, after which imaging was performed intermittently for the remainder of the experiment. A plot of the total stored charge, Q, is shown in Figure 7.6. There is an initial period of charge settling and reorganization during which it is difficult to reliably extract charge dot profiles in order to determine the stored charge. After this settling period and over the first 10 hrs, an exponential fit to the charge decay exhibits a time constant $\tau \sim 9.5$ hrs, after which the rate of decay slows down considerably to $\tau > 24$ hrs. After a period of $t > 40$ hrs, the stored charge either leaked away or was no longer detectable by our instrument. This is a substantially longer time constant

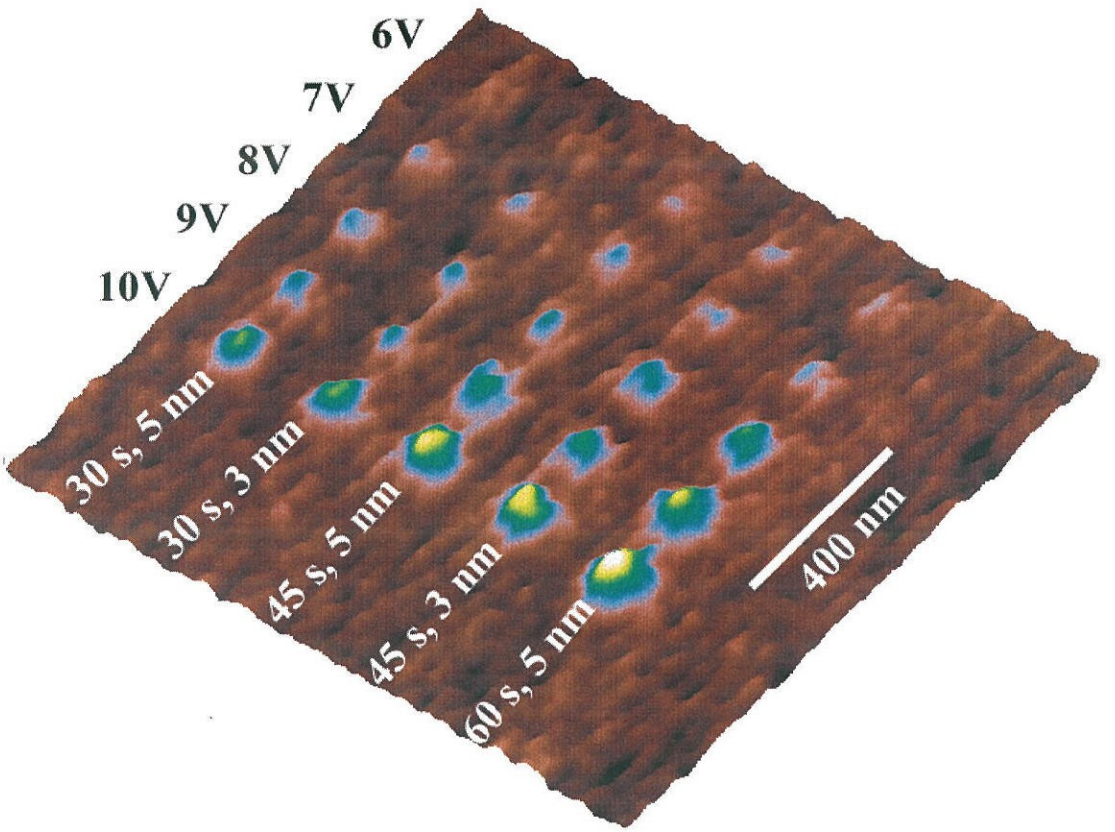

Figure 7.4: Electric force microscopy of an array of dots written at different voltages, tip to sample separations, and writing times as labeled. Dot intensity and size are strongly dependent on voltage and writing time, and more weakly dependent on tip to sample seperation.

than the 300 s obtained by Yu et al. for charge storage in cobalt nanostructures.

7.2 Conclusions

In conclusion, a novel application of EFM was used to write and image localized dots of charge in a double barrier CeO_2/Si/CeO_2/Si(111) structure. By applying relatively large tip voltages of $V_{EFM} = \pm(6 - 10)$ V and reducing the tip to sample separation to $z = 3 - 5$ nm, charge dots 50-200 nm FWHM of both positive and negative charge have been written. The total stored charge is found to be $Q = \pm(1 - 90)$ e per charge dot. These charge dots are shown to be stable over periods of time greater than a day, with an initial charge decay time constant of $\tau \sim 9.5$ hrs followed by a period of much slower decay with $\tau > 24$ hrs. The dependence of charge dot size and total stored charge on various writing parameters such as tip bias, tip to sample separation, and write time has been examined and linear dependencies extracted.

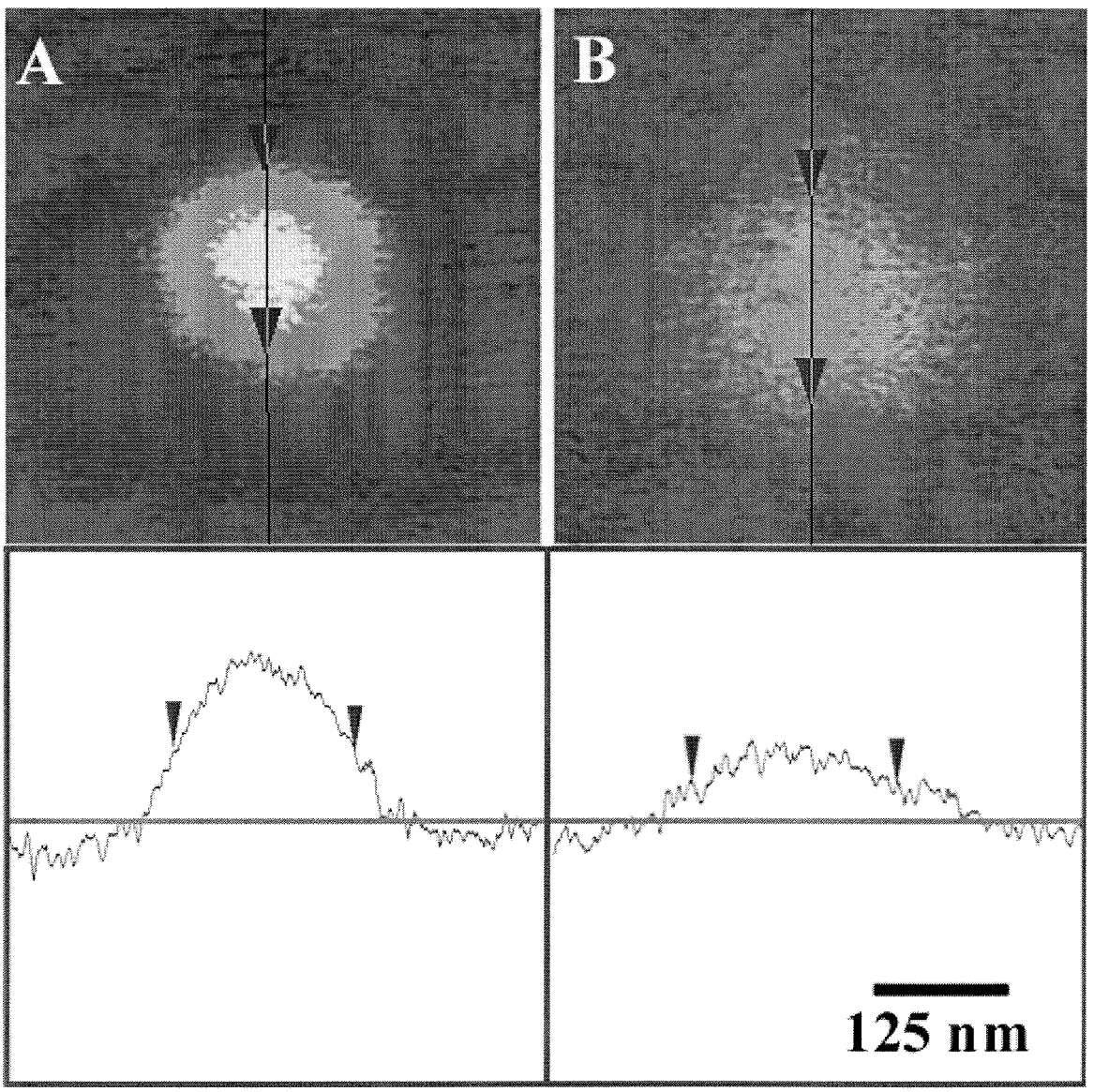

Figure 7.5: Electric force microscopy of deposited charge shortly after deposition (A) and again (B) after 20 hours. Line scan profiles of the charged regions indicate both spreading and leakage.

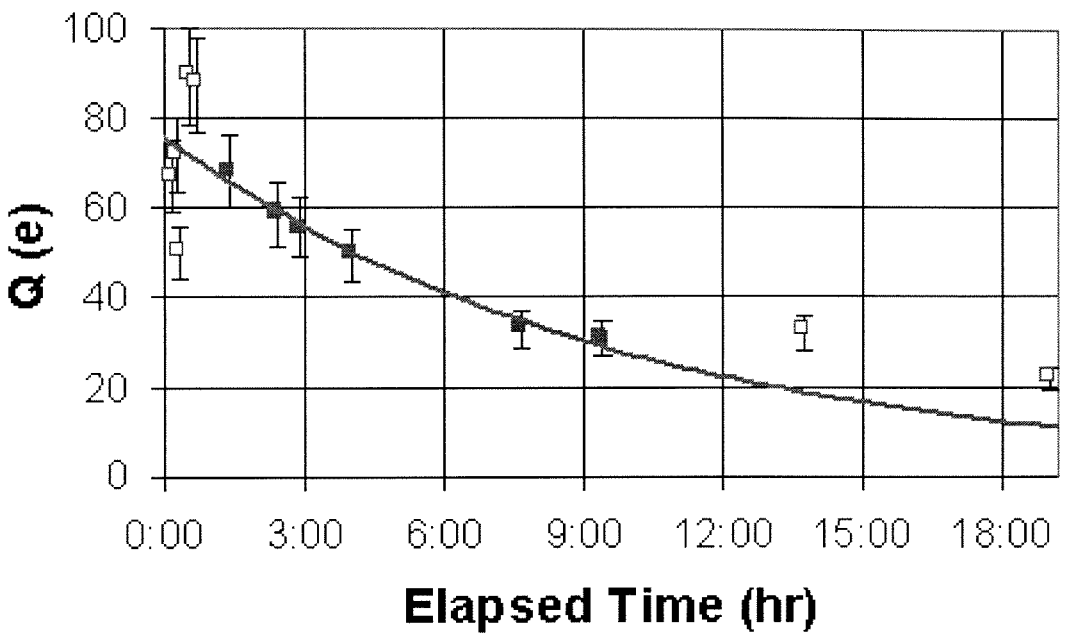

Figure 7.6: Decay curve for the deposited charge. After a settling period and over the first 10 hrs, an exponential fit to the charge decay exhibits a time constant $\tau \sim 9.5$ hrs, after which the rate of decay slows down considerably to $\tau > 24$ hrs. After a period of $t > 40$ hrs, the stored charge was no longer detectable by our instrument.

Bibliography

[1] T. Inoue, Y. Yamamoto, S. Koyama, S. Suzuki, and Y. Ueda, Appl. Phys. Lett. **56**, 1332 (1990).

[2] L. Luo, X. Wu, R. Dye, R. Muenchausen, S. Foltyn, Y. Coulter, C. Maggiore, and T. Inoue, Appl. Phys. Lett. **59**, 2043 (1991).

[3] T. Inoue, Y. Yamamoto, M. Satoh, A. Ide, and S. Katsumata, Thin Solid Films **281-282**, 24 (1996).

[4] T. Chikyow, S. Bedair, L. Tye, and N. El-Masry, Appl. Phys. Lett. **65**, 1030 (1994).

[5] S. Yaegashi, T. Kurihara, H. Hoshi, H. Segawa, Jpn. J. Appl. Phys. **33**, 270 (1994).

[6] J. Jones, E. Croke, C. Garland, O. Marsh, and T. C. McGill, J. Vac. Sci. Technol. B **16**, 2686 (1998).

[7] J. C. Mallinson, *The Foundations of Magnetic Recording* Academic Press, San Diego, CA, 1993.

[8] D. M. Schaadt, E. T. Yu, S. Sankar, and A. E. Berkowitz, Appl. Phys. Lett. **74**, 472 (1999).

[9] Y. Martin, D. W. Abraham, and H. K. Wickramasinghe, *Appl. Phys. Lett.* **52**, 1103 (1988).

[10] Dror Sarid, *Scanning Force Microscopy*, Oxford University Press, New York, 1991.

[11] F. Saurenbach and B. D. Terris *Appl. Phys. Lett.* **56**, 1703 (1990).

[12] J. E. Stern, B. D. Terris, H. J. Mamin, and D. Rugar, Appl. Phys. Lett. **53**, 2717 (1988).

[13] H. Yokoyama and T. Inoue, *Thin Solid Films*, 242, 33, (1994).

[14] R. M. Nyffenegger, R. M. Penner, and R. Schierle, Appl. Phys. Lett. **71**, 1878 (1997).

[15] M. Nonnenmacher, M. P. O'Boyle, and H. K. Wickramasinghe, App. Phys. Lett. **58**, 2921 (1991).

[16] K. K. Thornber, T. C. McGill, and C. A. Mead, J. Appl. Phys. **38**, 2384 (1967).

Appendices

Appendix A Surface Potential Microscopy

A.1 Derivation of the Force on the Tip from the Maxwell Stress Tensor

Originally, surface potential microscopy was called scanning Maxwell stress microscopy since the force on the tip is obtained by integrating the Maxwell stress tensor T_{ij} over the tip surface

$$F_i = \oint_{tip} T_{ij} dS_j. \tag{A.1}$$

Where the stress tensor in the absence of a magnetic field is: 5

$$T_{ij} = E_i D_j - \frac{1}{2}\delta_{ij}\mathbf{E}\cdot\mathbf{D}. \tag{A.2}$$

Since the electric field is always perpendicular to a perfect conductor, the normal component of the stress tensor at a point on the surface of the tip, r_t, reduces to

$$T_{kk} = \frac{1}{2}\epsilon(\mathbf{r_t})\mathbf{E}(\mathbf{r_t})\cdot\mathbf{E}(\mathbf{r_t}) = \frac{1}{2\epsilon}\rho_t^2(\mathbf{r_t}) \tag{A.3}$$

where $\rho_t(\mathbf{r_t})$ is the surface charge density on the tip. If there are isolated charge densities,$\rho(\mathbf{r})$, polarization fields, $\mathbf{P}(\mathbf{r})$, and sample regions at potentials V_l, then

$$\rho_t(\mathbf{r_t}) = \int [\rho(\mathbf{r}')]\, g(\mathbf{r_t}, \mathbf{r}')d\mathbf{r}' + \sum_{l=1}^{N} c_i(\mathbf{r_s})V_i + c_t(\mathbf{r_s})V_t \tag{A.4}$$

where $g(\mathbf{r_t}, \mathbf{r}')$ is the image charge density induced on the tip surface at $\mathbf{r_t}$ by a unit point charge at $\mathbf{r}'$. The terms $c_i(\mathbf{r_s})$ and $c_t(\mathbf{r_s})$ are the differential capacitance between the l^{th} potential and the self capacitance of the tip.

If an oscillating voltage plus a DC bias is applied directly to the AFM tip, $V_{applied} = V_{dc} + V_0 \cos(\omega t)$, the tip will feel a force with a DC component plus components at ω and 2ω due to the quadratic nature of the stress tensor.

$$T_\omega = \frac{1}{\epsilon}\left(\int \left[\rho(\mathbf{r}') - \nabla\mathbf{P}(\mathbf{r}')\right] g(\mathbf{r_t}, \mathbf{r}')d\mathbf{r}' + \sum_{l=1}^{N} c_i(\mathbf{r_s})V_i + c_t(\mathbf{r_s})V_{dc}\right) c_t(\mathbf{r_s})V_0 \cos(\omega t) \tag{A.5}$$

$$T_{2\omega} = \frac{1}{2\epsilon}V_0^2 c_t^2(\mathbf{r_s}) \sin^2(\omega t) \tag{A.6}$$

Since Eq. A.6 represents purely capacative forces, only the ω component will be considered here. Therefore, the force felt by the tip at frequency ω will become

$$F_\omega = \oint_{tip} T_\omega cos\theta dS_{tip} \tag{A.7}$$

Finally, the voltage V_{dc} is regulated by an external feedback loop so that the force F_ω vanishes at

$$V_{dc} = \frac{\int \left[\rho(\mathbf{r}') - \nabla\mathbf{P}(\mathbf{r}')\right] \oint_{tip} g(\mathbf{r_t}, \mathbf{r}') \cos\theta dS_{tip} d\mathbf{r}' + \sum_{l=1}^{N} V_i \oint_{tip} c_i(\mathbf{r_s}) c_t(\mathbf{r_s}) \cos\theta dS_{tip}}{\sum_{l=1}^{N} \oint_{tip} c_i(\mathbf{r_s}) c_t(\mathbf{r_s}) \cos\theta dS_{tip}} \tag{A.8}$$

If there are no charge densities and polarizations present, and only one other potential besides the tip, the measurement gives the potential directly. In most of the studies here, however, there are induced charges at the surface due to spontaneous polarization and piezoelectricity so the force will be an average of all these effects.

Appendix B Microellipsometer

B.1 Motivation

Ellipsometry is the standard way to quantitatively determine the optical properties and thicknesses of thin films. Despite being very accurate, the best ellipsometers are currently limited to approximately 50 μm spatial resolution. In an attempt to increase the spatial resolution, we explored a novel scanning probe technique we called the microellipsometer. The concept was to replace the free space optical path in a standard ellipsometer with polarization preserving fibers that could be brought close together and used as a polarizer/analyzer combination. The whole assembly could then be scanned over the sample. The spatial resolution would then be determined by the proximity of the two fibers which could approach 1 μm.

B.2 Types of Ellipsometers

There are three primary ellipsometer designs:

Null ellipsometer The null ellipsometer has the following elements:

Source $\longrightarrow$ Polarizer $\longrightarrow$ Compensator $\longrightarrow$ Sample $\longrightarrow$ Analyzer $\longrightarrow$ Detector

The objective of a measurement is to adjust the polarizer, compensator and analyzer to achieve a signal minimum at the detector. Complicated.

Polarization modulation

Source $\longrightarrow$ Polarizer $\longrightarrow$ Modulator $\longrightarrow$ Sample $\longrightarrow$ Analyzer $\longrightarrow$ Detector

Modulations of the input polarization are usually many kHz allowing for fast measurements but calibration is difficult.

Rotating element It is possible to construct an ellipsometer using only two polarizers for the polarizer and analyzer components. This method has the advantage of being simple to construct and align as well as being achromatic.

$$\text{Source} \longrightarrow \text{Polarizer} \longrightarrow \text{Sample} \longrightarrow \text{Analyzer} \longrightarrow \text{Detector}$$

It is this configuration that is used to implement the fiber microellipsometer. In the actual experiment, however, the analyzer element was rotated manually rather than continuously spinning.

B.3 Construction of instrument

B.3.1 fiber etching

Elliptical core, single-mode, polarization preserving fiber (Corning PMF-38) was etched to remove the cladding in order to bring the cleaved ends in close proximity. The fiber orientation was marked and the fiber was stripped and cleaved. The cleaved ends were then immersed in a solution of 25 mL 49% hydrofluoric acid and 25 mL 10% buffered HF solution (BOE etchant) and etched for 30 minutes. Since the radial etch rate is slow at the beginning of the etch and more rapid at the end, it was essential to carefully monitor the fiber ends.

Detection head assembly

The etched fibers were then mounted to a home built micromanipulator in order to position them in the holder. The holder was fabricated in lab and consisted of a # 8, stainless steel, machine washer with a hole drilled end-wise using a # 70 wire drill bit. The fibers were then threaded through the holes on either end and aligned. For the alignment, the separation of the cleaved ends and their angle was fixed by observation

through microscopes positioned at right angles (plan and profile) to the head assembly. The entire configuration was then epoxied into place to fix the alignment. A magnet holds the steel washer to an actuator which controlls its distance to the sample. The final assembly and a closeup of the fiber ends is shown in Figure B.1.

B.3.2 Control Experiment and Preliminary Results

In order to test the ellipsometer head, a calibration experiment was performed as shown in Figure B.2. Light from a near IR laser source is chopped for lock in detection and then polarized with a sheet polarizer. The source was a Melles Griot laser diode model 56DLB108 of wavelength $\lambda = 830$nm which was biased at 85.1 mA with a Keithley 238 high current source measure unit to give an optical power output of 25.5 mW. It then passes through a polarization rotator to set the polarization along one of the eigen-axes of the fiber. After passing though the fiber, it is incident on coverslip coated with gold in an evaporater intended as a reference sample. The reflected light is then collected by the second fiber and is incident on the analyzer and finally on a photodiode in a transimpedence amplifer configuration. Lock-in detection was performed with an EG&G 5101 single channel lock in amplifier at the chopping frequency. The distance to the sample was monitored under a microscope and controlled by a Newport 855C programmable controller with a Newport actuator 850. Results of the experiment are shown in Figure B.3 and indicate that there was some polarization sensitivity. Unfortunately locating the fast and slow axes to launch the polarized mode was not possible by hand. Moreover, the alignment of the two fibers in the probe assembly was unknown. Therefore, the results are most likely a mapping of the fiber misalignment rather than measuring the sample. Future instruments would need a way to better determine the alignment of the fiber axes as well as rotating polarizers to make fast measurements.

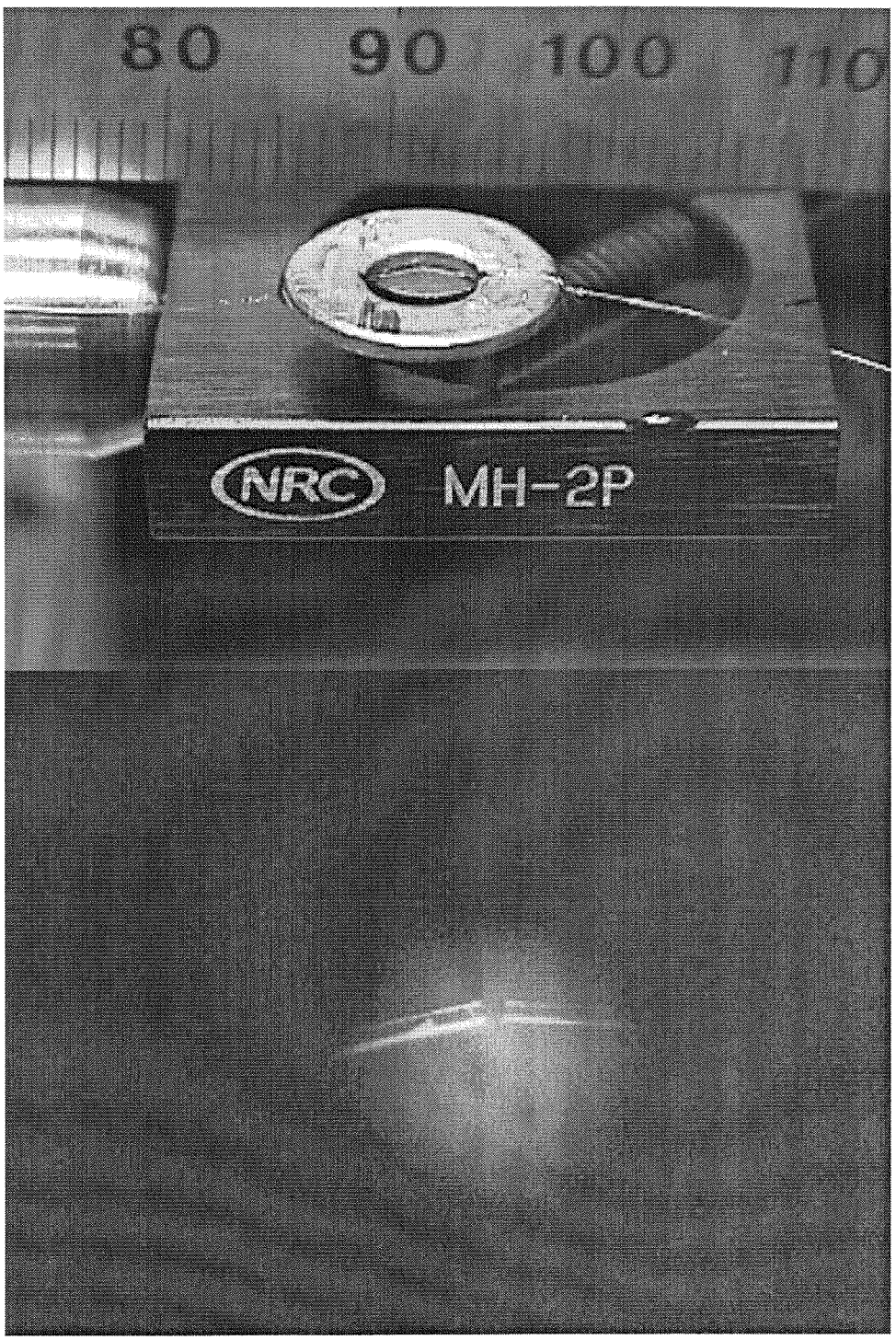

Figure B.1: Close up of the fiber probe.

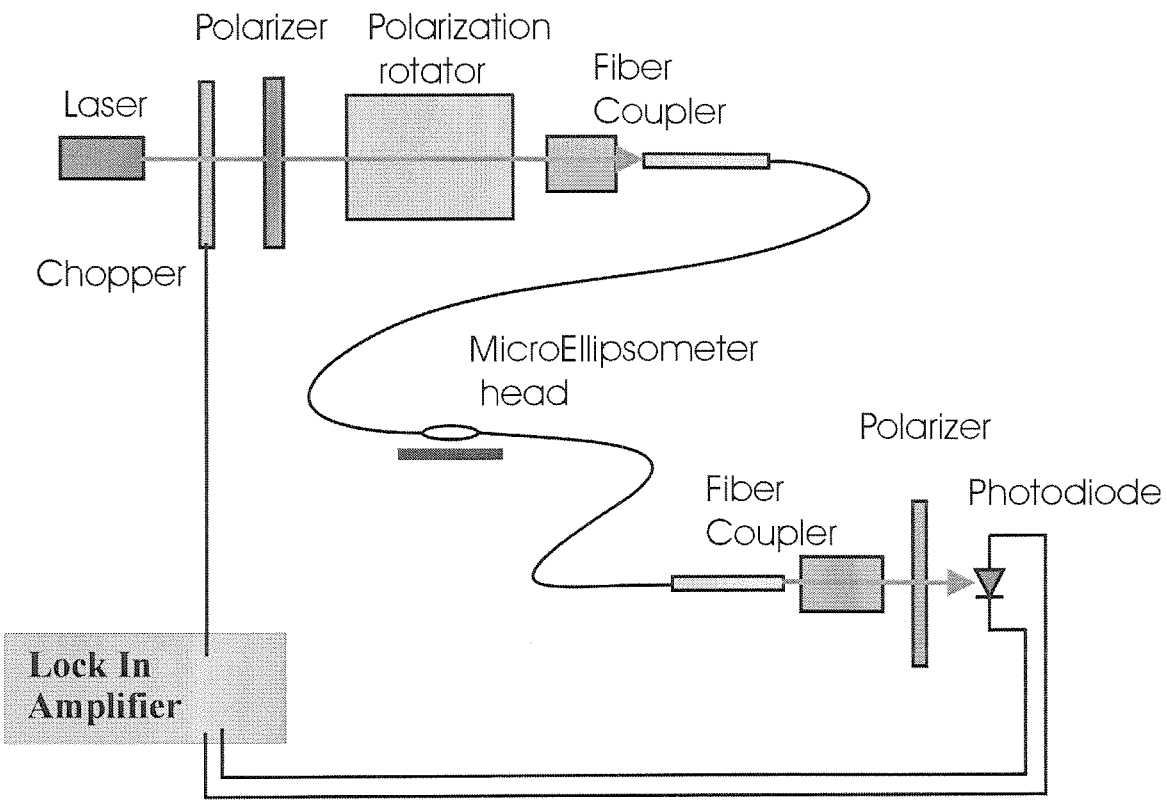

Figure B.2: Schematic of the microellipsometer experiment.

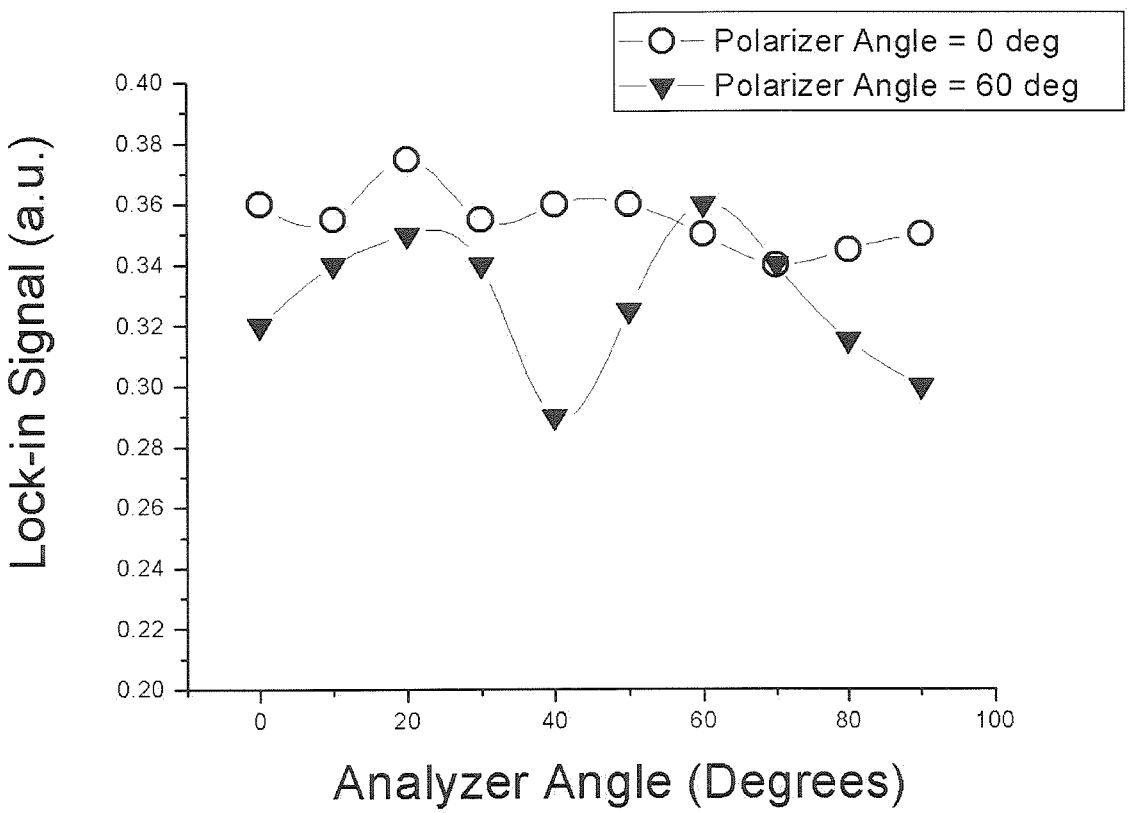

Figure B.3: Preliminary results from the microellipsometer. The lock-in amplifier signal from the analyzer photodiode is plotted as a function of the analyzer angle for two input polarizations. The angle of the fiber from the normal to the sample is roughly 70 degrees.